UNIVERSITY OF TRENTO - Italy

Department of Physics

Doctoral dissertation
in partial fulfillment of the requirements for the degree
of *Doctor of Philosophy* in the subject of Physics

On-chip photonic label-free biosensors

Supervisor:
Prof. Lorenzo Pavesi

Ph.D. candidate:
Davide Gandolfi

XXVII PhD cycle in Physics
March 2015

Prefazione

Quando, ormai più di tre anni e mezzo fa, concludevo il mio Percorso di Laurea in Fisica, avevo molta voglia di mettermi alla prova. Il mio ideale era una ricerca applicata, che fosse intellettualmente stimolante ma anche di rilevanza tecnologica a breve termine. La scelta di continuare con un dottorato è stata condizionata, tra le altre cose, anche da un confronto con il prof. Pavesi, quando ancora non sapevo che sarebbe diventato il mio relatore.

Con il percorso che ho intrapreso, penso di aver raggiunto il mio obiettivo: ho infatti trovato molto edificante esplorare il mondo della "Silicon Photonics", che fino a prima del dottorato mi era quasi totalmente sconosciuto. Soprattutto il primo anno, quando ancora stavo prendendo dimestichezza con la materia, ero continuamente stimolato dalle nuove tecniche apprese, e continuavo a sforzarmi di immaginare come prendere il meglio di ognuna per applicarle alla mia ricerca. Data la vasta dimensione della comunità scientifica coinvolta in questo settore, nella maggior parte dei casi ho trovato che le mie idee erano già state esplorate più o meno approfonditamente da altri lavori. Tuttavia, questo ha costituito, per me, non un motivo di sconforto quanto, al contrario, di ulteriore soddisfazione, perché potevo confrontarmi e vedere che anche altre persone si erano poste le mie stesse domande.

Ho trovato parecchia soddisfazione anche dall'interdisciplinarità del mio progetto di ricerca, che mi ha permesso di espandere la mia conoscenza, oltre che nel campo della fisica, anche in quello della chimica e della biologia (anche se molto "di settore"). Lo sforzo ulteriore, reso necessario dalle mie limitate conoscenze pregresse, è stato ricompensato dal buon risultato finale della ricerca.

Infine, un altro aspetto non strettamente scientifico della mia formazione durante il percorso di dottorato è stato lo sviluppo del mio profilo professionale. Anche grazie ai corsi dell'UNITN, *Crash Course on Research Funding, Intellectual Property and Start up Creation* e *IEEE Italy School of Career Boosting*, ho maturato la convinzione che si possa fondere buona ricerca tecnologica, innovazione e conoscenza anche fuori dall'università, con un trasferimento di sapere a doppio senso con le aziende e le start-up. Per questo motivo, insieme ai miei due amici e colleghi Matteo Franchi e Luca Matteo Martini, ho ideato, organizzato e curato la prima edizione di *IPSP Industrial Problem Solving with Physics*. La prima soddisfazione è stata vedere

il pieno supporto e la fiducia che l'Università ed il Dipartimento di Fisica hanno riposto nel nostro progetto. La seconda, e forse più grande, è stata vederlo realizzato, concreto e secondo i piani. Essendo stato il primo progetto curato da noi tre, il successo e il forte impatto mediatico riscosso mi ha veramente colpito e mi ha dato molta carica. Spero che anche le future edizioni possano continuare a ricevere altrettante soddisfazioni e a beneficiare di fruttuose collaborazioni.

Vorrei ringraziare in primo luogo il prof. Lorenzo Pavesi, sia per la sua guida scientifica che per i suoi consigli, sul piano umano e professionale. Ringrazio anche Laura, per l'aiuto costante nell'organizzare e preparare gli esperimenti di biosensing di questi anni, e Romain, che oltre ad essersi dimostrato un piacevole collega ed amico, è stato indispensabile per la pesantissima e lunghissima burocrazia di Symphony. Un grazie lo dedico anche ai miei colleghi Fernando e Paolo, che mi hanno aiutato in vario modo in questi anni, soprattutto con piacevoli ed a volte illuminanti dialoghi e confronti. Un pensiero lo dedico anche agli amici fisici (e chimici) che mi hanno accompagnato in questi anni, rendendo l'ambiente di lavoro anche un ambiente familiare e di cordialità.

Ringrazio i miei genitori, che mi hanno permesso di studiare e che mi hanno sempre sostenuto nelle mie scelte di percorso. Infine, un grazie immenso a Sofia, a colei che, purtroppo, si è subita anche i lati negativi del mio dottorato: i weekend saltati per delle urgenze da concludere a scadenza, i malumori per degli insuccessi inspiegati, quando finivo tardi (e senza avvisare!) in laboratorio, le notti insonni per scrivere una tesi che non ne voleva sapere di saltare fuori da quelle maledette pagine bianche. Lei che mi è stata vicina sempre, dimostrandosi paziente, premurosa e di conforto. A lei, ed al suo grande amore, io devo il mio dottorato, e per questo motivo le dedico i risultati dei miei sforzi.

Davide Gandolfi
Trento
Marzo 2015

Abstract

The development of a highly integrated optical biosensor is expected to significantly impact on the performances and on the throughput of biochemical assays, with applications in the field of pharmaceutical research, point-of-care diagnostic, food-borne pathogens screening and safety.

This dissertation studies the development of a label-free on-chip biosensor for the selective detection of Aflatoxin-M1 from milk content. We detail the design and the realization of two types of multiplexed sensors. They are based on the silicon photonics technology and operates in liquid ambient at wavelengths in the near-visible and near-infrared spectra.

Most of this work is focused on the first type of sensor, which is based on a whispering-gallery-mode resonator. In particular, we analyze microdisk, microring and wedge resonator structures, studying the sensitivity and the quality factor of each. The appeal of these structure is given by the low detection limit that can be achieved in a footprint of few tens of microns per side.

The second sensor type is based on a spectrally resolved asymmetric Mach-Zehnder interferometer. In this case, the high level of folding permitted by the use of high refractive-index-contrast materials enables the fabrication of sensitive interferometers in a reasonable footprint.

The experimental characterization of the bulk refractometric sensing of the devices is performed in continuous flow, using a dedicated microfluidic flow-cell in PDMS. This characterization assesses the high resolution of both device types, which are able to resolve variations in the refractive index of the liquids with a limit of detection down to 10^{-6} refractive index units (RIU).

The selective superficial sensing is also evaluated, implementing a biorecognition functional layer with DNA-aptamers. The assay of buffered solutions containing Aflatoxin-M1 molecules confirms that the devices under test are suitable biosensors, with specific detection limits down to about 100 pg ml^{-1} for the Mach-Zehnder interferometer, and slightly larger for the microring resonator.

A procedure for the regeneration of the sensor has been optimized, enabling reproducible sensing up to nine times. The detection of the receptor-ligand binding in real-time enabled

the study of the kinetics of the binding reaction, and we measured for the first time the kinetic rate constants of the anti-aflatoxin aptamers of our sensors.

Contents

List of Acronyms

AFM1 Aflatoxyn M_1 69

aMZI Asymmetric Mach-Zehnder Interferometer xx

ASE Amplified Spontaneous Emission 39

BHF Buffered HF oxide etch 21

BPSG Borophosphosilicate Glass 21

CMOS Complementary Metal Oxide Semiconductor xiii

CMT Coupled Mode Theory 72

DMSO Dimethyl Sulfoxide 120

DRIE Deep Reactive-Ion Etching 83

ELISA Enzyme-Linked Immunosorbent Assay xiv

ER Extinction Ratio 14

FEM Finite Element Method 13

FOM Figure Of Merit 8

FSR Free Spectral Range 14

LOD Limit Of Detection 8

LPCVD Low-Pressure Chemical Vapor Deposition 68

MES 2-(N-morpholino)ethanesulfonic acid 119

MFD Mode Field Diameter 53

MRR Micro Ring Resonator xx

MZI Mach-Zehnder Interferometer 7

NIR Near Infrared

OSA Optical Spectrum Analyzer 39

PBS Phosphate Buffered Solution 118

PCB Printed Circuit Board 50

PDMS Polydimethylsiloxane

PECVD Plasma-Enhanced Chemical Vapor Deposition 68

PML Perfectly Matched Layer 18

RIE Reactive-Ion Etching 21

SEM Scanning Electron Microscope 21

SNR Signal to Noise Ratio 8

SPR Surface Plasmon Resonance xv

TE Transverse Electric 17

TEOS Tetraethyl orthosilicate 93

TM Transverse Magnetic 17

Tris Tris(hydroxymethyl)aminomethane 119

VCSEL Vertical-Cavity Surface-Emitting Laser 45

VIS Visible

WGM Whispering Gallery Mode xvi

Introduction

Lifesciences are growing at fast-pace, attracting attentions from many different research and market fields. Biophysics, bioinformatics and biotechnologies are fusing together interdisciplinary expertises, and this cross-fertilisation of ideas is probably the most appealing feature for the curious mind of a physicist.

The advances in the understanding of the biological functions of living species are usually driven by the introduction of new technologies, to detect or amplify the signals and features of the small bio-objects. One of the most striking and relatively recent examples is the *polymerase chain reaction* (PCR) [1], that opened the road for the amplification of DNA pieces and that, eventually, gave a fundamental contribution to the sequencing of the human genome. Thus,

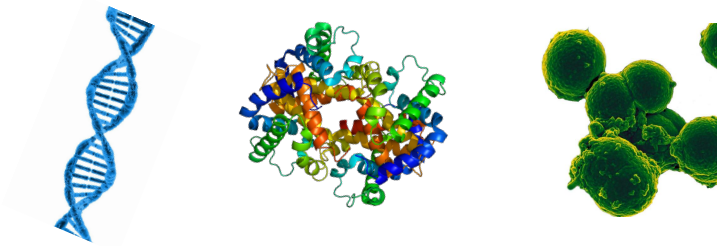

(a) (b) (c)

FIGURE 1: Representation of some examples of biological targets that a biosensor could detect. (a) DNA strands, (b) proteins or other signalling molecules, and (c) viruses and bacteria[1].

[1] Photographs: *PublicDomainPictures* at `http://pixabay.com/`, *Emw* at `http://de.wikipedia.org/`, and *NIAID/NIH* at `www.flickr.com/photos/niaid/`.

(a)

(b)

FIGURE 2: Two common features that are highly demanded in biological and chemical analysis systems: (a) high throughput, achieved by running in parallel several analysis, and (b) small sample volume consumption, to reduce the time and the costs. Both are inherent features of integrated lab-on-chips[2].

there is a continuous demand for the development of sensors and technologies that are able to detect or visualize biological materials, from whole cells to single molecules, with increasing capabilities.

Small integrated and functional chips are particularly appealing for creating biosensors: with the realization of miniaturized sensing sites, it is possible to limit the volumes of the samples or of the chemicals involved in the detection protocol, reducing the costs and the time of every assay. The device itself can be cheaper, because a high number of multiplexed sensors can be fit and run in parallel in a small area, as small as few square millimeters. Low cost and disposable biosensor cartridges allow for a simpler apparatus and a more accurate detection, without interference between consecutive assays. In addition, it is possible to combine a microfluidic sub-systems that transport, mix, process, separate and drain the fluids (sample and reagents). These integrated chips, with functional and sensing capabilities are known with the name of *Lab-on-Chip* [2, 3]. The aim of a Lab-on-Chip is to reduce the complexity of the sensing protocol, so that even untrained operators can correctly perform the measurements. In this way the analysis (and diagnosis) can be conveniently moved from the medical laboratories to the patients, through simple-to-use point-of-care testing devices.

Integrated optics and electronics are particularly suited to satisfy

[2]Photographs: *PublicDomainPictures* at `http://pixabay.com/` and *Jennifer Kanaan* at `http://fitnstyle.com/`.

the demand of miniaturized and multiplexed sensors. With the use of photolithography it is possible to realize sensors with sizes as small as few microns, densely interconnected and with special functionalities [4, 5]. *Complementary Metal Oxide Semiconductor* (CMOS) is the standard fabrication technology for silicon-based microelectronics. Similarly, CMOS-compatible silicon photonics is leading the field of integrated optics, taking advantage of the high degree of maturity of the technology, as well as of several favourable optical properties of silicon, first of which the high refractive index, that enables the realization of small optical wires with sharp bends [6]. However, photolithography is not the only available method to realize integrated optics. With the use of polymers, for example, it is possible to create a soft master mold and replicate polymeric optics with a high quality of the finishing and of the transmission properties [7, 8].

There are many applications in which a highly integrated Lab-on-Chip, or biosensor in general, could be of particular interest. The first and more obvious is for medical diagnostics, in specialized laboratories but also in point-of-care instrumentations. In this case the multiplexing capabilities of an integrated biosensor could improve the accurate recognition of a particular disease, by screening the sample against several markers [9]. Another interesting application is the detection of contaminants in the food industries. In this case the analyte, i.e. the target biomolecule, can be pesticides, toxins or mutated DNA sequences (thus, recognizing OGMs from biological products). Pharmaceutical research can benefit from the multiplexing capabilities, from the reduced samples volumes, but also for the real-time response offered by some systems. In drug screening and development, in fact, it is very important to be able to follow the kinetic of the uptake of the drugs. For what concerns environmental and pollution monitoring, biosensors can be used to detect bacteria, chemical compounds and heavy metals [10], that are present in the atmosphere, in the soil or in the waters. Lastly, an important application of biosensors, especially nowadays, is for security and counterterrorism. Small traces of chemical and biological warfare agents can be detected in airports, stadiums and other safety-critical scenarios [11].

Like every sensor, a transduction mechanism is necessary to quantify the specific observable, that in a biosensor is usually the presence or the concentration of a target, and converting it into a measurable signal. Examples of non optical transducers are the microelec-

trodes arrays (MEA) [10], that are mainly used for impedance spectroscopy and for recording the neural activity *in-vitro* and *in-vivo*, and the microelectromechanical systems (MEMS) [12]. In this last category we recall the microcantilevers [13] and the quartz-crystal-microbalances (QCMB) [14], that perform gravimetric sensing exploiting the change in resonance frequency of a vibrating piezoelectric crystal. A commercial system based on MEMS technology is the *VereChip*™, from *Veredus Laboratories*[3].

For what concerns optical diagnostic and sensing, there is a plethora of different techniques [15]. In some specific case, it is possible to adopt spectroscopic techniques, like, for example, absorption, fluorescence or Raman spectroscopy. However, these kind of techniques are either not easily integrated in a chip, or are created for a particular application, limiting their usefulness. The reason is that to detect and discriminate the target, they rely on its specific optical properties. A more versatile approach is the use of a non-selective optical diagnostic technique, rendered selective by the functionalization of the sensor with biorecognition agents. The strength of this approach is that the transduction and the detection are decoupled, so that a single device can be applied to the sensing of different kinds of targets, just by changing its functionalization. We can divide the techniques that rely on a functionalization layer in two classes: *labeled* and *label-free*.

The former is arguably the most famous and widespread biosensing approach. It is based on the addition of a marker, that binds to the target changing its optical properties. Fluorescence microscopy is a good example of labeled imaging, because target biomolecules are stained (labeled) with fluorescent markers to increase the resolution and the contrast of the microscope image. Another prominent example is the *Enzyme-Linked Immunosorbent Assay* (ELISA), for which the paper of its original proposal [16] has received more than 3550 citations, at the present day[4]. The general concept is the following: the target analyte is immobilized on a substrate, either by direct adsorption or by specific binding to a primary antibody. Then, an enzyme is linked through a secondary complexed antibody, either directly or competitively with the target. Finally, the change in an optical property (usually the color, but also the fluorescence) is detected. There are several variations of ELISA tests: the direct and the indirect la-

[3] Company website: `http://vereduslabs.com/`

[4] Source: Google Scholar

beling, the "sandwitch" and the competitive approaches. ELISA-based technologies are very mature, with demonstrated applications in which microarrays with up to several thousands sensing sites have been realized [17]. In addition the availability of cheap and mass production test-kits, with easy handling procedure (so to be used by untrained personnel), is an evidence of the great versatility of this labeling approach. A clear example is the lateral-flow strip test [18], which find applications from the pregnancy tests to the routine laboratory analysis. Always related to ELISA-based sensing, we recall the (electro)chemiluminescence approach [19] and the fluorescence lifetime imaging.

Finally, we recall here two important labeled sensing methods that do not require a washing step, and that, for this reason, are more suited for homogeneous and real-time probing: molecular beacons and fluorescence polarization immunoassays [20]. The former are very sensitive and selective, but can be applied only to the sensing of single-strand DNA sequences. The latter is less sensitive, but it can be used to detect many different kinds of small biomolecules, like hormones, toxins, drugs and explosives. While labeled detection is highly sensitive, with detection limit down to a single molecule [21], it suffers from laborious and costly labeling processes. In addition, the labels may functionally interfere with the target biomolecule, which can be disadvantageous in drug research.

With the term label-free we indicate the class of biosensing approaches complementary to the labeled detection. In this case, the sensor is functionalized with antibodies, oligonucleotides, aptamers [22] or molecularly imprinted polymers (MIP) [23, 24], and traps the target biomaterial on its surface. Thus, the biorecognition is achieved only by the trapping agent, without the need for an additional marker. The physical transduction is then necessarily based on optical properties of the target itself, e.g., on its molecular polarizability (and, hence, on its refractive index). This approach is inherently different than spectroscopic ones, as the change of this optical property is used to *quantify* the analyte, whereas its *discrimination* is achieved by the functional layer. There are many optical devices that can be used as sensitive label-free biosensors [25]. The most mature technology, and probably, the *de-facto* standard for label-free optical analysis, is *Surface Plasmon Resonance* (SPR) [26]. A surface plasmon wave is a charge density oscillation that occurs at the interface of two media with dielectric constants of opposite signs, such

as metal/dielectric interfaces. Among several coupling mechanisms, the most widely used is the prism coupler: basically, the resonance condition is found when the transverse component of the propagation constant of laser light impinging from the prism side equals the propagation constant of the surface plasmon wave. For a fixed wavelength this condition is achieved only at a specific incidence angle, or, complementary, at fixed angle the condition imposes a certain laser wavelength. When the boundary conditions change due to the surface adsorption (or binding) of a target molecule, the resonance angle or the resonance wavelength shift accordingly, so that they can be used as a transduction signal. Liedberg proposed and demonstrated, for the first time in 1983, the use of this kind of sensors to detect fractions of monolayers of antibodies [27]. Since then, this technique has evolved considerably, and nowadays it is involved in several commercial apparatus, the most famous ones being sold by the company *Biacore*[5]. Moreover, several papers are now reporting about multiplexed SPR biosensor chips [28], with more than 10.000 sensing sites [29].

Whispering Gallery Mode (WGM) resonators are, arguably, the most promising competitor to SPR biosensors. They are entirely made with low-loss dielectrics, and for this reason their resonances are much sharper and more resolved than SPR. Despite being a known effect in dielectric optics since the 1960s [30], the use of a small WGM resonator for biosensing applications made its first appearance only recently [31]. WGM resonators are appealing both for the very high quality factor that they can exhibit [32], as well as for the possibility of miniaturization down to few tens of micrometer in diameter. They are easily integrated with photonic waveguides to allow the realization of complex systems [33, 34]. Moreover, their sensitivity does not depend on the size of the resonator, so that the down-scaling of the system is favourable, in comparison to several other competing technologies. This scaling law, in combination with the high spectral resolution, led to the demonstration of single particle detection (a single InfA virus) [35, 36], although the size (50 nm radius) and the mass (5×10^{-16} g) of the particle were still large compared to many biomarker of interest. Eventually, also the single protein detection has been demonstrated in a hybrid plasmonic-enhanced WGM resonator [37, 38]. Also in the case of

[5] Company website: https://www.biacore.com/lifesciences/index.html

WGM biosensor, some commercial apparatus are appearing on the market, with up to 128 multiplexed sensing sites (and no cross-talk) as in the case of the *Maverick* system, from *Genalyte*[6].

Other competing technologies for the label-free detection are the integrated interferometers [39], either in Young (YI) or Mach-Zehnder (MZI) configuration. As opposite to WGM resonators, these sensors do not scale well, and they are usually made with sensing arms as long as several centimeters. On the other side, this feature makes possible the precise control of the sensitivity of the apparatus, and one can engineer the size of the sensor depending on the application. Despite the fact that very low detection limits have been demonstrated using these devices [40], larger sample volumes are necessary to cover the whole sensor, and single-molecule detection can not be foreseen.

Finally, a special mention has to be reserved for biosensors based on optical fibers. Thanks to their small size, their flexibility and mechanical robustness and to their inherent property of light guiding with low losses, these photonic device are excellent candidates for remotely sensing or for *in-vivo* biosensing. They can be the optical equivalent of electrodes, and, in fact, the term optrode has been introduced. Despite the light guiding for spectroscopy applications or for labeled detection [41], fibers can be employed also for label-free detection. Two examples are the fiber Bragg grating (FBG) and the photonic crystal (PhC) fibers [42], which show reflection spectra or mode confinement loss spectra that are dependent on the refractive index of bound particles. In addition, PhC fibers can be fabricated with a hollow core, so that the specific functionalization can be made directly in the holes, sensibly increasing the light-matter interaction.

There are many other optical techniques that can be applied to the detection of target biomolecules. However, due to this wide variety, an exhaustive treatment is far beyond the scope of this thesis. The reader can find additional information elsewhere [15, 3].

Motivations

As explained in this brief introduction, silicon photonics is arguably the most promising technology to develop highly integrated, multiplexed biosensors. Moreover, the use of silicon nitride, Si_3N_4, and

[6]Company website: `http://genalyte.com/`

silicon oxynitride, SiO_xN_y, extends the possible range of light guiding and sensing to the visible spectrum. This enables the on-chip integration of silicon-based photodetectors, and the use of fluorescent markers for labeled detection. For this reason, in the last years the Nanoscience group of the University of Trento investigated the use of silicon-based waveguides to realize labeled biosensors to be operated in the visible [43, 44]. In this approach, the evanescent wave of the guided mode was used to both excite and collect with high efficiency the fluorescent specific biomarkers. These works were funded by the local government *Provincia Autonoma di Trento* PAT, in the framework of the *FU-PAT NAOMI* project. One of the drawbacks and limitations of this technique was the background noise due to the scattered light, mainly generated at the interfaces of the reaction wells. To circumvent the issue, we started to investigate the use of resonant WGM cavities as an alternative approach, more robust to intensity fluctuation and noise.

This new research activity provided an important role within the scope of the FP7 European project *Symphony "integrated SYsteM based on PHOtonic microresonators and microfluidic components for rapid detectioN of toxins in milk and dairY products"*, grant number 610580 [7]. The Description of Work [45] of the project states that

> "The objective of the Symphony project is the development of a system for the detection of aflatoxin M1 in milk for the dairy industry. [...] the Symphony project will deliver and test in real settings a smart heterogeneous integrated system by the integration of key enabling technologies such as micro-nano-bio-systems and photonics, polymer-based technologies for low-cost microfluidics and Si-based photonic structures".

Aflatoxin M1 is a milk contaminant and potent carcinogen classified in group 1 of the International Agency for the Research on Cancer (IARC, 1993). The European Commission regulation (EC) No. 1881/2006 specifies the maximum level of aflatoxin M1 contamination in milk to 50 ppt ($50\,pg\,ml^{-1}$), and to 25 ppt ($25\,pg\,ml^{-1}$) for infant formulae. Thus, this project is aimed at the realization of a

[7] Project website: `http://symphony-project.eu/`

complex system, where the sensor has to provide smart functionalities, in terms of multiplexing, reuse and integration with the rest of the apparatus, together with ultra-sensitive detection limits.

The need for an integrated system, with cheap light sources and detectors, motivated the choice of silicon-based and CMOS-compatible materials, to be operated at wavelengths in the VIS-NIR range. At the same time, the required low detection limits motivated the investigation and exploitation of two promising candidate technologies, i.e., WGM micro resonators and MZIs. As previously anticipated, the former is appealing for its scaling law: ultra-sensitive detection can be achieved irrespectively to the resonator size, so that a large number of sensors can be fit on a small chip. On the other side, the latter is favourable exactly for the same scaling law: if the detection limit of the WGM resonator will result not sufficient for the purposes of the project, a larger MZI is expected to provide the required specifications.

Motivated by these considerations, this thesis is devoted to the design, development and experimental characterization of a silicon-based label-free biosensor. The main focus is given to the applications of WGM microresonators, but we also test and compare MZI-based biosensors.

Document Structure

This document is structured in four chapters, based on the following contents.

Chapter 1 gives to the reader a general theoretical background, that entails the models and equations used to describe the biosensors. It covers both the description of the kinetic of the binding reaction, that selectively recognize the analyte molecules, and the description of the photonic sensors, that transduce the binding in a measurable signal. Section §1.2.2, in particular, details the numerical methods that I have adopted to accurately and efficiently simulate the sensing properties of the WGM resonators.

Chapter 2 reports on the development and characterization of the experimental apparatus. Here, I realized and tested four optical setups, for the rapid measurement of the photonic sensors at 780, 850 and 1550 nm. In addition, I also realized the systems for the thermal control of the sample and the fluid handling at the micro-litre scale.

Chapter 3 focuses on the design of the test- and sensor-chips, developed by me and Dr. Guider Romain of the University of Trento (UniTN) and fabricated by the Fondazione Bruno Kessler (FBK) within the scope of the Symphony project. The chapter is divided in sections that cover the design of the waveguides, the splitters, the ring resonators and the fiber butt-coupling.

Chapter 4 describes the optical characterization of both *Micro Ring Resonators* (MRRs) and *Asymmetric Mach-Zehnder Interferometers* (aMZIs) devices. The measurements have been performed by me and Dr. Guider, partially supported by the bachelor student Rougemond Alexis. We test the compliance with the design parameters and the performances in terms of bulk refractive index sensing. In addition, this chapter reports also on the first successful experiments involving specific detection of Aflatoxin-M1 in buffered solutions. During this set of experiments I trained and I received a partial support by the new Ph.D. student Chalyan Tatevik. Within the chapter, I compare our sensors to state-of-the-art competing technologies, proving their effective potential for the realization of an integrated and ultrasensitive label-free biosensor. Moreover, I model and analyze the binding reaction kinetics, evaluating the kinetics rate constants and the superficial sensitivities of our sensors.

Finally, appendix §A shortly reports on the procedures for the surface functionalization and for the preparation of the buffer and regeneration solutions, while appendix §B explains the algorithms that I have implemented for the realtime acquisition of the spectral features used as sensing signals.

Theoretical background 1

1.1 Optical biosensing principles

This section provides the theoretical basis to understand the biological and physical principles behind optical biosensors. We will focus on the label-free devices that have been studied in this thesis, but we will also compare some of their characteristics with competing technologies. We will first describe the biorecognition agents and mechanism, which are necessary to provide specificity to the sensor. Then, we will move to the physical transduction mechanisms, and we will give the definitions used to characterize and compare different devices.

1.1.1 Biorecognition agents

Selectivity is the ability of a (bio-)sensor to recognize preferentially a certain analyte, or class of analytes, even in presence of other interfering species. *Specificity* is the ultimate of selectivity [46], i.e., the ability of the sensor to respond only to its target. If an optical technique is not inherently selective, it can still be used as the building block for many different biosensors. To bring selectivity to the measurement we need to functionalize the sensor, by means of a biorecognition agent. The advantage of separating the transduction from the

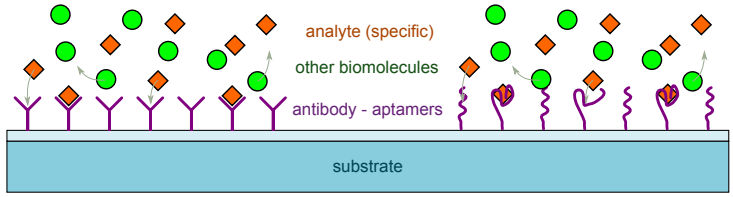

Figure 1.1: Representation of the biorecognition mechanism, by means of antibodies and DNA-aptamers. Since the binding is selective, only the target analyte can be captured, while other biomolecules can not form a stable complex. The progressive trapping of molecules produces a layer with high surface concentration of analyte.

biological functionalization is double. First, the same optical sensing technique can be reused for applications with different targets, eventually enabling multiplexed analysis on a single instrument. Second, the development and the optimization of a certain selective receptor molecule can be employed on different devices.

In biology, there are numerous examples of biorecognition mechanisms that can form complexed structures. Just to name a few, we recall receptor-ligand, antigen-antibody, RNA-ribosome as naturally-occurring examples. In addition, there are some artificial techniques that have been developed for the realization of selective bindings. One is the molecular imprinting, which is receiving attentions since 1931 [24, 23]. Another one, and probably a real breakthrough of the modern years, is the *SELEX* process, which enables the realization of DNA- or RNA-aptamers [47].

Antibodies are at the heart of immunological assays, and have been employed for molecular recognition since the 1950s. Their Y-shaped structure ends with two particular *paratopes*, which can bind to their specific *epitopes* through the so-called key-lock mechanism. Despite their widespread use, DNA-aptamers are emerged as rivals in the field of diagnostics [22]. Here, we summarize the main advantages of aptamers over antibodies:

- selection and production of aptamers are faster and cheaper;
- thanks to the *in-vitro* selection, it is possible to obtain aptamers which are more suited for *in-vitro* diagnostics;

- it is possible to realize selective aptamers for toxins and other molecules which are not compatible with the *in-vivo* selection;
- the chemical synthesis allows for high accuracy and reproducibility of the aptamers production;
- functional groups or reporter molecules can be attached in engineered locations;
- aptamers are stable to long-term storage;
- their denaturation is reversible, allowing for regeneration of the active sensing site;
- the small dimensions are suitable for a high-density coverage of the sensor.

The functionalization of a biosensor can be divided in two steps. The first is an activation, or a pre-coating, which is necessary to expose on the surface of the sensor a pre-determined functional group. For silica-based biosensors, we can recall the silanization technique [48], the coating with copolymers [49] and the photochemical attachment of alkene-derived monolayers [50]. Then, the immobilization of the bio-recognition agent is obtained by means of a chemical reaction, which creates covalent bonds between the exposed functional group and the correspondent group at the end of the DNA-aptamer [51]. If needed, a final step of passivation could be performed, in order to block all the exposed functional groups which did not react with any bioreceptor.

1.1.2 Reaction kinetics

Once the surface of the biosensor has been functionalized to provide selectivity, the sensor can be used to detect the target molecules. The association reaction, which leads to the formation of analyte-receptor complexes, is actually a dynamic process, governed by a thermodynamic equilibrium. In its simplest form (one-to-one reaction), this can be expressed as

$$\mathrm{A} + \mathrm{R} \underset{k_d}{\overset{k_a}{\rightleftharpoons}} \mathrm{AR} \tag{1.1}$$

where A is the analyte, R is the receptor, AR is the bound complex and k_a and k_d are the association and dissociation rate constants.

The reaction kinetic is modelled with a first order differential equation, that expresses the rate of surface adsorption:

$$\begin{cases} \dfrac{d[\mathrm{AR}]}{dt} = k_a[\mathrm{A}][\mathrm{R}] - k_d[\mathrm{AR}] \\ \dfrac{d\big([\mathrm{AR}] + [\mathrm{R}]\big)}{dt} = \dfrac{d\sigma_0}{dt} = 0 \end{cases} \tag{1.2}$$

where the square bracket operator $[*]$ denotes the concentration of the compound. The latter equation is valid in the case of immobilized receptors, where the total surface concentration of receptors (occupied or not) is constant to σ_0.

By expressing the surface concentration of the complexed molecules, AR, in terms of surface coverage $\theta \in [0, 1]$, we have

$$\begin{cases} \dfrac{d\theta}{dt} + (k_a[A] + k_d)\theta = k_a[\mathrm{A}] \\ [\mathrm{AR}] = \theta\sigma_0 \end{cases} \tag{1.3}$$

The differential equation can be solved analytically. In particular, during the association phase of a bio-assays we have that the initial condition is $\theta_0 = 0$, and that the analyte concentration is constant throughout the reaction $[\mathrm{A}](t) = C$. In such case, we obtain

$$\theta(t) = \frac{k_a C}{k_a \cdot C + k_d}\left[1 - e^{-\left(k_a \cdot C + k_d\right)t}\right] \tag{1.4}$$

It is interesting to notice that the initial rate of covering

$$\left.\frac{d\theta}{dt}\right|_{t=0} = k_a C \tag{1.5}$$

is proportional to the concentration. Thus, if the objective of the assay is the estimation of the analyte concentration, a fast method is the evaluation of the signal slope at the beginning of the incubation.

If the assay is protracted for a sufficiently long time, the sensor reaches an equilibrium condition. The rate of the association reaction equals the rate of the dissociation one:

$$k_a[\mathrm{A}]_{eq}[\mathrm{R}]_{eq} = k_d[\mathrm{AR}]_{eq} \tag{1.6}$$

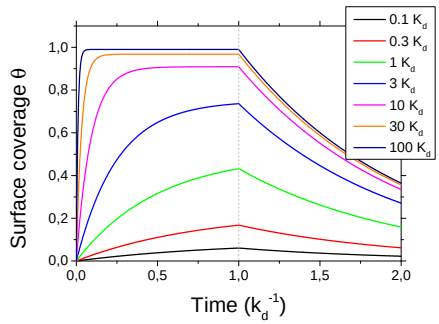

FIGURE 1.2: Surface coverage $\theta(t)$, as a function of assay time (normalized to k_d^{-1}) and analyte concentration (normalized to K_d). The analyte is removed at $t_0 = k_d^{-1}$. To show comparable time-scales in the association and dissociation phases, we set the dissociation constant $K_d = 0.1\,\mathrm{M}$. In the more realistic case of $K_d \ll 1\,\mathrm{M}$, the time scale of the dissociation phase will be much longer than the one of the association phase.

By defining the dissociation constant $K_d = \frac{k_d}{k_a} = \frac{[\mathrm{A}]_{eq}[\mathrm{R}]_{eq}}{[\mathrm{AR}]_{eq}}$ we can find the surface coverage at equilibrium as

$$\theta_{eq}^{-1} = \frac{k_a \cdot C + k_d}{k_a C} = 1 + \frac{K_d}{C} \tag{1.7}$$

Notice that the sensor can saturates its binding sites only if $C \gg K_d$.

When, at a certain time t_0 from the beginning of the bio-assay, the flow of analyte is ended, the dissociation phase of the reaction starts. Since we have $[\mathrm{A}] = 0$, the solution to the differential equation for $t > t_0$ becomes

$$\theta(t) = \theta(t_0)e^{-k_d(t-t_0)} \tag{1.8}$$

Figure 1.2 shows the calculated surface coverage curves of complete assays (association and dissociation phases) at various analyte concentrations.

One of the peculiarities of *label-free* biosensors is their ability to measure in real-time the binding of the analyte. The output signal is proportional, through the transfer function of the sensor, to the surface coverage θ. Therefore, a label-free bio-assay signal resembles one

of the curves of Figure 1.2. By fitting the model, Equation (1.4) and Equation (1.8), to the experimental measurements at various concentrations, it is possible to calculate the association and dissociation rate constants, k_a and k_d. A study comparing the measured K_d of bio-assays conducted with different receptor types, showed that aptamers can outperform antibodies and lead to lower detection limits [52].

1.1.3 Biosensor physical transduction

As stated in §1.1.1, the bio-recognition of an analyte is just one aspect of the sensing method. In order to be able to detect and quantify the target molecules, a transduction mechanism is needed. For what concerns optical biosensors, some examples of signals that can be monitored are the color (or the absorbance at some specific wavelength), the refractive index, the polarization of the light and the luminescence of signalling molecules.

In addition, the transduction methods can be divided in *labeled* and *label-free*. The first one exploits the addition of another signalling molecule, like a fluorophore [44], that has to be selective for the analyte. Thus, in this case the biorecognition is performed twice: during the immobilization and during the labelling, making the labeled approach more selective but, in principle, less sensitive. The second method relies solely on the presence of the immobilized target. During this thesis, we focused mainly on the label-free approach, in particular exploiting the change of refractive index induced by the trapped particles.

During the immobilization, in fact, the analyte is concentrated on the surface of the sensor, replacing pre-existing water (or buffer) molecules. This exchange of material produces local variations in the refractive index. If the trapping is performed on a waveguide, the bound particles can interact with the evanescent wave of the confined light. As represented in Figure 1.3, the tail of the evanescent wave rapidly decays within few tens or hundreds of nanometers. For this reason, they are particularly suited to detect local variations in refractive index, without being affected by fluctuations far in the bulk.

The guided light propagates with phase velocity $v = c/n_{eff}$, where c is the speed of light in vacuo and n_{eff} is the effective refractive index. The latter is a weighted average of the real indexes in contact with the light, which depends also on materials bound on

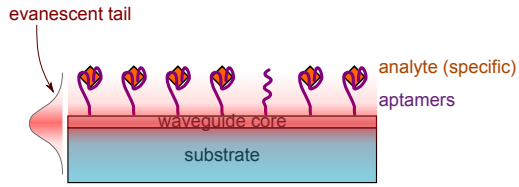

FIGURE 1.3: Schematic drawing of the evanescent wave interacting with the captured molecules. The presence of the analyte perturbs locally the refractive index. The evanescent tail, which decays exponentially in few tens or hundreds of nanometers, is suited to sense this local perturbations, while being almost insensitive to fluctuations far in the bulk.

the surface. Hence, to accurately measure the adsorption of the analyte, it is possible to measure the phase shifts of the guided light. This can be accomplished by means of interferometric measurements or by monitoring the spectral shifts of WGM resonances. This two methods will be explained in more details in §1.2 and §1.3.

1.1.4 Sensors characteristics

We conclude this section by giving some useful definitions, which will be used throughout the thesis to characterize our biosensors. The first one is the *sensitivity*, which quantifies the sensor's output signal produced by a unitary variation at the input. In the case of label-free biosensors based on WGMs, the measured output is the resonance wavelength, λ_0, of an optical resonator. Thus, in this case the spectral sensitivity to variations of the refractive index, n_s, in the bulk sensing volume is given by

$$S_{b,\,\mathrm{WGM}} = \frac{\partial \lambda_0}{\partial n_s} \tag{1.9}$$

Similarly, in the case of *Mach-Zehnder Interferometers* (MZIs), the measured quantity is the phase ϕ_0 of the interferometric pattern. Therefore, we will define *sensitivity* the quantity

$$S_{b,\,\mathrm{MZI}} = \frac{\partial \phi_0}{\partial n_s} \tag{1.10}$$

As we will see later (in §1.2 and §1.3), both these sensitivities are proportional, through geometrical factors, to the intrinsic sensitivity,

which is given by

$$S_{b,\,i} = \frac{\partial n_{eff}}{\partial n_s} \tag{1.11}$$

The second definition is the *Limit Of Detection* (LOD), which represents the minimum amount of input that can be distinguished with a certain confidence level. If the sensitivity is S, and σ_0 is the standard deviation of repeated measurements of blank solutions, then the LOD can be calculated as

$$\mathrm{LOD} = \frac{k\sigma_0}{S} \tag{1.12}$$

IUPAC recommends the use of $k = 3$, which sets the confidence level to 99.7 % [53].

Despite its intuitive meaning, the LOD is affected by instrumental uncertainties, which can arise in any component of the whole sensor: temperature and fluid control, purity of carrier buffers and analyte, laser source, etc. For this reason, a fair comparison of single elements on different apparatus is not easily defined. However, it is possible to show that the LOD is lower-bound by the *Signal to Noise Ratio* (SNR) of the light intensity, and by a *Figure Of Merit* (FOM) which depends only on the characteristics of the transducer [54]. In the case of a WGM sensor with quality factor Q (and full-width at half-maximum $\delta\lambda$), we can define

$$FOM = \frac{QS}{\lambda_0} = \frac{S}{\delta\lambda} \tag{1.13}$$

where, as before, S is the sensitivity and λ_0 is the resonance wavelength.

In alternative, some authors prefer the use of the "intrinsic LOD", ILOD, defined as $\mathrm{ILOD} = FOM^{-1} = \lambda_0/QS$ [55]. This definition of FOM is also used for SPR or photonic crystal cavity sensors [56, 57]. Thus, it is an ideal parameter for comparing the intrinsic performances of the transducers, even for (bio-)sensors relying on different technologies.

1.2 Whispering Gallery Mode resonators

As explained in section §1.1.3, one of the physical effect that can be exploited for the transduction in a biosensor is the change of re-

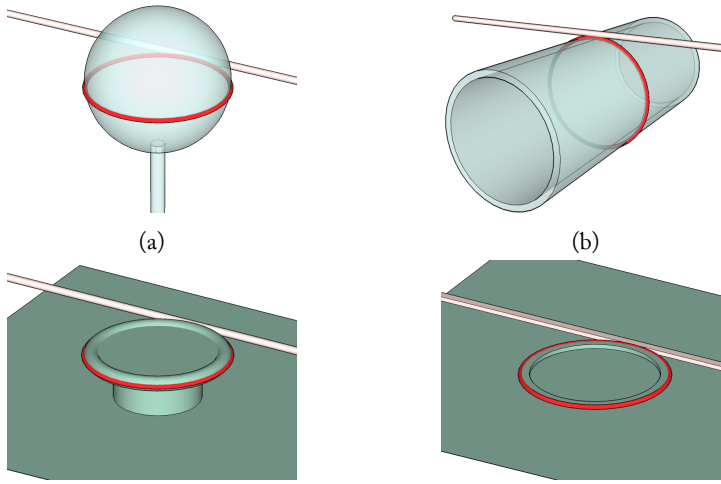

FIGURE 1.4: Few examples of WGM microresonators: (a) silica microsphere, (b) silica microcapillary, (c) silicon microtoroid and (d) silicon microring. (a),(b) and (c) are coupled through an external tapered optical fiber, whereas (d) is coupled through an integrated bus waveguide. The red circles represent the excited WGMs.

fractive index. In this section, we will see how particular structures, namely the WGM resonators, can be used to measure such variable.

A WGM is formed when light of a given wavelength, confined by means of total internal reflection, is forced to travel in a closed loop. In this case, the light interferes with itself and, if the interference is constructive, the field builds up in the cavity. The eigenmodes that satisfy this constructive interference are called WGM. There are various devices that can produce WGMs [58, 59]. The simplest is an optical fiber spliced with itself, forming a fiber loop (or fiber ring) resonator [60]. Other examples are (see Figure 1.4):

- **Microspheres**, formed by the melting and re-solidification of a dielectric, which commonly is the silica glass of an optical fiber tip [31, 48]. These are easily fabricated, and due to the ultra-smooth surface finishing, they exhibit very low losses. How-

ever, their integration in optical chips is intrinsically very challenging.

- **Microcapillaries or microbubbles**. Here the WGM is formed on the outer interface of the capillary, whereas the liquid to be sensed flows into the inner part of the capillary. Therefore, the thickness of the capillary must be sub-micrometric, in order to have a significant mode overlap with the analyte. When this is achieved, the sensitivities of microcapillary-based sensors can outperform standard WGM sensors [61]. Despite the inherent integration with microfluidics, their fabrication and scalability are even harder than microspheres.

- **Microdisks and microrings**, fabricated by means of photolithography [62]. They suffer from higher losses due to the roughness of the surfaces, but their small volume and their fabrication method make them suitable for dense integration in optical chips for multiplexed analysis [9, 63]. The optical coupling to the sensor is achieved by means of integrated bus-waveguides.

- **Polished crystal macrodisks**. These are definitely the structures that exhibit the highest quality factors (see Equation (1.24) for the definition), but their integration is probably even more challenging than microspheres. Moreover, due to the macrometric size, the overlap between the mode and the analyte solution is minimal, leading to very low sensitivities [64].

- **Microtoroids**, i.e., melted and re-solidified suspended microdisk. The surface tension during the fusion process gives ultrasmooth surface finishing, as for the case of microspheres, leading to low losses [65]. However, even if they can be mass-fabricated in dense optical chips, their coupling with optical waveguides is not obvious, and for this reason they can only be addressed individually by means of tapered optical fibers.

- **Wedge microresonators**, which are the best compromise between surface quality and integrability [66, 67]. Similarly to microdisks, they are fabricated through photolithography, but the resonator definition is achieved by a wet etching process, which produces smoother surfaces. With a proper engineering of the fabrication process, it is possible to monolithically

integrate both the resonator and the coupling waveguide [34], enabling the possibility to have dense array of multiplexed sensors.

During my Ph.D., I worked with microdisks, microrings and wedge resonators. The next sections will present the mathematical formalism necessary to describe and analyze a biosensor based on these structures.

1.2.1 Microdisks and microrings

MRRs are just a "small-scale" version of the fiber ring resonators: a bent single-mode waveguide, closed on itself, and forming a ring. If the waveguide is widened towards the central point of the ring, eventually forming a microdisks, it will support multi-modal propagation. The modes with grazing light near the outer edges of the structure will be confined by total internal reflection, and will circulate in a similar fashion to that of the microring. Thus, the model for the description of both structures is the same [68].

In Figure 1.5, we schematize the model. A ring with radius R is coupled to a straight waveguide. The field amplitudes in the waveguide and in the ring are labelled with A and B, respectively, while the subscripts 1 and 2 indicate the positions immediately before and after the coupling zone. The propagation constant along the ring is β. The field transmission and coupling coefficients are labelled with t and k, respectively. During the propagation in the ring, the light can undergo various loss mechanisms:

- **absorption losses**, governed by the Lambert-Beer law. The absorbing material can be in the core but also in the cladding (light absorption through evanescent field);
- **radiative losses**, where the light is lost towards the exterior of the resonator due to the finite confinement of the guided light. These becomes predominant when the refractive index contrast is low or when the bend radius is short;
- **surface scattering** due to the roughness on the exterior sidewall of the resonator. This scattering is accentuated in bends because the mode is pushed towards the sidewall of the waveguide.

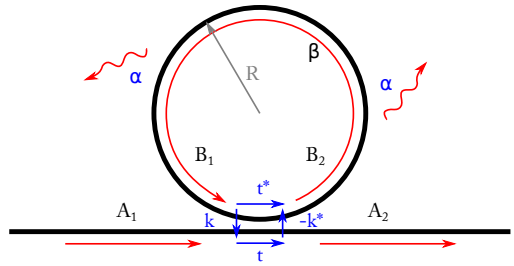

Figure 1.5: Schematic model of the WGM ring resonator. The field amplitudes in the waveguide and ring are labelled with A and B, respectively. The subscripts label the positions immediately before (1) and after (2) the coupling zone. The field transmission and coupling coefficients are labelled t and k, respectively. The propagation constant inside the ring is β, while the radius of the ring is R. Losses are schematized by the wavy arrows and coefficient α.

- **surface absorption**, similar to the bulk absorption but localized near the surface of the resonator (where more contaminants can be present). Similarly to the previous loss mechanism, also in this case the losses are accentuated with decreasing bend radius.

In our model, all these losses are taken into account through a comprehensive attenuation coefficient $\alpha = \sum_i \alpha_i$, where i labels the contributions of absorption, radiation, surface scattering and surface absorption.

The field amplitudes are linked through the following system of equations:

$$\begin{cases} A_2 = tA_1 + kB_1 \\ B_2 = -k^* A_1 + t^* B_1 \\ B_1 = e^{-\alpha\pi R} e^{i2\pi R\beta} B_2 = a e^{i\theta} B_2 \end{cases} \tag{1.14}$$

where we introduced $a = e^{-\alpha\pi R}$ and $\theta = 2\pi R\beta$ for simplifying the reading. Solving the system for A_2/A_1, we can find the expression

for the field transmission,

$$\frac{A_2}{A_1} = \frac{te^{-i\theta} - a}{e^{-i\theta} - at^*} \tag{1.15}$$

while solving for B_1/A_1 we get

$$\frac{B_1}{A_1} = \frac{-ak^*}{e^{-i\theta} - at^*} \tag{1.16}$$

From these, we can calculate the transmission coefficient T

$$T = \left|\frac{A_2}{A_1}\right|^2 = \frac{|t|^2 + a^2 - 2a|t|\cos(\theta + \phi_t)}{1 + |t|^2a^2 - 2a|t|\cos(\theta + \phi_t)} \tag{1.17}$$

and the cavity intensity build-up I

$$I = \left|\frac{B_1}{A_1}\right|^2 = \frac{a^2(1 - |t|^2)}{1 + |t|^2a^2 - 2a|t|\cos(\theta + \phi_t)} \tag{1.18}$$

where ϕ_t is the argument of the complex transmission coefficient t.

We notice that these equations are periodic in θ, with period 2π. We also notice that the cavity resonates (i.e., I is maximum) when

$$\theta + \phi_t = m2\pi \tag{1.19}$$

with m some integer number, called the *azimuthal mode number*. When $R \gg \beta^{-1}$, which is the typical case for microrings and microdisks, we have that $\theta \gg \phi_t$ and that $\theta \approx m2\pi$. Thus, the effect of the argument ϕ_t is just a detuning of the resonance spectral position, near its "intrinsic" position.

The intrinsic spectral resonance condition is given by

$$\lambda_m = \frac{2\pi R}{m} n_{eff} \tag{1.20}$$

where we used the *effective refractive index* n_{eff} because the mode is confined and guided. Please note that the exact calculation of n_{eff}, which is wavelength dependent and also depends on the geometrical details of the resonator, requires the solution of the Helmholtz equation, which can be obtained analytically in simple geometries [69], or numerically in more complex cases [70]. We will see later how to calculate this value with a *Finite Element Method* (FEM) solver.

When n_{eff} is known, the transmission spectrum Equation (1.17) can be evaluated.

Figure 1.6(a) reports a simulated transmission spectrum, obtained using Equation (1.17). We can recognize the sharp resonance features as transmission dips. The spacing between them is called *Free Spectral Range* (FSR), and can be calculated from Equation (1.20):

$$\mathrm{FSR} \approx \frac{\lambda^2}{2\pi R n_g} \tag{1.21}$$

Here we used the group index $n_g = n_{eff} - \lambda \frac{\partial n_{eff}}{\partial \lambda}$ because of the wavelength dependence of n_{eff}.

The *Extinction Ratio* (ER) can be obtained by the value of the transmission at resonance:

$$\mathrm{ER}^{-1} = T(\lambda_m) = \frac{(a - |t|)^2}{(1 - a|t|)^2} \tag{1.22}$$

Notice that the transmission vanishes (and ER is infinite) only if

$$|t| = a \tag{1.23}$$

This is said the *critical-coupling condition*. When this is satisfied, the light field in the cavity interferes perfectly and destructively with the light transmitted in the waveguide, which is the reason why the transmission drops to zero. Other possibilities are the *under-coupling condition* ($|t| > a$) and the *over-coupling condition* ($|t| < a$). In either cases, the transmission does not vanish at resonance, as we can see also from Figure 1.6(b).

The finite width of the resonances is given by the losses. For an ideally lossless resonator ($a = 1$), the resonance width would become infinitesimal and the transmission would be identically $T = 1$. Instead of using the full-width at half-maximum, it is more common to report the *quality factor* Q of a resonator, which can be calculated as

$$Q = \frac{\lambda_0}{\Delta\lambda_{\mathrm{FWHM}}} \tag{1.24}$$

To probe the WGM resonances and measure the Q value, one needs to couple the light with a waveguide (or a tapered fiber), as from the model herein analyzed. The presence of this coupling perturbs the cavity modes, as it can be seen from the dependence of

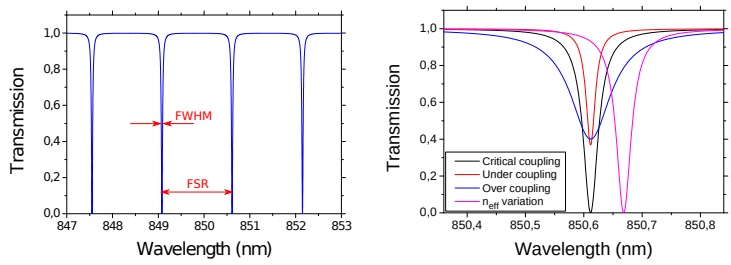

(a) (b)

FIGURE 1.6: (a) Simulated spectrum of a critically-coupled WGM resonator. (b) Comparison of the resonances of WGM resonators in different coupling conditions or subjected to a small variation in refractive index n_{eff}.

Equation (1.17) from t. The side effect is that the measured Q is higher in undercoupling regime and lower in overcoupling regime (see Figure 1.6(b)). It can be shown [71] that the loaded (measured) quality factor Q_l can be divided in two contributions:

$$Q_l^{-1} = Q_c^{-1} + Q_0^{-1} \tag{1.25}$$

where Q_0 is the intrinsic (or unloaded) quality factor, given just by the losses of the cavity itself, and Q_c is the contribution given by the coupling. In particular, the latter can be expressed as

$$Q_c = \frac{2Q_l}{1 - \sqrt{T_{\min}}} \tag{1.26}$$

where $T_{\min}$ is the minimum of the measured resonance transmission spectrum.

Notice that in critical coupling $T_{\min} = 0$, so that $Q_l = \frac{1}{2}Q_0$. With this observation we can finally calculate Q_0 [72]. From Equation (1.17), when $|t| = a \approx 1$, we have

$$Q_0 = \frac{2\pi n_g}{\lambda \alpha} \tag{1.27}$$

As previously said, the attenuation coefficient α is comprehensive of all the internal loss mechanisms.

1.2.2 Numerical methods for mode analysis

The analysis exposed in the previous section gives interesting insights into the physics of WGMs resonators, but it is not suitable for accurate calculations. In particular, the value n_{eff} is assumed as known, but there are no closed-form equations for its calculation in the general case. For accurate calculations, one has to solve the Maxwell's equations, and in particular the Helmholtz equation, for every specific structure (i.e., for a specific spatial distribution of refractive index $n(\vec{r})$) and boundary condition.

In the case of microspheres, their special (spherical) symmetry leads to analytical solutions. Similarly, for the particular class of WGM resonators in which we can find an axial symmetry, we can reduce the complexity of the numerical calculation, as explained in [70]. Most of the more important microresonators belong to this category. We can model rings, disks, toroids, wedges, microcapillaries and also spheres (useful as a test-bench).

In this thesis, we use the FEM solver *Comsol Multiphysics*, and in particular the Wave Optics Module, to calculate the axisymmetric eigenmodes supported by our structures. There are two possible kinds of analysis that can be used [73]:

- *Mode analysis*, in which the user is required to input the operating frequency. In this case the mode profiles are solved without any particular symmetry condition at the boundary of the azimuthal coordinate (i.e., the structure is a bent waveguide, but not a loop), and the calculated eigenvalue is the propagation constant or, equivalently, the effective index n_{eff}.

- *Eigenfrequency*, in which the user is required to input the azimuthal mode number. In this case, the mode profiles are solved imposing periodic conditions at the boundary of the azimuthal coordinate (i.e., the structure is a complete loop), and the calculated eigenvalue is the resonant frequency.

Both methods have pros and cons: with the latter, the user is guarantee to calculate the real WGMs, but it is not easy to estimate in advance the azimuthal mode number corresponding to a resonance near a desired wavelength. With the first, the wavelength is fixed, but the modes that are calculated are not exactly the WGMs. For big resonators, which have a small FSR (see Equation (1.21)), the density

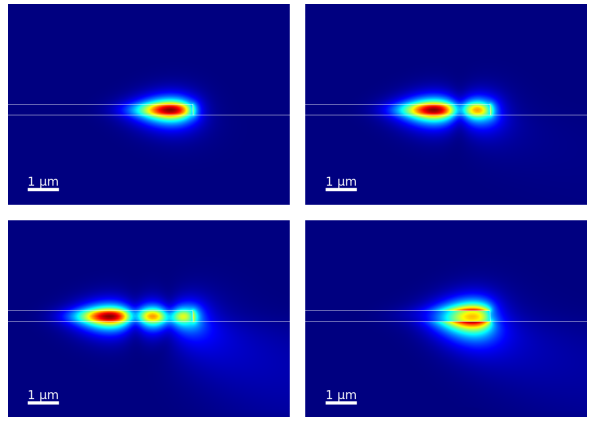

FIGURE 1.7: "Mode analysis"-calculated electric field magnitude for WGMs of a disk resonator. The plots represent resonances of the first, second and third radial families of TE modes, as well as for a resonance of the first radial family of TM modes.

of modes is such that the profiles calculated with the first analysis are normally a sufficient approximation of the closest WGM.

In Figure 1.7 we show, as an example, the supported modes of a thin amorphous SiN_x disk, with resonance wavelengths near 1540 nm. Besides the fundamental *Transverse Electric* (TE) and *Transverse Magnetic* (TM) modes, we also observe the presence of higher order radial TE modes. They differ in their electric field spatial distributions, but also in their azimuthal mode numbers m and effective indexes n_{eff}.

Once that the mode profile and the effective refractive index of a particular resonance are solved, we can calculate the quality factor Q and the sensitivity S of that WGM. These are parameters of major interest for a biosensor, because they affect its achievable resolution (here meant as the LOD).

When we add losses in the analysis of our structure, the hermiticity of the eigenvalue problem is broken. Thus, the solutions that the FEM solver calculates are complex-valued [73]. As explained in [74], it is possible to evaluate Q from the complex effective refractive index (mode analysis) or from the complex eigenfrequency (eigenfrequency

analysis) by using the relation:

$$Q_0 = \frac{\Re(\omega)}{2|\Im(\omega)|} = \frac{\Re(n_{eff})}{2|\Im(n_{eff})|} = \frac{\beta}{\alpha} \tag{1.28}$$

where $\Re$ and $\Im$ are, respectively, the real and imaginary part of the complex value, while β and α are the propagation constant and attenuation coefficient, as in Equation (1.14).

We can model bulk absorption losses as the imaginary part of the refractive index (k) of the materials of our model, through the equation

$$k = \frac{\lambda}{4\pi}\alpha \tag{1.29}$$

Similarly, one can emulate surface absorption and surface scattering by adding a thin outer layer to the model, where the value of k is higher than in the bulk material. For what concerns radiative losses, the modelling can be achieved by adding a special kind of absorbing material, the *Perfectly Matched Layer* (PML), to the outer regions of the simulation box [75]. As the name suggests, these regions will absorb the radiation without reflections, mimicking an infinitely long simulation domain.

The other important parameter for a biosensor is its sensitivity S. From the definition, Equation (1.9), one could naively calculate it by running two eigenfrequency simulations, with a small difference in the refractive index of the liquid in the sensing volume. However, there is a more efficient way to calculate it [76]. Let's call V the volume filled by the sensing liquid, and let's assume that the unperturbed refractive index in that volume is n_V. To calculate the bulk sensitivity, S_b, of the resonance with unperturbed wavelength λ_0, we can first notice that

$$\frac{1}{\lambda_0}S_b = \frac{1}{\lambda_0}\frac{\partial\lambda}{\partial n_V} = -\frac{1}{\omega_0}\frac{\partial\omega}{\partial n_V} \tag{1.30}$$

Then, by using the perturbation theory developed in [77, 78], we obtain

$$\frac{1}{\lambda_0}S_b = \frac{1}{2}\frac{\iiint_V \vec{E}^* \frac{d\epsilon}{dn}\vec{E}\, dV}{\iiint_\infty \vec{E}^*\epsilon\vec{E}\, dV} \tag{1.31}$$

$$= \frac{1}{n_V}\frac{\iiint_V \vec{E}^*\vec{D}\, dV}{\iiint_\infty \vec{E}^*\vec{D}\, dV} \tag{1.32}$$

where we have used the equations $\epsilon = \epsilon_0 n^2$ and $\vec{D} = \epsilon \vec{E}$ for the dielectric constant and the electric displacement field, respectively. Finally, we get

$$S_b = \frac{\lambda_0}{n_V} \frac{\iiint_V \frac{1}{2} \vec{E}^* \vec{D} \, dV}{\iiint_\infty \frac{1}{2} \vec{E}^* \vec{D} \, dV} \tag{1.33}$$

Basically, the sensitivity is the fraction of electric energy contained in the sensing volume V, multiplied by the constant λ_0 / n_V. In Comsol, this calculation can be obtained in one step by integrating in V the expression

```
real(lambda0*emw.Weav/(emw.nrr*emw.intWe))
```

where `lambda0` is, obviously, the wavelength λ_0.

When light is confined in a WGM cavity, it is quite common to obtain evanescent tails which extend from the surface of the structure for tens to hundreds of nanometres. When used as label-free sensors, the volume of interaction between the analyte and the WGM evanescent field is very small, and mainly limited by the thickness of the layer of the captured analyte. In the case of nanometric-sized molecules (like proteins), this means that most of the evanescent tail is unperturbed and does not contribute to the signal. For a fair comparison between different structures, it is very helpful to introduce the superficial sensitivity S_s, defined as

$$S_s = \frac{\lambda_0}{n_V} \frac{\iint_{A^+} \vec{E}^* \vec{D} \, dA}{\iiint_\infty \vec{E}^* \vec{D} \, dV} \tag{1.34}$$

where A^+ is the area of the sensor exposed to the liquid. The superscript $^+$ warns that the fields, which are discontinuous at the sensing interface, have to be computed in the exterior part of the geometry.

When dealing with discrete meshes, like in the case of a FEM analysis, the definition of A^+ is bugged. In this case, it is possible to overcome the problem by adding a small layer of volume V and thickness t_V in the outer part of the geometry. Thus, we obtain

$$S_s = \frac{\partial^2 \lambda}{\partial t_V \partial n_V} = \frac{\partial S_{b,V}}{\partial t_V} \approx \frac{S_{b,V}}{t_V} \tag{1.35}$$

where $S_{b,V}$ is the "bulk" sensitivity defined in Equation (1.33) and calculated in the small layer V.

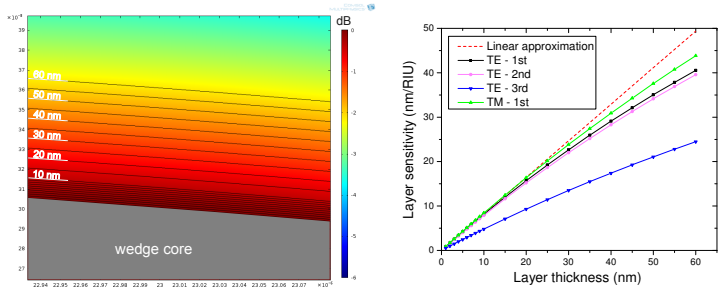

(a) (b)

Figure 1.8: (a) Zoomed view on the cross section of the model used to test the superficial sensitivity. The color-bar represents, in decibel scale, the electric energy density of a WGM mode, normalized to the surface of the sensor. We can notice that the energy halves at a distance $\sim$ 70 nm. (b) "Bulk" sensitivities, Equation (1.33), calculated in layers of increasing thickness t_V from the surface of the resonator. The slope of these curves is the surface sensitivity S_s. Notice that the linear approximation of Equation (1.35) is valid up to $t_V \approx 20$ nm.

The range of validity of the approximation in Equation (1.35) is roughly determined by the results shown in Figure 1.8. In that simulation, we calculated the superficial sensitivity of the WGMs supported by a wedge resonator, for progressively thicker layers above the sensor's surface. In Figure 1.8(b), we see that the layer sensitivity grows linearly up to $t_V \approx 20$ nm. Thus, for t_V smaller than this value, the surface sensitivity S_s can be accurately calculated with this method.

1.2.3 Wedge resonators

Analyzing Equation (1.14), we notice that the model of the coupling mechanism, between the probing waveguide (or tapered fiber) and the WGM resonator, is very general. A commonly adopted way to achieve such coupling is by placing a bus-waveguide in the same horizontal plane of the resonator. However, this choice has some limitations:

- the precise control of the coupling strength requires a high res-

olution, achieved by *deep-UV* or *e-beam* lithography;

- the thickness and the material of the waveguide has to be the same of the resonator;
- it is not easy to realize free-standing devices.

In our group, we recently developed an alternative coupling mechanism, where the bus waveguide is placed under the resonator [33]. The choice of a vertical coupling is favourable because, other than solving all the issues above mentioned, it has unique features. Figure 1.9 schematizes the key aspects of this technique, which in summary are:

- the precise control of the coupling gap is achieved by adjusting the deposition and etching rate of the *Borophosphosilicate Glass* (BPSG) spacing layer, so that it is compatible with conventional UV lithography (Figure 1.9(a));
- by varying the horizontal displacement of the waveguide it is possible to selectively couple a specific radial family of WGMs;
- the thickness of the resonator can be varied arbitrarily with respect to that of the waveguide;
- it is possible to realize free-standing devices;
- it is possible to couple wedge resonators (Figure 1.9(b)).

The key elements for the realization of a vertical coupling are the deposition, reflow and etching of a BPSG layer, which are necessary to planarize the spacing layer and remove the step created by the presence of the waveguide.

As mentioned, one of the unique features of the vertical coupling is the possible realization of the so called *wedge resonator*, monolithically coupled to an integrated waveguide [34]. These resonators are similar to the disk ones, but they differ in the inclination of the sidewalls. As a comparison, Figure 1.10 shows *Scanning Electron Microscope* (SEM) pictures of vertically coupled disk and wedge resonators. In particular, the realization of the wedge structure involves the pattern definition via a *Buffered HF oxide etch* (BHF). This step produces a much smoother surface finishing with respect to the corresponding *Reactive-Ion Etching* (RIE) used for the disk resonator definition. As

(a) (b)

Figure 1.9: (a) Scheme of the vertical coupling mechanism. The distance d_ν can be controlled with nanometric precision by controlling the deposition and etching rate of the BPSG layer. Thus, the coupling strength γ_ν does not depend on the photolithographic resolution. The horizontal displacement of the waveguide can be adjusted to selectively couple to a particular radial family of WGMs. (b) The vertical coupling mechanism is suitable for fabricating free-standing disk or wedge resonators. Figures reprinted from [34].

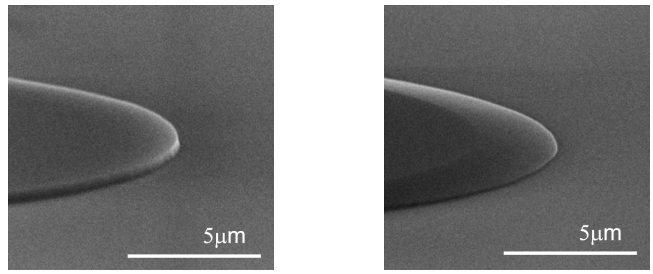

(a) (b)

Figure 1.10: SEM pictures of (a) disk and (b) wedge resonators, vertically coupled to an integrated bus waveguide (the waveguide is barely visible). Please note the difference in the sidewall angle and surface finishing. Figures reprinted from [34].

a result, wedge structures can show ultra-high quality factors, up to $Q \approx 1 \times 10^9$ [67].

From the perspective of a (bio-)sensor, a high quality factor is a desirable feature, as it could help in achieving a high spectral resolution and, in turn, a high sensing resolution. Thus, we decided to exploit the benefits of the wet etching and of the vertical coupling for the realization of an enhanced WGM sensor. In particular, we studied how the wedge inclination and thickness can affect the bulk

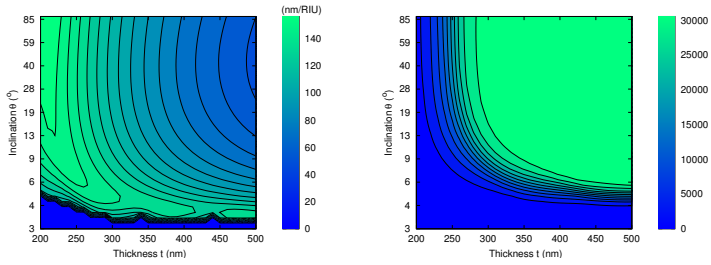

(a) (b)

FIGURE 1.11: (a) Bulk sensitivity S_b and (b) quality factor Q of a resonance of the first radial family of TE modes. More details in [76].

and surface sensitivity, and the quality factor [76].

By using the results of §1.2.2, we calculated the performances of a wedge resonator while varying its model parameters. As shown in Figure 1.11(a), the bulk sensitivity can be enhanced by either reducing the thickness or the sidewall inclination. In view of Equation (1.33), this result is reasonable, since in both cases the light confinement is reduced and, therefore, the interaction of the mode with the sensing liquid is increased. At the same time, however, Figure 1.11(b) shows that the quality factor is reduced.

As explained in §1.1.4, the parameter that is best suited to compare the sensing performances of a WGM resonator is the FOM. In particular, since our study was focused on surface sensing for label-free applications, we distinguished between the bulk and surface FOM with the definition of

$$\text{FOM}_b = \frac{QS_b}{\lambda} \tag{1.36}$$

$$\text{FOM}_s = \frac{QS_s}{\lambda} \tag{1.37}$$

where S_b and S_s were calculated through Equation (1.33) and Equation (1.35).

Figure 1.12 compares the calculated figures of merit (bulk and surface) for resonances of the first radial family, in both polarizations. Analyzing the results, we notice that the control of the thickness of the structures is crucial for achieving the highest FOM, both

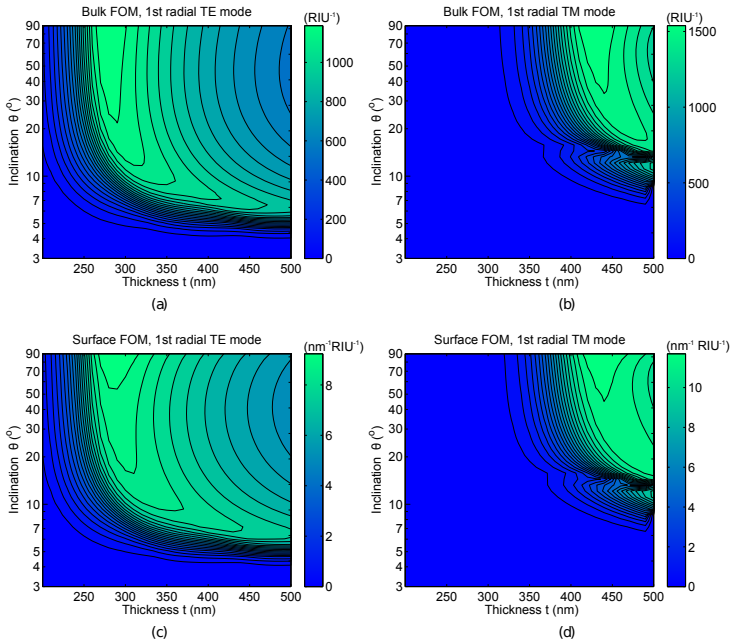

Figure 1.12: (a,b) Bulk FOM and (c,d) surface FOM, calculated for the first radial family of (a,c) TE and (b,d) TM modes. Figures reprinted from [76].

bulk and superficial. The control of the inclination is less critical for what concerns the FOM_b, while an almost vertical sidewall is required to optimize the FOM_s. The highest figures of merit are $\mathrm{FOM}_b \approx 1600/\mathrm{RIU}$ and $\mathrm{FOM}_s \approx 11.7/\mathrm{nm/RIU}$, both obtained in the case of TM polarization.

We should point out that it is not possible to create vertical sidewalls with a wet etching. However, wedge resonators with inclination $\theta \approx 30^\circ$ have already been reported [67] and we think that inclinations of at least $\theta \approx 40^\circ$ could be feasible. Thus, even if this analysis is purely theoretical, it still gives very useful guidelines to realize optimized wedge resonators, suggesting the use of the highest feasible inclination, and indicating the best thickness depending on θ. In this regard, the use of vertical coupling has emerged to be particularly appealing, because it gives control on the resonator thickness

and geometry without posing limitation to the bus waveguide.

1.3 Interferometers

In the previous sections, we showed how WGM resonators can be used to detect small changes of refractive index. In the mathematical analysis, and in particular in Equation (1.20), we saw that the resonance condition is given by the self-interference of the light in a closed loop. A change in the refractive index of the sensing liquid affects the effective index, n_{eff}, and this, in turns, affects the phase accumulated during a round-trip, shifting the resonance wavelength. Thus, the WGM resonator can be thought as a compact interferometer with high spectral resolution.

Obviously, other kind of interferometers can be used to detect the phase difference experienced by the light in contact with the sensing liquid. One of this is the MZI, schematically represented in Figure 1.13. In synthesis, the light coming from the input is split in two arms, with length L_A and L_B, respectively. The propagation constants of the light are $\beta_{A/B}$, which can be different if the effective refractive indexes $n_{eff,\,A/B}$ are different in the two arms.

The phase difference, accumulated by the light during the propagation in the two arms, is

$$\phi_{AB} = \phi_A - \phi_B = \beta_A L_A - \beta_B L_B = \frac{2\pi}{\lambda}(n_{eff,\,A} L_A - n_{eff,\,B} L_B) \tag{1.38}$$

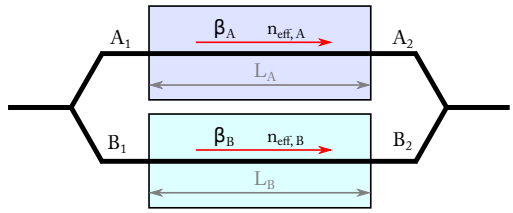

FIGURE 1.13: Schematic model of a Mach-Zehnder Interferometer. The field amplitudes in the two arms are labelled with A and B, respectively. The effective refractive indexes, $n_{eff,\,A/B}$, can be different in the two waveguides, leading to different propagation constants. The lengths of the arms are, respectively, L_A and L_B.

Neglecting the losses, at the recombiner the interference of the light leads to a transmission given by

$$T = \frac{1}{2}[1 + \cos(\phi_{AB})] \tag{1.39}$$

When the Mach-Zehnder is balanced, i.e., the optical path length of the two arms is almost equal ($n_{eff,\,A}L_A \approx n_{eff,\,B}L_B$), we have that ϕ_{AB} varies slowly with the wavelength, and the transmission spectrum at the output port is almost constant. Thus, the sensing signal can be obtained at fixed laser wavelength by monitoring the transmitted intensity. If the arm A is exposed to a sensing liquid and the arm B is protected by a cladding layer, the intensity at the output changes. The bulk sensitivity of this device can be calculated as

$$S_b = \frac{\partial T}{\partial n_A} = -\frac{\sin(\phi_{AB})}{2}\frac{\partial \phi_{AB}}{\partial n_A} = -\frac{\pi L_A \sin(\phi_{AB})}{\lambda}\frac{\partial n_{eff,\,A}}{\partial n_A} \tag{1.40}$$

The maximum sensitivity is obtained when $\phi_{AB} = (m + \frac{1}{2})\pi$ with m integer. The problem is that the sensitivity is not constant, and varies during the measurements (because ϕ_{AB} changes with n_A). In particular, small changes of refractive index are not resolved when $\phi_{AB} = m\pi$, limiting the overall resolution of the device.

1.3.1 Asymmetric Mach-Zehnder

The issue just described can be circumvented by spectral interrogation of an aMZI [79, 40]. As the name suggests, in this case the two arms are intentionally unbalanced, so that the transmission at the output port is wavelength-dependent. If the wavelength scan is performed in a small range ($\lambda = \lambda_0 + \delta\lambda$), we can write

$$\phi_{AB}(\lambda_0 + \delta\lambda) \approx \frac{2\pi}{\lambda_0}(n_{eff,\,A}L_A - n_{eff,\,B}L_B)(1 - \frac{\delta\lambda}{\lambda_0}) \tag{1.41}$$

$$= \phi_0 - \frac{2\pi\delta\lambda}{\lambda_0^2}(n_{eff,\,A}L_A - n_{eff,\,B}L_B) \tag{1.42}$$

By defining $\Lambda = \lambda_0^2/\left(n_{eff,\,A}L_A - n_{eff,\,B}L_B\right)$, we can write the transmission spectrum as

$$T(\lambda_0 + \delta\lambda) \approx \frac{1}{2}\left[1 + \cos\left(\phi_0 - \frac{2\pi\delta\lambda}{\Lambda}\right)\right] \tag{1.43}$$

from which we see that Λ plays the role of a FSR, and that its expression resembles Equation (1.21). Notice that Λ can be made arbitrarily short by increasing the optical path difference between the two arms. Reducing the FSR, the steepness of the curves of the transmission spectrum and the number of visible peaks (and valleys) in a given wavelength range increases. Therefore, Λ sets the intrinsic resolution for the measurement of the phase ϕ_0, similarly to the role of Q for a WGM sensor.

ϕ_0 can be measured accurately via a sinusoidal fit of the transmission spectrum, and from its variation we can detect variations in the refractive index n_A. We have

$$\phi_0 = \frac{2\pi}{\lambda_0}(n_{eff,\,A}L_A - n_{eff,\,B}L_B) \tag{1.44}$$

from which we can obtain

$$S_b = \frac{\partial\phi_0}{\partial n_A} = \frac{2\pi L_A}{\lambda_0}\frac{\partial n_{eff,\,A}}{\partial n_A} \tag{1.45}$$

Notice that this sensitivity is independent of ϕ_0, and that S_b can be increased by choosing a longer L_A.

In conclusion, in the design of an aMZI we have the freedom to independently set the sensitivity and resolution of the sensor. In particular, we saw that both parameters can be enhanced by increasing L_A. However, there is a catch: in this analysis we neglected the effects of losses. If the device is made too big, the absolute intensity and the visibility of the fringes at the output port will decrease, posing an ultimate limit to the achievable LOD.

1.3.2 Ring-loaded Mach-Zehnder

We conclude this theoretical section by proposing a device that could combine the compactness and sensitivity of a MRR with the wavelength independence of the balanced MZI. In particular, this idea came while trying to find a suitable method for the on-chip screening of a MRR sensor using broadband light (e.g., electroluminescence light emitted from silicon nanocrystals integrated in the waveguides [72, 80, 81]).

One possible way to achieve this is by cascading a MRR sensor with a MRR narrowband filter in add-drop configuration. If the filter

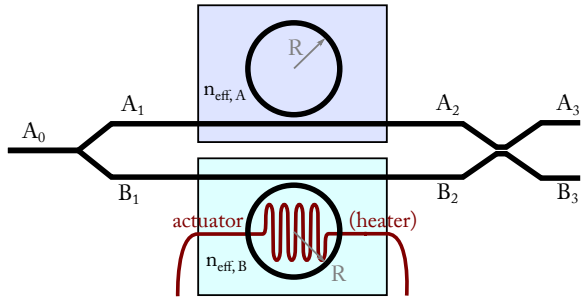

Figure 1.14: Scheme of a balanced ring-loaded Mach-Zehnder. The transmission at the output ports is balanced if $n_{eff,\,A} = n_{eff,\,B}$. The sensing arm A is affected by variations in refractive index n_A, while the reference arm B can be controlled with temperature, exploiting the thermo-optic coefficient.

is thermally actuated, its resonance wavelength can be tuned, providing a way to spectrally resolve the transmission spectrum of the sensor and, hence, to measure the resonance shift of the WGM sensor. One of the drawbacks of this configuration is that the transmitted power is inversely proportional to the spectral resolution of the filter, posing serious constraints to the light intensity of the source. The second limitation is that

- either the filter is continuously swept around the position of the resonance of the sensor, inducing thermal fluctuations in the nearby ambient,
- or it is slowly retro-actuated to remain on the rising slope of the resonance, in which case it will be affected by light intensity noise.

The proposed device is a ring-loaded (balanced) Mach-Zehnder. Figure 1.14 schematizes the concept. Basically, the central element is a balanced MZI, with a Y-splitter followed by a directional-coupler recombiner. The two arms are loaded with MRRs to enhance the phase sensitivity of the interferometer, without the need to increase their lengths.

The mathematical model is quite simple [82]. The Y-junction splits the light equally both in intensity and phase, such that $A_1 =$

$B_1 = \frac{A_0}{\sqrt{2}}$. During the propagation in the two arms, the light experience a phase shift βL which is equal for both, plus and additional phase delay $\phi_{A,\,B}$, which is given by the complex argument of Equation (1.15)

$$\begin{pmatrix} A_2 \\ B_2 \end{pmatrix} = \frac{A_0}{\sqrt{2}} \begin{pmatrix} e^{i\phi_A} \\ e^{i\phi_B} \end{pmatrix} \tag{1.46}$$

The phase delay can be simplified in [4, 60]

$$\phi_A = \pi + \theta_A + \tan^{-1}\left(\frac{t\sin(\theta_A)}{a - t\cos(\theta_A)}\right) + \tan^{-1}\left(\frac{ta\sin(\theta_A)}{1 - ta\cos(\theta_A)}\right) \tag{1.47}$$

where, θ_A, t and a are defined as in Equation (1.14). Notice that, when the resonator is critically coupled, the phase delay experiences an abrupt π shift at the resonant wavelength.

Finally, the recombiner mix the signals of the two arms adding a last $\frac{\pi}{2}$-shift, i.e.

$$\begin{pmatrix} A_3 \\ B_3 \end{pmatrix} = \frac{1}{\sqrt{2}} \begin{pmatrix} 1 & -i \\ -i & 1 \end{pmatrix} \begin{pmatrix} A_2 \\ B_2 \end{pmatrix} \tag{1.48}$$

from which we can calculate the total transmission coefficients

$$\begin{pmatrix} T_A \\ T_B \end{pmatrix} = \begin{pmatrix} \left|\frac{A_3}{A_0}\right|^2 \\ \left|\frac{B_3}{A_0}\right|^2 \end{pmatrix} = \frac{1}{2} \begin{pmatrix} 1 - \sin(\Delta\phi) \\ 1 + \sin(\Delta\phi) \end{pmatrix} \tag{1.49}$$

where we defined $\Delta\phi = \phi_A - \phi_B$.

If the two MRRs are balanced, i.e., have the same radius R and the same effective index n_{eff}, it is easy to see that $T_A = T_B$ for every wavelength. However, as soon as a small variation in effective index $\Delta n = n_{eff,\,A} - n_{eff,\,B}$ is introduced, the transmission spectra of the two output ports present sharp double Fano-like features. Figure 1.15 shows the differential transmission $T_B - T_A$ in a broad wavelength range of 20 nm (comparable to that of a LED source) for three different values of Δn.

If a broadband light is used, the signals at the output photodiodes will be given by the (normalized) integrals of the transmission spectra. Figure 1.16 shows the expected differential output $T_B - T_A$ when the device is lit with broadband light. We see that the signal presents a steep response for small variations $\Delta n \approx 0$, paving the way

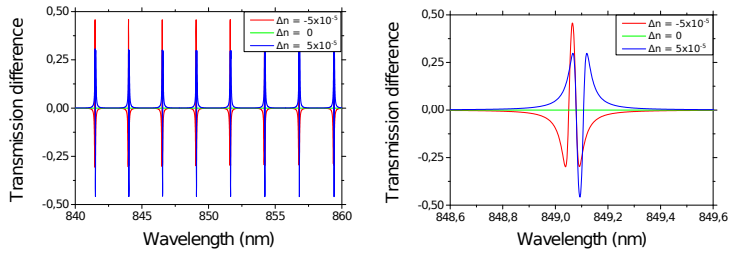

Figure 1.15: (a) Broadband and (b) narrowband spectra of the differential transmission $T_B - T_A$ of a balanced ring-loaded Mach-Zehnder, for $\Delta n = -5 \times 10^{-5}$, 0 and 5×10^{-5} RIU.

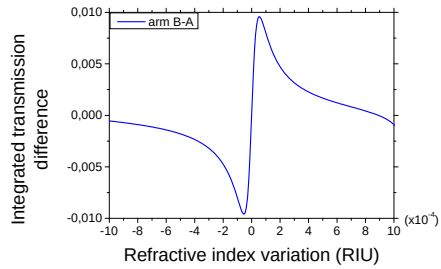

Figure 1.16: Integrated differential transmission, as a function of the index variation $\Delta n = n_{eff,A} - n_{eff,B}$. The sensitivity is maximum when $\Delta n \approx 0$.

for a highly-sensitive refractometer. Even more notably, the differential output can be used as feedback for a thermal actuator on the reference MRR B. By analyzing Figure 1.16, we see that the feedback control is stable for $\Delta n = \pm 10^{-3}$ RIU, automatically bringing the system towards equilibrium at $\Delta n \approx 0$. In this case, the variation in refractive index n_A can be directly measured by monitoring the temperature in B or, equivalently, the feedback current.

In conclusion, the proposed device shows several favourable features:

- it is compact,
- it is insensitive to light intensity fluctuations,

- it is highly sensitive to refractive index variations,
- it is stable in a wide range of unbalanced Δn,
- it does not require tunable narrowband light sources,
- the thermal actuator is tuned only to keep the system balanced, without the need of continuous thermal sweeps.

In view of all these pros, we think that it could be really interesting to develop the proposed architecture, for the realization of an all-integrated label-free sensor.

Experimental apparatus 2

The development of a reliable biosensor, able to resolve the binding of small fractions of a monolayer of proteins or other small biomolecules, requires the mastering of many experimental, critical, issues. The ultimate limit of detection, in fact, is not only affected by the optical characteristics of the WGM resonator or of the MZI, but also by other external factors. Among them, we remind here:

- Fluctuations in intensity, polarization and wavelength of the laser source.
- Mechanical stability of the light coupling system.
- Temperature stability of the sensor, particularly during the injection of the solution to be sensed.
- Reproducibility of the flow-rate and sample volume.
- Electrical noise in the readout system.
- Reproducible and efficient coverage of the sensor with the specific receptors (e.g., DNA-aptamers or antibodies).

With the exception of the last item, all the other issues have been faced during the development of the experimental setup. In fact, the development and the perfecting of the apparatus required a consistent

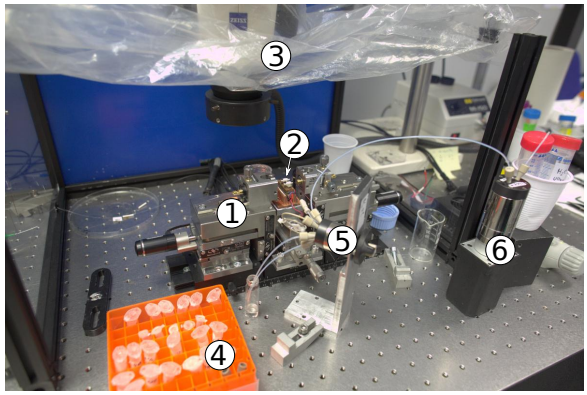

Figure 2.1: Photograph of the experimental setup. In the photo we can recognize: (1) the translation stages for the precise alignment of the optical fibers, (2) the thermally-controlled sample holder, (3) the optical microscope, (4) few sample vials, (5) the injection valve and (6) the continuous flow pump. The core part of the setup is entirely encased, with the aim of reducing air flows and thermal fluctuations.

amount of efforts of my Ph.D. work. The photograph in Figure 2.1 shows the core of the apparatus, where the optical and fluidic systems converge. The description, characterization and performances of the experimental apparatus will be detailed in this chapter. We distinguish between optical setup and liquid handling, addressing the former in §2.1 and the latter in §2.2.

The issue concerning the optimization of the functionalization process has been addressed by Laura Pasquardini (a colleague of the FBK) and by Marta Guarisco (former master student of the UniTN) in [83]. A short description of the proposed functionalization procedure is reported in §A

2.1 Optical setups

2.1.1 Chip in/out coupling with fibers

The common elements of all the optical setups described in this thesis are the chip holder and the fiber positioners. The photograph reported in Figure 2.2, resembles many other setups for waveguide

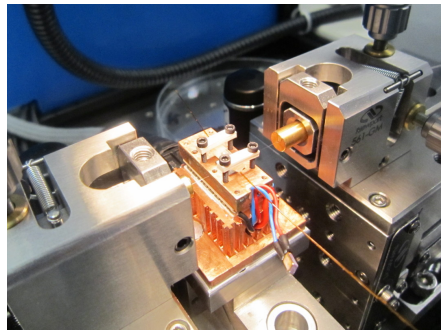

FIGURE 2.2: Zoomed view on the optical fibers positioners and on the thermally-controlled sample holder. The precise alignment of the fibers, with sub-micrometric resolution, is needed to achieve efficient coupling of the light in (and out) the photonic chip. The sample holder shows auxiliary threaded holes and screws, which are used to fasten the microfluidic flowcell on the photonic chip.

probing: two tapered lensed optical fibers, *OZ-Optics TSMJ* series, are mounted on two XYZ-translastion stages, *Newport Ultralign 562* series, and positioned with sub-micrometric precision with six remotely controlled actuators, *Newport NanoPZ PZA12*. The use of tapered lensed fibers is highly recommended, as it reduces the insertion losses to the photonic chip, by improving the matching of the mode field diameter. The use of the remotely controlled actuators is not compulsory, but desirable. It permits the encasing of the experimental setup, eliminating the need for manual access, and leading to a better thermalization of the ambient near the sensor.

The photonic chip is placed on a flat holder, made with a block of copper, whose temperature can be regulated with a Peltier thermoelectric cell. The position of this holder can be translated longitudinally and vertically with micrometric screws, *Newport Ultralign 561D*. To visualize the sample and the positioning of the fibers, an optical microscope is placed above the holder. The copper block has threaded holes, which are used to fasten the microfluidic flowcell to the photonic chip with small screws.

The temperature controller, shown in Figure 2.3(a), is homemade. Its main processing unit is a *RMT Ltd. DX5100*. It can be directly controlled with a PC or programmed for autonomous routine

(a)

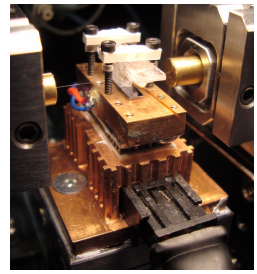

(b)

Figure 2.3: (a) Dual channel thermal controller, home-built on the base of the *RMT Ltd. DX5100* programmable controller unit. (b) Zoomed view on the sample holder. The Peltier thermo-electric cooler is interposed between a copper heat sink and the sample holder. The copper ensures a fast thermalization and homogeneity in the temperature distribution. The temperature of the block is measured with an *Analog Digital AD590*, directly inside the copper, just below the photonic chip.

functioning. It can regulate two independent channels, providing up to 2×16 W of power to the Peltier cells. The resolution of the temperature reading is influenced by the choice of the temperature sensor. In our case we choose two *Analog Digital AD590JF*, because of the small dimensions (only $2.2 \times 5.8 \times 1.2$ mm) and of the linearity of the response. Considering the resolution of the analog-to-digital converter in the controller unit, the precision in the temperature reading is 0.6 mK.

The feedback loop of the controller is closed on a thermoelectric Peltier cell, interposed between the copper sample-holder and a copper heat-sink. Figure 2.3(b) shows a close-up picture of the assembly. The temperature sensor is encapsulated into the top copper block, directly below the usual position of the sensor chip.

To characterize the temperature controller, we measured its accuracy, the stability and the response time of the feedback-loop. In addition, we also assessed the response time of the transmission spectra of a WGM resonator, as a function of the temperature variations of the sample holder. Figure 2.4(a) shows the accuracy of the temperature readings on the first channel of the controller, compared to the

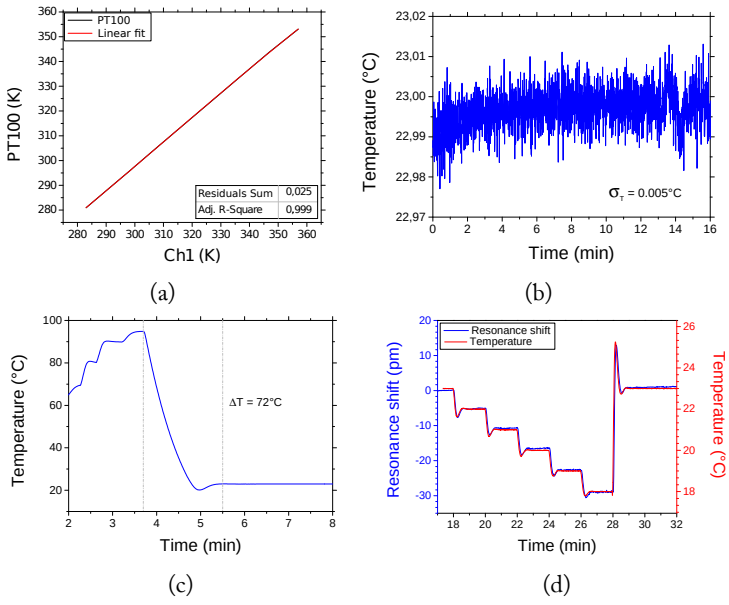

FIGURE 2.4: Calibration and characterization measurements performed on the thermal controller. (a) Comparison of the temperature read from the *AD590* sensor of the channel Ch1, with the temperature of a reference PT100 thermoresistor. (b) Trace of the temperature, measured in the copper block of the sample holder, in a time window of 16 min, during active control. The temperature is stabilized within ± 5 mK. (c) Example of a programmed temperature cycle. The controller recovered a temperature excursion of $\Delta T = 72\,^{\circ}\mathrm{C}$ in less than 2 min. (d) Comparison of the resonance shift curve of a wedge resonator and of the temperature curve, during a programmed temperature cycle. Thanks to the high thermal conductivity of the copper and of the small thermal capacity of the photonic sample, the two curves are highly correlated, with a short temporal delay, of the order of ≈ 3 s, in-between the two.

reading of a reference PT100 resistance temperature detector. After the calibration, the accuracy of both channels is within $\pm 0.05\,^{\circ}\mathrm{C}$ for temperatures below $50\,^{\circ}\mathrm{C}$, and within $\pm 0.15\,^{\circ}\mathrm{C}$ for temperatures up to $100\,^{\circ}\mathrm{C}$.

The stability of the temperature control-loop has been characterized by measuring the temperature in the sample-holder copper block, in a time window of 16 min. During the measurement, no liquids were flown on the sensor, and the casing of the setup has been kept closed to reduce air fluctuations. Figure 2.4(b) shows that the temperature stability (measured as the standard deviation of the whole dataset) is 5 mK.

The control-loop is based on the well-known proportional-integral-derivative (PID) algorithm. The total response time of the controller depends on the cooling/heating power of the thermoelectric cell (the actuator), the system heat capacity, and on the three coefficients of the PID algorithm. We fine-tuned these coefficients, both with the Ziegler–Nichols method and empirically, to reduce the response time to temperature setpoint variations. As shown in Figure 2.4(c), a programmed variation $\Delta T = 72\,^{\circ}\mathrm{C}$ can be stabilized in less than 2 min, with a small overshoot of the setpoint. This feature is believed to be very useful if the regeneration of the aptamer-functionalized biosensor is obtained with thermal shocks. In this case, in fact, temperatures of up to $90\sim95\,^{\circ}\mathrm{C}$ have to be set to reversibly denaturate the biorecognition molecules. However, in this thesis, alternative methods (and, in particular, denaturation through pH variations) have been preferred. The reason for this choice is that, at high temperature, we did not succeed to keep the surface of the sensor wet, and, as better explained in §2.2.1, the drying of the sensor surface affects the reliability of the WGM resonance wavelength measurement.

Finally, we characterized the time response of the effects of the temperature on a WGM resonator. To this regard, we measured the wavelength of a high-Q resonance in a wedge microresonator, and we compared it to the temperature read from the *AD590* sensor. For this experiment, the wedge radius was 25 µm, and its core material was non-stoichiometric silicon nitride, SiN_x. The probing laser wavelength was swept around 780 nm, with the use of the optical setup described in §2.1.3.2. As reported in Figure 2.4(d), the resonance wavelength shifts according to the variations in the temperature, following the temperature readings of the controller with a delay of the order of ≈ 3 s. Thus, from this measurement, we conclude that the

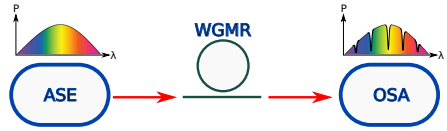

FIGURE 2.5: Schematic representation of the experimental setup for the broadband characterization of the photonic structures, in the NIR wavelength range. An ASE source emits broadband, incoherent and unpolarized, light, in the range from 1530 to 1570 nm. The light is transmitted through the WGM resonator sensor and analyzed at the output with an OSA. The transmission spectrum is retrieved in a single acquisition.

control of the temperature of the holder is sufficient to affect and control the temperature in the resonator, and that the sensitivity of the wedge to temperature variation is 5.9(1) pm/K. During active temperature stabilization, the temperature fluctuations will lead to wavelength fluctuations of the order of 0.03 pm.

2.1.2 Broadband NIR source

During my Ph.D. research, I have developed a number of optical setups, each suitable for a particular application or spectral region. For a fast characterization of the transmission spectra of moderate-Q WGM resonators, we decided to probe the photonic devices with broadband light. In particular, we opted for an *Amplified Spontaneous Emission* (ASE) source, *Opto-Link OLS15CLGB-25-FA*.

The scheme of the setup is reported in Figure 2.5. The light of the source is unpolarized and incoherent, with emission wavelength from about 1530 to 1600 nm. After the transmission through the resonator, the signal is collected by the output optical fiber, and it is analyzed in an *Anritsu MS9710C Optical Spectrum Analyzer* (OSA). The entire transmission spectrum is retrieved in about a second, with a resolution of 20 pm.

Figure 2.6 shows the light intensity transmitted through a vertically-coupled SiN_x microdisk resonator of 25 µm radius. For moderate-Q resonators, like this one, the resolution of the OSA is sufficient. Moreover, as shown in Figure 2.6(b), by increasing the sampling points it is possible to increase the effective resolution of the con-

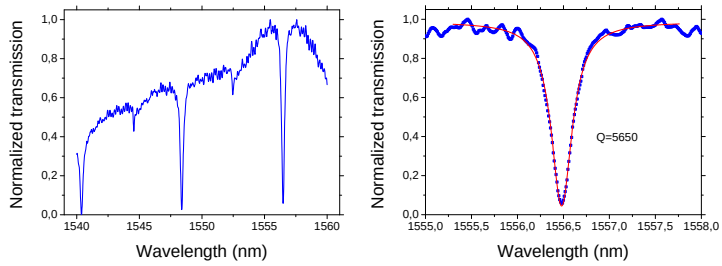

(a) (b)

Figure 2.6: (a) Transmission spectrum (normalized to the maximum intensity) of a microdisk resonator, measured with the scheme explained in Figure 2.5. (b) Zoomed view on a resonance of the microdisk. The resolution of the OSA, which is 20 pm, is not suitable to resolve small resonance shifts or resonances with quality factors $Q \gtrapprox 2 \times 10^4$.

volved spectrum, leading to a more accurate fitting of the resonances.

The optical setup here explained is well suited to characterize the bulk sensing properties of WGM resonators with moderate quality factors. Figure 2.7 reports the characterization and comparison of a disk and a wedge resonators, both realized in SiN_x (refractive index 1.99). The two geometries have the same radius (25 µm) and thickness (350 nm), but the different etching processes for their definition creates different sidewall angles. The disk, defined with a RIE process, shows a sidewall inclination of 85°, while the angle of the wedge, created with a BHF process, is $\approx 7°$.

To measure the bulk sensitivity, we exposed the surface of the two resonators to several glucose/water solutions, with concentrations spanning from 0.0 to 9.0 % (weight/weight). The change in refractive index of the solutions, Δn, is proportional to the glucose concentration C through the relation

$$\Delta n = C \times 1.375 \times 10^{-3} \text{ RIU /\%} \tag{2.1}$$

as reported in [84] and confirmed by control measurements, performed with an Abbe refractometer in our labs.

Figure 2.7(a) shows the measured resonance spectral positions as a function of the refractive indexes of the solutions. To enhance the

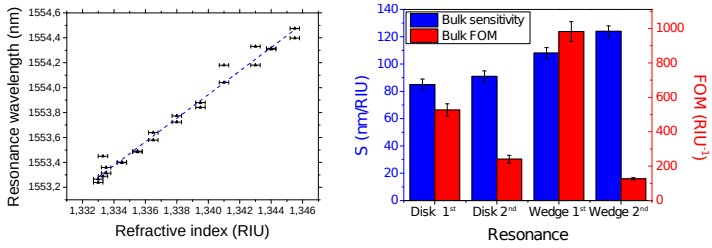

(a) (b)

FIGURE 2.7: Sensing characterization of a disk and a wedge resonator with similar composition and size. The measurements have been achieved with the setup in Figure 2.5. (a) The resonance position is measured as a function of the refractive index of the liquid in contact with the sensor. The bulk sensitivity is calculated from the slope of the linear fit. (b) Plot summarizing the sensing characteristics of the two microresonators, for both resonances of the first and second radial families of WGMs. These results have motivated the study of §1.2.3. The comparison between the theoretical analysis and the experimental results is treated in [76].

precision of the resonance wavelength determination, we fitted a portion of every spectrum with a lorentzian function

$$f(\lambda) = I_0 \left(1 - \frac{A\gamma^2}{\gamma^2 + (\lambda - \lambda_0)^2}\right) \tag{2.2}$$

where I_0 is the off-resonance transmitted intensity, A is the amplitude of the resonance (i.e., one minus the transmission coefficient at resonance, Equation (1.22)), γ is the half-width at half-maximum (half-amplitude, in this case) and λ_0 is the resonance center wavelength.

By using Equation (1.9), we calculated the bulk sensitivity as the slope of the plot. In Figure 2.7(b) we compared the bulk sensitivity and the FOM, Equation (1.13), of the two microresonators, for both resonances of the first and second radial families of WGMs. We notice that, compared to the commonly-used first radial resonance of the disk resonator ($S_b = 85(4)$ nm/RIU), the bulk sensitivity is enhanced by either using the second radial family ($S_b = 91(4)$ nm/RIU) or reducing the inclination of the resonator sidewalls

($S_b = 108(4)$ nm/RIU). The explanation is that both choices have the effect of reducing the confinement of the WGM and, therefore, of increasing the interaction of the mode with the sensing liquid. However, the WGMs of the second radial family exhibit lower quality factors, due to radiative losses. For these reasons, the highest bulk FOM is achieved by the wedge resonator's first radial WGM family. Compared to the disk geometry, which exhibits a $\mathrm{FOM_{disk}} = 530(40)$ /RIU, the wedge microresonator performs almost twice better, with a $\mathrm{FOM_{wedge}} = 980(60)$ /RIU. These results have motivated the study of §1.2.3. A deeper analysis of the two structures, and a comparison of the experimental results with the simulated ones, is treated in [76].

In conclusion, the setup for broadband probing here presented shows several favourable features, first of which is its simplicity. However, this setup can not resolve narrow resonances, with Q values exceeding $\approx 2 \times 10^4$. Moreover, even with an increased convolved resolution, the ultimate limit is given by the wavelength stability, which is reported in the manual of the OSA as 5 pm. Thus, resonance shifts smaller than this value can not be reliably detected. The next sections will present three optical setups that have been developed to overcome these two issues.

2.1.3 Monochromaric NIR sources

2.1.3.1 Tunable external cavity diode laser at 1.5 μm

To characterize narrow resonances at high resolution, we used a tunable external cavity diode laser, with emission wavelength ranging from 1520 to 1630 nm. The laser is a *Yenista Tunics T100S*, operated in continuous sweep mode. As schematized in Figure 2.8, its polarization is controlled with two quarter-waveplates and one half-waveplate. The light is fed into (and out from) the waveguides of the chip, by means of tapered optical fibers, and it is finally measured with a photodetector.

In principle, it would be possible to reconstruct the transmission spectrum by setting, one after the other, closely spaced wavelengths on the laser controller, and measuring in sequence the transmitted intensities. However, this procedure is too slow for practical uses in biosensing experiments, because a complete scan can take definitely more than 1 min, depending on the scan range and the resolution. To overcome this problem, it is possible to operate in continuous-

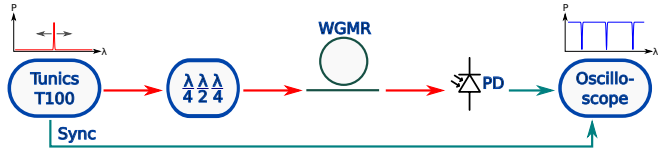

FIGURE 2.8: Schematic of the experimental setup for the high resolution characterization of the samples in the NIR. An external-cavity tunable diode laser, a *Yenista Tunics T100S*, is continuously swept in a given range. The light polarization is adjusted with two quarter-waveplates and one half-waveplate. The light is measured at the output of the WGM microresonator with a photodetector. The transmission spectrum is reconstructed by synchronizing, with an oscilloscope *Pico Technology PicoScope 4424*, the traces of the photodetector and of the sync signal of the laser controller.

sweep mode, where the laser cycles in a range between two given wavelengths and at a fixed sweep speed, v. At the beginning of every sweep, a rising-edge trigger is set on the *sync* output of the laser. This signal can be used to trigger an oscilloscope (in our case a *Pico Technology PicoScope 4424*), which will read the photodetector synchronously. In this case, the measured intensity traces $I(t)$, which are time-dependent, can be converted to wavelength-dependent transmission spectra, $I(\lambda)$, with the simple mapping

$$\lambda = \lambda_0 + (t - t_0)v \tag{2.3}$$

where λ_0 is the sweep starting wavelength and t_0 is the time of the trigger event.

In continuous-sweep mode, the time required for a complete scan is proportional to the scan range and inversely proportional to v, so that a higher speed would be desirable. At the same time, however, the resolution of the spectrum is inversely proportional to the sweep speed, v, and it is lower limited by the slowest between the photodetector bandwidth and the oscilloscope sampling rate. As an example, Figure 2.9(a) shows the reconstructed transmitted intensity spectrum of the same wedge resonator analyzed also in Figure 2.7(b) (radius 25 µm, thickness 350 nm and core material SiN_x). Here the scan range is 24 nm (more than twice the FSR) and the sweep speed is $v = 10\,\mathrm{nm\,s^{-1}}$, leading to a reasonable scan period of $T = 2.4\,\mathrm{s}$. By setting a sampling frequency $\nu = 10\,\mathrm{kHz}$ (10^4 samples per second),

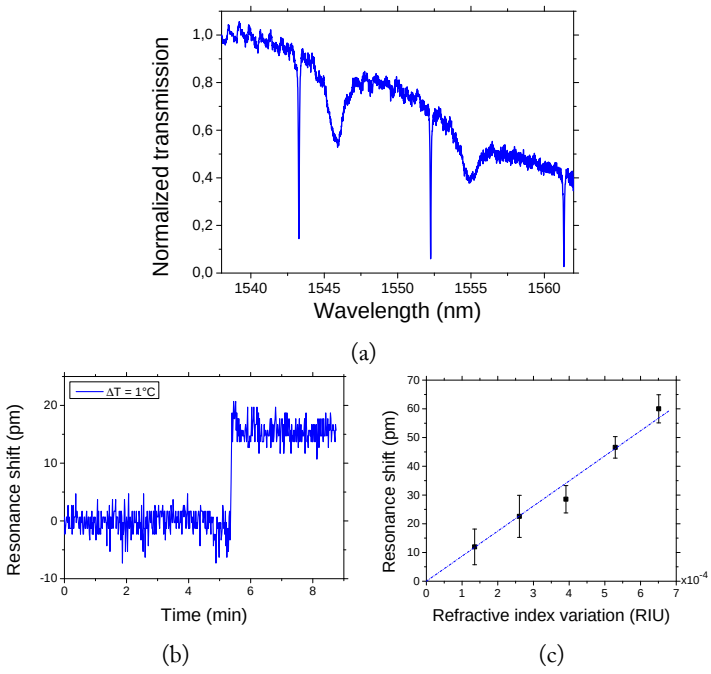

Figure 2.9: (a) Transmitted intensity spectrum (normalized to the maximum intensity) of a wedge resonator, measured with the setup in Figure 2.8. Two families of radial WGMs are visible, and can be distinguished for their quality factor. (b) Measurement of the temperature sensitivity of the same wedge resonator. The resonance shifts by 15(3) pm for a temperature variation of 1 °C. (c) Refractive index sensitivity of the same wedge resonator, for bulk variations of refractive index ($S_b = 88(3)$ nm/RIU).

which is lower than the bandwidth of the photodetector (100 kHz), the resulting spectral sampling spacing is 1 pm. At this sweep speed, the photodetector-limited resolution would be 0.1 pm, which enables the resolving of resonances with quality factors up to $Q \approx 3 \times 10^6$.

Figure 2.9(b) and (c) report the measurements of the temperature sensitivity and bulk refractive index sensitivity for the same wedge resonator as in Figure 2.9(a). Also in this case, for every spectrum acquisition, we automatically selected a small wavlength range around

the target resonance, and we fitted the resonance in real-time with a lorentzian function, Equation (2.2). With this method, we measured a temperature sensitivity $S_T = 15(3)$ pm/K, and a bulk refractive index sensitivity $S_b = 88(3)$ nm/RIU.

As we can notice from the distribution of the datapoints in Figure 2.9(b), or from the error bars in Figure 2.9(c), the resonance shifts can not be measured with the same very high, single-shot, resolution derived above. The accurate detection of small resonance shifts is still limited by the repeatibility of the scan. The shift, in fact, has to be measured as the difference between two spectra, and this difference is not limited (only) by the resolution of the two, single, scans. The determination of the resonance position, in fact, is affected by a precision (relative uncertainty) in the order of 3 pm. The reason for this uncertainty is that the wavelength tuning of the *Tunics T100S* source is obtained by changing the length of the laser cavity, and that this operation is actuated with a motor. While the motor speed, and consequently the sweep speed, can be accurately controlled, the absolute length of the cavity has to be referenced (internally, in the source). This internal reference has an absolute accuracy of 30 pm, and a repeated precision of 3 pm (the datasheet of the source states a slightly more conservative value, 5 pm). This finite precision sets the lower limit for the resolution of small resonance shifts, and, hence, also sets the lower limit of detection of the sensor.

A way to overcome the issue of the wavelength precision, is the use of a more reproducible wavelength tuning method. The next two sections deal with two alternatives to improve by more than one order of magnitude the limit of detection of our apparatus: the wavelength tuning with a piezoelectric-actuated cavity and the tuning by modulation of the driving current of a *Vertical-Cavity Surface-Emitting Laser* (VCSEL).

2.1.3.2 External cavity tunable diode laser at 780 nm

It is well known that silicon photonics is pushing the frontiers of telecommunications, allowing the realization of cheap, compact and efficient photonic routers and modulators, entirely based on CMOS fabrication, and operating at wavelengths near 1.55 μm. However, this wonderful technology platform is still lacking an efficient light source and a photodetector, to be integrated directly on-chip. Despite the hybrid-integration with external laser sources and detectors,

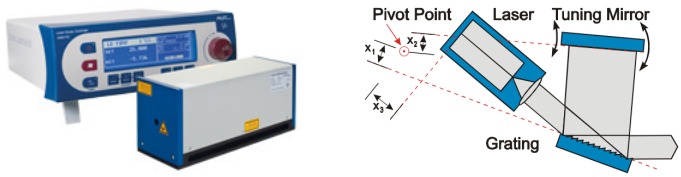

(a) (b)

Figure 2.10: (a) Picture of a *Sacher Lasertechnik LiON TEC-500* laser. (b) Scheme of the Littman/Metcalf configuration for the realization of a tunable external cavity diode laser.

one of the proposed way to realize a complete set of photonic devices is the use of shorter wavelengths, in the VIS-NIR range. In this way, the light detection can be achieved with silicon detectors, while the light emission can be obtained, for example, with silicon nanocrystals [85, 86]. Obviously, the waveguides can not be made of silicon, because it is not transparent in this range, but many other CMOS-compatible silicon-based materials are available, like silicon nitride, Si_3N_4, or silicon oxynitride, SiO_xN_y.

The Nanoscience Laboratory of the University of Trento has always been committed to the development of such a complete integrated platform [87]. Also in the field of biosensors, we decided to investigate the possibilities of working in the VIS-NIR range. For this reason, we appositely built an optical setup with a tunable laser source at wavelengths near 780 nm. The laser is a *Sacher Lasertechnik LiON TEC-500*, shown in Figure 2.10(a). The topology of the resonant cavity has been developed by Littman and Metcalf. In particular, if the rotation pivot point of the tuning mirror (see Figure 2.10(b)) is carefully chosen, the tuning of the emission wavelength can be made mode-hop-free in a large range [88]. In the *Sacher LiON* laser, the tuning mirror is actuated with both a motor, for large tuning ranges, and a piezoelectric element, for the fine tuning in a small range. Thus, while developing this apparatus, we had the chance to test the reliability of the cavity tuning with a piezoelectric actuator.

The scheme of the optical setup is represented in Figure 2.11. Similarly to the previous setup, the light from the laser is continuously swept in a given range, and the polarization is controlled with three waveplates. At the output of the chip, the light is collected with

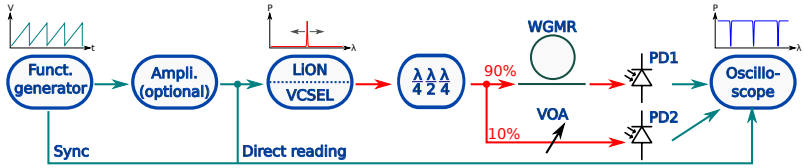

FIGURE 2.11: Schematic of the experimental setup for the characterization of sensors in the VIS-NIR range. The basic idea is similar to the one of Figure 2.8, but it differs in the source of the modulation, which in this case is an external function generator, and in the mechanism that actuates the wavelength tuning. The amplifier is needed to drive at high voltages the piezoelectric actuator of the *Sacher Lasertechnik LiON*, but it can be avoided for small scan ranges. The light polarization is controlled with waveplates. Then, a 90/10 fiber splitter divides the light: one part is sent to the WGM resonator and to the first photodetector; the other is sent, through a variable optical attenuator, to a reference photodetector. As in Figure 2.8, the transmission spectrum is reconstructed, at the oscilloscope, by synchronizing the power ratio of the two photodetectors with the modulation signal that drives the laser cavity actuator.

a photodetector and then read, synchronously to the modulation signal, with an oscilloscope. The differences with the previous setup are that:

- the modulation of the wavelength is applied to the piezoelectric actuator with an external function generator, amplified up to 100 V with a power amplifier, *N4L LPA400*;
- after the waveplates, the light is split in two branches, with either 50/50 or 90/10 splitting ratios. One part is sent to the WGM resonator, the other part is sent to a variable optical attenuator and then to a reference photodetector.

The reason for the necessity of the two photodetectors is that the output power of the *LiON* laser is strongly wavelength-dependent. Comparing a spectrum obtained with the *Tunics* source, Figure 2.9(a), with the one in Figure 2.12(a), we can notice that the baseline is really noisy, such to reduce almost entirely the visibility of the WGM resonances. In contrast, Figure 2.12(b) shows a transmission spectrum of

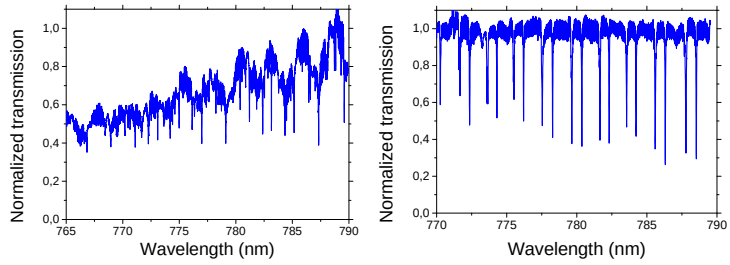

Figure 2.12: Transmission spectra of two similar wedge microresonators, acquired in a broad range with a *Sacher Lasertechnik LiON TEC-500*, (a) without and (b) with the referencing photodetector. In the latter case, the contrast for the identification of the resonance peaks is visibly enhanced.

a similar wedge resonator, where the normalization is provided by the power impinging on the reference photodetector. The resulting plot is much more clean, and the visibility of the resonances is enhanced.

The two photodetectors for this apparatus have been home-made, and are based on a fast silicon photodiode, *Hamamatsu S5972*, and a low-noise, low-distorsion operational amplifier with gain-bandwidth product of 3 MHz. The schematic of the transimpedance amplifier circuit is shown in Figure 2.13(a), while the photograph in Figure 2.13(b) depicts the final casing of the photodetector. The circuit is designed to be battery-powered, in order to reduce the electric noise, and to have a fixed current-to-voltage gain (transimpedance) of 10 kΩ. The capacitance in parallel to the feedback resistance is calculated to avoid self oscillations at high frequency, as suggested in [89]. The calculated 3 dB-bandwidth should be as high as ∼900 kHz, according to the impedance of the feedback loop.

Figure 2.13(c) and (d) report the characterizations of the responsivity and of the temporal response of the two detectors. The first shows that the devices have good linearity in the whole operating-range. The responsivity is calculated as $R = 5.0(1) \times 10^3$ V/W, which fits reasonably good with the usual responsivity of silicon photodiodes and the chosen transimpedance gain. The second measurement has been achieved by acquiring, at high sampling rate, the output of the photodetector, when illuminated by ultra-short pulses of

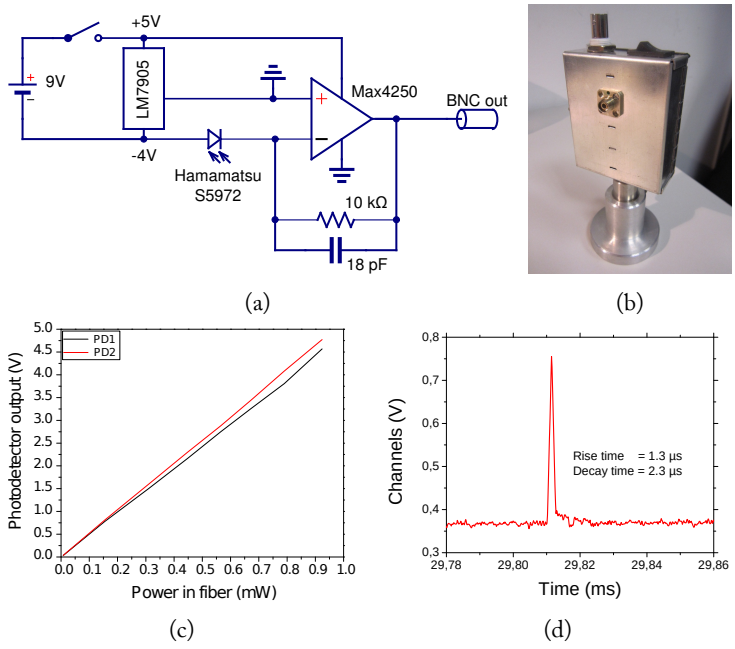

FIGURE 2.13: (a) Circuit schematic of the photodetector. The photodiode is a *Hamamatsu S5972*, and the op-amp is a *Maxim MAX4250*. The voltage/current gain of the transimpedance amplifier is fixed to 10 kΩ. The calculated 3 dB-bandwidth is ∼900 kHz. (b) Picture of one home-made photodetector. (c) Power calibration curves for the two realized photodetector replicas. The devices show good linearity in the whole operating-range of the op-amp. (d) Temporal response of one of the photodetectors when illuminated by an ultrashort pulse of a picosecond-pulsed-laser. The bandwidth is greater than 200 kHz.

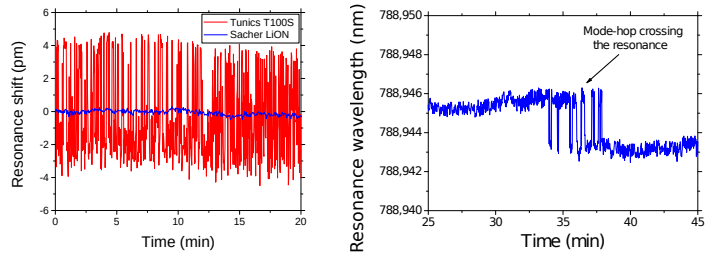

(a) (b)

Figure 2.14: (a) Comparison of the resonance shift signals recorded with a *Tunics T100S* (setup in Figure 2.8) and with a *Sacher LiON* (setup in Figure 2.11) tunable lasers. The WGM sensor under investigation is a wedge microresonator, kept in air at constant temperature. Analysing the signals in a time window of 5 min, the standard deviation of the measurements obtained with the *Tunics* source is 3 pm, whereas the standard deviation with the *LiON* source is only 0.1 pm, corresponding to a 30-fold enhancement. (b) Effect on the resonance wavelength estimation when a mode-hop is spectrally positioned within the resonance width. The magnitude of the mode-hop-induced shift is 3 pm.

a picosecond-pulsed-laser. The rise and decay times are in the order of 1∼2 µs, which indicates a bandwidth $\gtrsim$200 kHz. The circuit has been soldered on a prototyping perforated board, instead of a professional *Printed Circuit Board* (PCB). Therefore, the stray capacitances could explain why the measured bandwidth is lower than the calculated one. However, during the experiments of this thesis, the reduced bandwidth has never been the limiting factor to the resolution of the specta, and for this reason we did not optimize the detector any further.

As previously anticipated, the use of a piezoelectric actuator improved the scan precision, in comparison to the actuation with a motor, as in the case of the *Tunics* laser. Figure 2.14(a) shows a comparison of the repeated measurement of the resonance wavelength, obtained with the setups of Figure 2.8 and Figure 2.11. In this case the device under test is the usual SiN_x wedge resonator, with 25 µm radius and 350 nm thickness, dried and exposed to air, and kept at constant temperature. As we can see, the two traces show very dif-

ferent resonance wavelength uncertainties. By analyzing the standard deviation of the signals in a time window of 5 min, the motor actuation leads to an uncertainty of 3 pm, while the piezoelectric actuation can reach values as low as 0.1 pm, corresponding to a 30-fold enhancement.

However, even this setup has some problems. First, the fine scan range is quite limited: the piezoelectric actuator can be driven up to 100 V, but the tuning sensitivity is only $4\,\mathrm{pm\,V^{-1}}$, leading to a total scan range of 0.4 nm. For resonators of small radii, this range is less than the FSR, and it is possible that no resonance is detected. Luckily, in such cases, it is possible to move the center of the fine scan window with the motor actuator, until one resonance becomes visible. The second issue is the need of the two photodetectors, that inevitably reduces the light power made available to probe the WGM resonator. When the insertion losses of the photonic chip are high, this can be a problem. The third issue, and probably the more serious, is that the *LiON* laser shows many mode-hops. Despite the specification of the constructor and the particular precautions in the design of the cavity, Figure 2.10(a), we observed an unpredictable number, from 5 to 20 or more, of mode-hops in the 0.4 nm range of the fine scan. With resonances of $\approx$ 50 pm width, it is quite probable that, sooner or later, the resonance will cross the spectral position of one of these mode-hops. Figure 2.14(b) shows the apparent hops in resonance position when this happens. The effective shift, caused by the mode-hops, is in the order of 3 pm. Being an apparent shift, and, in addition, a quite visible artefact, it should be possible to correct the data in post-processing. However, for a better reliability of the resonance shift measurement, any mode-hop should be avoided from the beginning.

We conclude this section by showing the result of the measurement of the bulk sensitivity of a wedge resonator, with the setup here proposed. Figure 2.15(a) reports the resonance shift curves, obtained by exposing the sensor to several water-glucose solutions, with concentrations ranging from 0.1 to 0.5 % (weight over weight). The SNR is high, even at the lowest refractive index variation ($\Delta n = 1.4 \times 10^{-4}$ RIU). The higher precision of this setup is particularly evident by comparing the error bars in the plot of Figure 2.15(b) with the ones in Figure 2.9(c). Thanks to the improvements here intro-

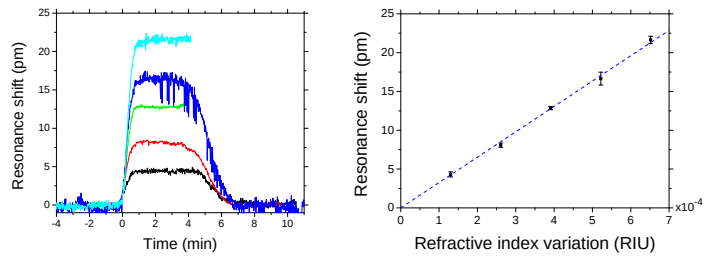

(a) (b)

Figure 2.15: The higher spectral resolution obtained with the experimental apparatus in Figure 2.11, leads to a more precise estimation of the bulk sensitivity. (a) Sensorgrams obtained by injecting several glucose solutions at different concentrations on a wedge resonator. (b) Resonance shift as a function of the refractive index variation of the glucose solutions of (a). The R^2 value of the linear fit is 0.9998, and the calculated bulk sensitivity is $S_b = 32.7(3)$ nm/RIU. This plot can be compared with Figure 2.7(a) and Figure 2.9(c), confirming the improvements of this setup.

duced, the LOD of this wedge-based sensor became

$$\mathrm{LOD} = 3 \times \frac{1.8(2) \times 10^{-4}\,\mathrm{nm}}{32.7(3)\,\mathrm{nm/RIU}} = 1.7(2) \times 10^{-5}\,\mathrm{RIU} \qquad (2.4)$$

according to Equation (1.12) and to the resonance wavelength uncertainty during water flow, which was $\sigma_\lambda = 0.18(2)$ pm.

2.1.3.3 VCSEL laser at 850 nm

The last optical setup presented in this thesis is the one built specifically to characterize the sensor chips developed within the European project Symphony. With the aim of realizing a low cost, disposable and integrated optical biosensor, the Symphony consortium has decided to use, as light source, the VCSEL diodes *U-L-M Photonics ULM850-B2-PL-S0101U*, which are sold as bare-dies, and can be bonded with a flip-chip method directly at the input of the waveguides.

The integration strategy of this laser source is quite complicated, and it is currently under development at the facilities of our partner

LioniX. In the meanwhile, as a temporary solution, we have built an optical setup based on fiber coupling (see §2.1.1), where the VCSEL source is the same, just in a more handy TO46 can, *ULM850-B2-PL-S46FZP*.

The particularity of these VCSEL diodes, that motivated their choice, is that they are single mode, polarization maintaining and can be tuned in wavelength by more than 1.6 nm, by changing the driving current. During the wavelength tuning, the probability of experiencing a mode-hop is low, because the vertical cavity is very short and, consequently, the FSR is large. Moreover, like any other VCSEL, the output beam is circular, and can be matched with reasonable efficiency to an optical fiber in butt-coupling.

We managed to pigtail our VCSELs to single-mode optical fibers, reaching an efficiency of 40 % (the fiber *Mode Field Diameter* (MFD) was 5 µm). Figure 2.16(a) shows the microscope picture of a TO-packaged laser diode during the procedure for the fiber alignment. When the correct position is found, a small drop of UV-curable glue is placed on the fiber tip. After a final alignment, the glue is cured with a UV-curing LED system. In a couple of minutes, the glue is hard, and the fiber is held in position. To increase the mechanical stability of the bonding, an additional drop of epoxy glue is put into the TO46 can, filling the empty volume. Finally, a short piece of shrinking tube is wrapped around the assembly, to protect the fiber from bend tensions.

To drive the VCSEL, the current has to be in the range from 2 mA (lasing threshold) to 6 mA (damaging threshold, output power 2 mW). This range is too small to be accurately tuned by most of the commercially available laser drivers, which are designed to work in a current range of the order of 100 mA. To overcome this problem, we connected the laser in series with a resistor of $R = 550\,\Omega$, and we drove it directly by setting the voltage with a function generator, *Tektronix AFG3000*. The current, in fact, is so low that the generator is able to source it without any additional amplifier.

Figure 2.16(b) shows the calibration curves for the emission wavelength, measured with an OSA, as a function of the driving voltage. We fit the data with polynomial functions, with degree from first to fourth. The analysis of the residuals of the fitting, in the inset, shows that a polynomial degree of 3 is a good choice, and that increasing the order does not reduce significantly the fit error. Thus, from the fitting coefficients, in the sensing experiments we could calculate the

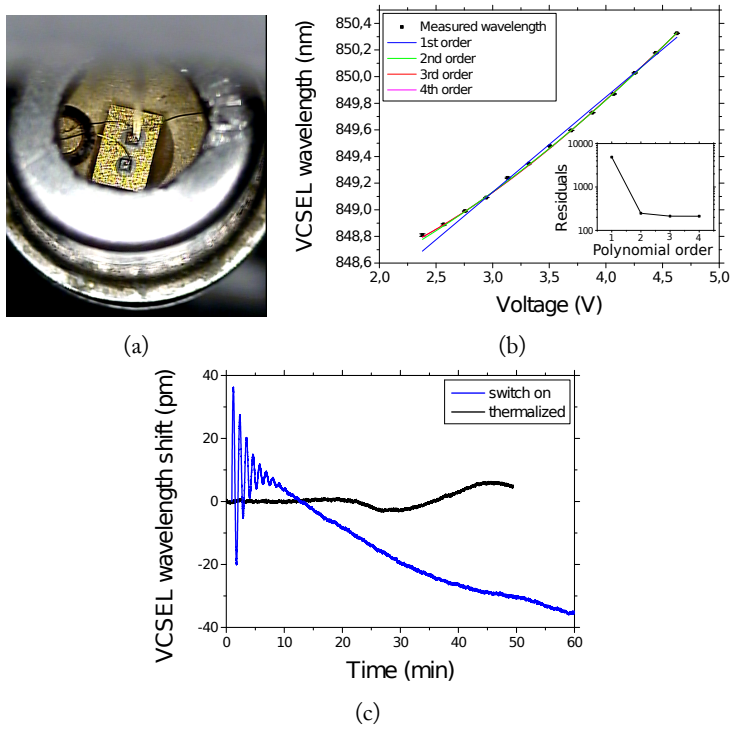

Figure 2.16: (a) Microscope picture taken during the fiber pigtailing of the VCSEL source. (b) Calibration of the lasing wavelength of the VCSEL, as a function of the driving voltage. The wavelength has been measured with an Optical Spectrum Analyzer (average uncertainty 5 pm). The continuous lines are polynomial fitting of the datapoints (up to the fourth order). The inset shows the sum of the squared residuals as a function of the order of the polynomial model. (c) Wavelength drift during the thermalization of the VCSEL. The blue curve has been recorded starting from the switching-on of the temperature controller of the VCSEL. The drift persist for more than one hour. The black curve has been recorded after the thermalization.

emission wavelength by measuring the driving voltage.

The last plot, shown in Figure 2.16(c), represents the characterization of the wavelength stability. This has been measured with the same setup of Figure 2.11. The only differences are that the amplifier was not necessary, and that the two photodetectors are two switchable-gain amplified silicon detectors, *Thorlabs PDA36A*. The WGM under test is a racetrack in SiO_xN_y, from the batch L2 of the Symphony project (see Table 4.1). The resonator is kept in static water (no flow), at constant temperature. Therefore, the measured wavelength shift is actually due to the shift in emission wavelength from the VCSEL. The blue curve has been measured immediately after the switching-on of the temperature controller of the laser diode. As expected, the emission wavelength drifts with the temperature, but the issue here is that the controller takes more than one hour to reach a complete thermalization. In contrast, the black curve has been measured at equilibrium. The short-term (2 min) wavelength uncertainty is as low as 0.07 pm, but bigger fluctuations can arise in the long term.

This VCSEL, and the setup of Figure 2.11, has been used to characterize the samples described in §4.1, and it has been used to successfully detect Aflatoxyn M1 down to nanomolar concentrations, as reported in §4.2.

2.2 Liquid samples handling

In order to reduce the limit of detection of a biosensor, it is important to have a well developed optical setup, an optimized sensing element and, finally, a reliable system to handle the flow of the liquid samples. The micrometric size of the photonic structures, allows for the use of very small sample volumes, in the microlitre or, even, nanolitre range. Obviously, the handling of such low amount of liquid is very challenging, and requires capillaries, microchannels and microvalves, in order to be successful. This microfluidics, opens a whole new world of physical effects, that can be studied or exploited [90].

In this thesis, we will use only very basic microfluidic elements. The general scheme of the liquid handling systems consists in a dispenser, or a pump, that pushes the samples through one or more capillaries, down to a flow-cell, and then to a waste bottle. The flowcell is a microchannel, open on one side, that is leak-tight bond to the

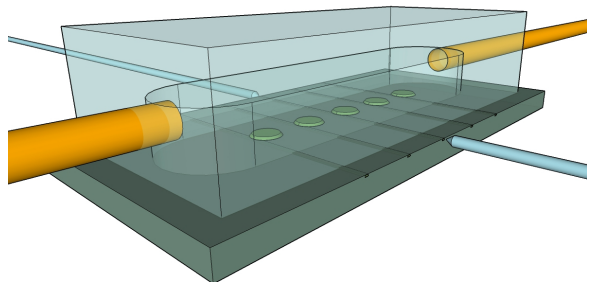

Figure 2.17: Schematic representation of a flowcell. The microfluidic is leak-tight to the photonic chip. All the resonators are flood simultaneously, and exposed to the same sample solution. The inlet and outlet capillaries are depicted in orange, while the tapered fibers for light-coupling are depicted in light blue, at the edges of the chip.

sensing area of the chip. Thus, the sensor can come in contact with the liquid through the aperture, and it can analyse its content. Figure 2.17 represents a sketch of a typical flowcell, covering the sensing area of few WGM resonators.

The next sections will cover, first, the sources of flow that we used in our experiments, and, second, the two flowcells that we developed.

2.2.1 Pressure-driven pulsed flow

The first source that we developed is a pressure-driven dispenser, based on an *Eppendorf FemtoJet*. This device is nothing more than an air compressor with a regulated valve, that can apply a specific pressure in arbitrarily-long pulses. The pulsed regime can be convenient when the sample volume is really small, being able to deliver just the desired amount of liquid at will.

In order to dispense more than one sample, we realized an homemade switch-box, with five electrovalves controlling the flow of air applied by the *FemtoJet*. Figure 2.18(a) shows a picture of the switch-box, connected with a tube to the *FemtoJet*, while Figure 2.18(b) depicts schematically the concept of this apparatus. Five pipette tips (volume $\approx$ 50 µl) are initially filled with different solutions. These are, on one side, connected to the flowell via five capillaries, and, on the other side connected to the electrovalve controller. Typically, one

(a) (b)

FIGURE 2.18: (a) Picture of an *Eppendorf FemtoJet* and of the home-made electrovalve controller. (b) Schematic representation of the pressure-driven microfluidic apparatus. Up to five *Eppendorf* pipette tips can be filled with the analyte samples, the blank solution and the regeneration solution. The flow of the liquids towards the biosensor is regulated by the electrovalves in the controller.

channel is open at a time. When the *FemtoJet* is activated, the pressure pulse pushes the liquid of the selected pipette tip, feeding it to the sensor.

Unfortunately, this approach is affected by at least three issues:

1. In some cases, we noticed a backflow, progressing from one tip, to the flowcell, and back to another tip.

2. When the liquid is not exactly at the same temperature of the sensor, at every injection we noticed a small variation of the resonance wavelength, even if the injected solution was always the same (with no change in refractive index). Figure 2.19(a) shows an example of such issue. The injections, marked by the red arrows, produce sudden shifts of up to ≈3 pm, that are restored only after more than 10 min.

3. It is difficult to remove all the air bubbles from the capillaries, prior to the sample injection. This trapped air is then pushed, together with the liquid, towards the sensor area. When a bubble crosses the flowcell, the sensor is momentarily dried, and the salts, contained in the buffer solution of the sensing experiments, can deposit on its surface. The superficial interaction of the newly-formed crystals is very strong, so that even when

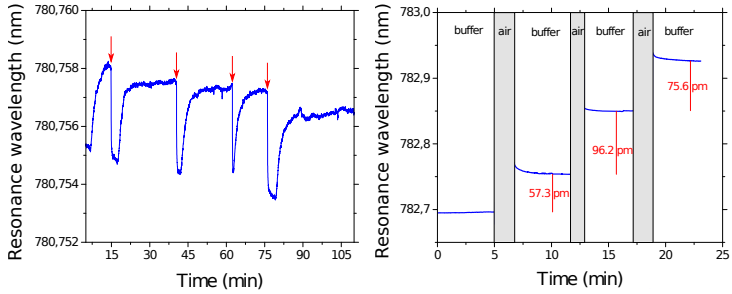

(a) (b)

Figure 2.19: (a) Resonance shift upon pulsed injections with the fluidic setup of Figure 2.18(b). The pulsed flow change the resonance wavelength by up to ≈3 pm, probably because of a small offset between the temperature of the liquid and of the resonator. (b) Residual resonance shift, observed after the temporary exposure of the resonator to an air bubble. In this controlled experiment, three air bubbles are flown in sequence, producing a cumulative shift of 230 pm. On average, the step-shift is ≈80 pm.

the sensor is again flood with the buffer solution, this deposited layer can not be entirely dissolved. Figure 2.19(b) reports on a controlled experiment, where we cycled between injections of buffer solution and air. As it can be seen, after every cycle a residual shift is measured, with an average step of ≈80 pm. Such an effect is unacceptable during a biosensing experiment, and for this reason any air bubble should be avoided during the injections.

2.2.2 Syringe-pump continuous flow

To overcome the issues of the pulsed flow, we built a microfluidic apparatus based on a positive displacement pump and on a 6-way loop injection valve. We choose a *VICI M6* syringe-free pump and a *VICI C1CF* valve, which are shown in Figure 2.20(a) and (b), respectively.

The pump is able to feed an unlimited volume of carrier solution, usually the incubation buffer, to the sensor without interruptions. This device combines a smooth flow, typical of syringe pumps,

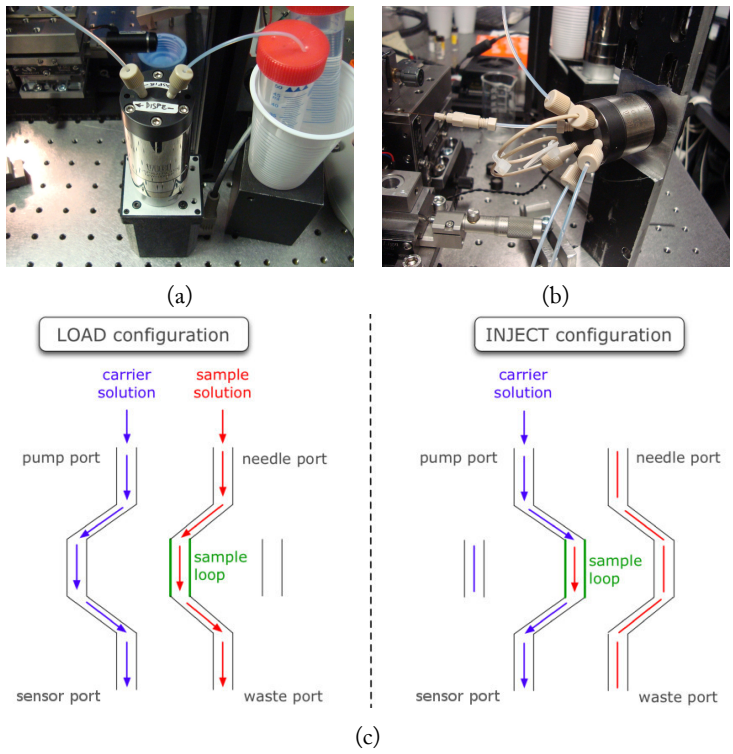

FIGURE 2.20: (a) Picture of the *VICI M6* continuous flow pump, connecting a buffer reservoir to the injection valve. (b) Picture of the *VICI C1CF* injection valve, with a sample loop calibrated to 20 µl. (b) Schematic representation of the working principle of an injection valve. When the valve is in "load" configuration, the sample loop can be filled with the analyte solution through the needle port. Contemporaneously, the flow of the carrier solution towards the WGM sensor is uninterrupted. When the valve is in "inject" configuration, the carrier solution pushes the fixed-volume plug of analyte solution towards the sensor. Scheme adapted from [83].

with the unlimited reservoir volume, typical of peristaltic pumps. The continuous flow stabilizes the resonance wavelength, even if the temperature of the fluid is not exactly the same of the photonic chip, preventing the spikes observed in Figure 2.19(a).

By adopting an injection valve, small volumes of sample solutions can be delivered to the sensor as small liquid plugs, embedded in the continuous stream of carrier buffer. Figure 2.20(c) schematizes the working principle of such valve. When the handle is set to "load", the inner rotator connects the needle port to the sample loop (i.e., a piece of tube of known volume) and the pump port to the sensor port. In this way, it is possible to fill the sample loop with the target solution, without interrupting the flow towards the sensor. When the handle of the valve is set to "inject", the inner rotator switch the connections, directing the needle port directly to the waste, while the flow of carrier solution pushes the sample in the capillaries towards the sensor.

The continuous flow consumes a bigger amount of buffer solution, in comparison to the pulsed flow, but this is not a problem because the buffer is inexpensive. In contrast, the volume of sample solution can be reduced at will by changing the length of the sample loop. In addition, the continuous flow purges the capillaries from trapped air, and every injection can be reproducibly performed "bubble-free".

2.2.3 Microfluidic flowcells

2.2.3.1 Homemade PDMS flowcell

The development of a reliable and small-volume flowcell required many trials-and-errors. Here, we will describe the procedure that provided the best results.

The minimum requirements were:

- The cell has to be transparent, in order to be easily aligned to the sensing structures.
- It should form a good sealing with the chip.
- It should be easily removed and remounted, to allow for multiple functionalization of the sensor surface.

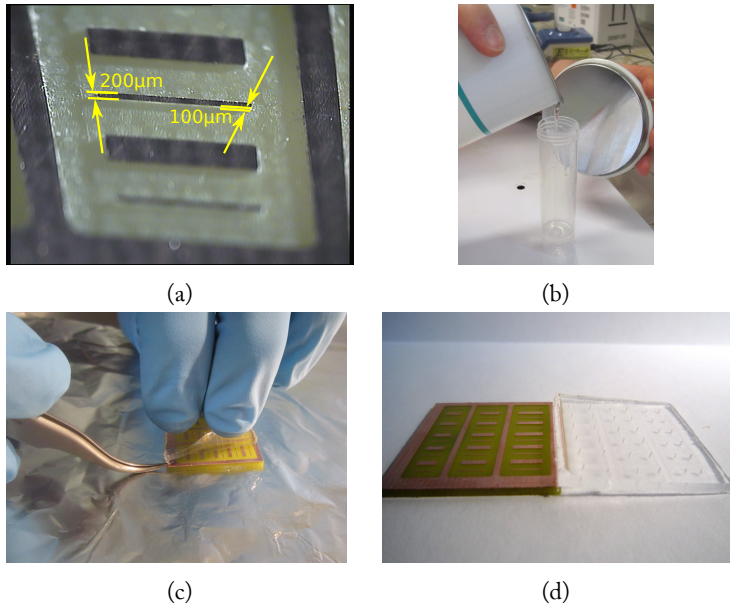

(a) (b)

(c) (d)

FIGURE 2.21: (a) Microscope picture of the PCB used as mold for the PDMS flowcell. The cross-section of the microfluidic channel is 200 µm × 100 µm (width × height). (b) Preparation of the PDMS mix. (c) Removal of the PDMS flowcells from the mold. (d) After the casting, the PDMS is punched or drilled to realize the vertical holes (vias), which will link the inlet and outlet capillaries to the incubation channel.

- The central channel should be as small as possible, ideally slightly larger than the WGM resonator itself, and about 100 µm height. The reason is that, for a given speed of the solution flowing above the sensor, the flow rate is proportional to the cross-section area of the channel. Therefore, a smaller area can lead to lower values of the flow rate, that consume less amount of analyte.

In order to obtain a leak-tight sealing between microfluidic and chip, we decided to build our flowcell in a soft polymer: the PDMS. This elastomer has been vastly adopted in the field of microfluidics, because it can be easily cast, even in molds with submicrometric fea-

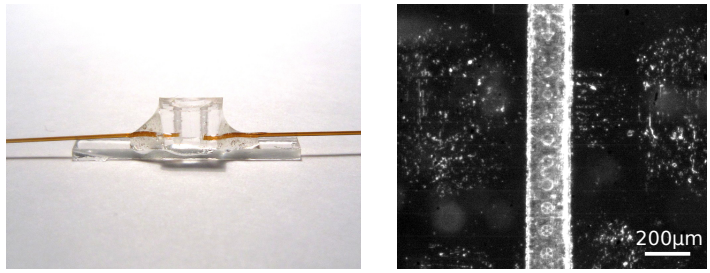

(a) (b)

Figure 2.22: (a) Side view of a PDMS flow-cell. The capillaries have an inner diameter of 150 µm, and penetrate the polymer to reach the vertical vias. The assembly is fixed to a glass substrate with epoxy glue. (b) Microscope top-view picture showing the perfect alignment of the flowcell to the microdisk and wedge resonators on the photonic chip.

tures. When solid, its elastic properties make it a good sealant. Our WGM resonators have diameters in the range from 50 to 200 µm, and the sensor chips are typically 3 to 5 mm large, limiting the maximum (external) width of the cell. We obtained a good compromise, in terms of resolution, fabrication time and flexibility, by using a milled PCB as a mold for the PDMS casting. The lateral resolution of the mill is certified by the constructor to be better than 100 µm, but nothing is specified about the vertical axis. Thus, we calibrated the milling depth with a profilometer, obtaining a vertical resolution of 3 µm and an absolute accuracy of $\lesssim$ 10 µm.

In Figure 2.21(a) we show a microscope picture of our mold. The dark parts are the residuals of copper foil of the PCB, while the bright parts have been milled. In this case, we fabricated thin wires of 200 µm width and 100 µm height. The PDMS is prepared by mixing the elastomer, *Dow Corning Sylgard 184*, with the curing catalyst in 10:1 ratio. While the mix is still liquid, it is poured on the mold and placed in a vacuum chamber (low vacuum is sufficient) to degas. The curing can be obtained either at room-temperature, in 48 hours, or in an oven at 150 °C for 10 minutes.

Figure 2.21(c) shows the careful removal of the cast flowcells. Then, for an easier connection of the inlet and outlet capillaries to

the microchannel, we drilled (or punched) vertical vias at both ends of every channel, as shown in Figure 2.21(d). Up to 18 flowcells can be cast on the same mold, where every flowcell is 2.5 mm wide and from 5.5 to 7.5 mm long.

Then, every flowcell is singulated by cutting the rubber with a knife. The inlet and outlet capillaries are inserted in the polymer, with the help of a syringe needle, down to the vertical vias. The PDMS and capillaries are fixed to a glass substrate with epoxy glue, to give mechanical stability to the assembly. Figure 2.22(a) shows a side-view picture of a finished flowcell.

Finally, the flowcell is positioned onto the sensor chip with micrometric precision by using the same translation stages used for the fibers alignment. Despite the small width of the microchannel, it is possible to precisely align it to the resonators, as represented in the microscope picture of Figure 2.22(b). Once aligned, the flowcell is gently fastened with the screws of the chip holder, as shown in Figure 2.3(b).

The method here proposed for the realization of the microfluidic cell is simple and versatile. However, the coupling with the capillaries requires practising and it is not completely reproducible. In addition, the use of a PCB-mold limits the design to planar channel structures. Despite these issues, we realized many flowcells, and we successfully used them in all the experiments of §4.1 and §4.2.

2.2.3.2 Professional PMMA flowcell

Finally, we conclude this chapter by presenting the design and the first realization of a professional-grade flowcell. Epigem, one of the partners of the Symphony project, is specialized in the realization of microfluidics. They are able to work with many different materials, mainly plastics, and are able to produce 3D microfluidic structures by stacking several layers one over the other.

With their collaboration, we designed a flowcell that could also serve as chip-holder. We chose PMMA (also known with the commercial name of *Plexyglass*) as main material, because it is inexpensive, rigid and transparent. By milling it, Epigem can realize microcapillaries with width of 100 µm and height down to 10 µm.

The flowcell that we designed is represented in Figure 2.23(a). It is composed of four main blocks:

- A connector block (blue in the drawing), with threads for *Chem-inert* tube fittings.
- The main substrate (pink in the drawing), that provides the fluidic connections to the flowcell.
- The chip-holder (light-blue in the drawing), that keeps the sensor chip in position, aligned to the flowcell.
- The removable lid (green in the drawing), that closes the holder and allows for an easy replacement of the sensor chip.

Figure 2.23(b), in particular, shows a zoomed view on the flowcell. The PDMS (in red) both creates the sealing with the chip and defines the sensing volume, which has dimensions $2 \times 6 \times 0.150$ mm.

This microfluidic can serve both the sensor chips fabricated by the FBK and the ones designed by LioniX. Figure 2.23(c) shows the first demonstrator of the sensing unit of the Symphony project. A chip is placed into the microfluidic platform, and it is glued to the VCSEL light source and to the output fibers (photodetectors not shown), while the inlet and outlet tubing are fixed to the connector block.

At the moment of writing, we did not have the chance to test this microfluidic thoroughly, but it will be one of the next activities within the Symphony project.

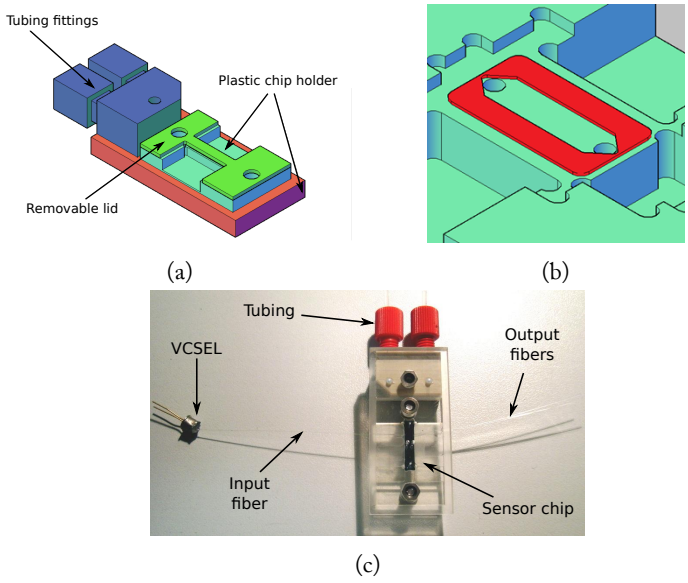

FIGURE 2.23: (a) 3D drawing of the proposed microfluidic chip-holder. The tubing can be easily fixed with the leak-tight fittings. The photonic chip is placed in-between the chip holder and the removable lid. The fluid is conveyed through small capillaries from the inlet to the sensing area of the chip. (b) Zoomed view on the incubation chamber. The two holes are the inlet and outlet for the fluid, while the red part is the PDMS gasket that ensures a leak-tight connection to the optical sensor (in this case positioned upside-down on top of the gasket). The sensing volume is $2 \times 6 \times 0.150\,\text{mm}$. (c) Picture of the first prototype developed by the Symphony consortium. The sensor chip is placed into the microfluidic platform, and it is glued to the VCSEL light source and to the output fibers (photodetectors not shown).

Chip design 3

This and the following chapters are focused on the activities performed within the scope of the FP7 EU project Symphony. The project aims at realizing a photonic sensing unit based on a low cost and fully integrated optical sensor, to be operated in the NIR ($\sim$ 850 nm). The chosen technology is the CMOS. The sensing elements will be based on WGM MRRs and/or aMZIs. Both the excitation laser source (a low cost VCSEL diode) and the detectors (Si-photodiodes) will be integrated by butt-end coupling. Moreover, a new technology for the monolithic integration of a Si-photoconductive detector will be developed and tested. A simple sketch of the chip conceived by the consortium is depicted in Figure 3.1.

The consortium partners that are involved in this task are UniTN, as the work-package leader, FBK and LioniX. While LioniX focused on the design and fabrication of the aMZIs sensors, the MRRs sensors have been designed in close collaboration between UniTN and the APP group of FBK. Please note that, initially, we were planning to realize wedge resonators, as we already demonstrated their monolithic integration and their high quality factors [34]. However, when the Symphony project started, the machine for the BPSG deposition (necessary for the realization of the vertical coupling to the wedge structures) suffered from sever issues, and we had to revert to the use of horizontally-coupled MRRs. These sensors have been fabricated

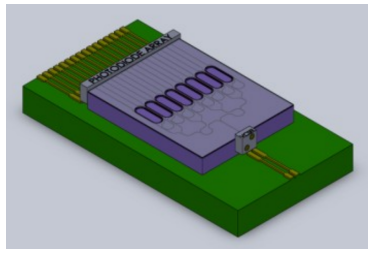

Figure 3.1: Simple sketch of the sensor's chip conceived by the Symphony consortium. Multiple sensing sites are driven by the same VCSEL source and read simultaneously by an array of photodetectors. The top cladding has opening windows to allow the interaction with the analyte. Taken from [45]

.

by FBK and then tested, together with LioniX's aMZIs, at UniTN.

During my Ph.D. work I've collaborated in the design of the MRRs chip. For this reason, this section will cover only the simulations and design of the structures related to the MRRs sensors. Details about the design of the aMZIs can be found in [91].

3.1 Materials

As explained in §2.1.3.3, the Symphony consortium decided to develop sensors to be operated in the VIS-NIR range. This strategic choice has the aim of realizing a low cost and integrated optical biosensor. In this wavelength range, in fact, it is possible to integrate cheap silicon photodetectors directly on-chip. Moreover, there exist commercially-available single-mode VCSELs sources, that are sold as bare die and that can be coupled to the sensor through flip-chip technology. The final choice has been the VCSEL diode *U-L-M Photonics ULM850-B2-PL-S0101U*, which operates at a wavelength of 850 nm.

Among the Si-based materials transparent at such wavelength, FBK and UniTN decided to adopt a *Plasma-Enhanced Chemical Vapor Deposition* (PECVD)-deposited SiO_xN_y, as the material for the core of their devices, while LioniX based its ones on *Low-Pressure Chemical Vapor Deposition* (LPCVD)-deposited Si_3N_4. These mate-

rials are compatible with the chemistry selected for sensor functionalization. For both the MRRs and the aMZIs, the cladding of the photonic circuit will be SiO_2 or air, respectively for the protected or sensing zones.

In particular, the choice of the SiO_xN_y is strategical for two reasons:

- by varying the relative amount of nitrogen and oxygen, the refractive index of the dielectric can be tuned continuously between 1.45 and 2.0 (refractive index of SiO_2 and Si_3N_4, respectively);
- the strain created at the silica-SiON interface can be relaxed by reducing the content of nitrogen. This reduces the optical scattering losses while still preserving a reasonably high refractive index contrast with the silica cladding.

High refractive index contrast is preferred to allow smaller photonic features/structures, however at the cost of increased material losses which can reduce the quality factor of the MRRs sensors. In order to evaluate the quality of the materials and the corresponding effects on the sensing performances, we have decided to test two different SiON compositions. The first one is a low-stress and low-contrast SiON with a refractive index of 1.66. The second one is a high-stress and high-contrast SiON with refractive index 1.80.

3.2 Objectives

For an easy handling of the sensor, the chip's overall dimensions have been set to 10 mm $\times$ 10 mm. However, the typical dimensions of MRRs in SiON are in the order of 10 to 100 µm, and 100 to 1000 µm in the case of aMZIs. Thus, the sensing area, which has to be flood with the analyte solutions, has been restricted to a rectangle of 2 mm $\times$ 6 mm. Taking into account a microfluidic height of about 150 µm, this leads to a total sensing volume of less then 2 µl.

The specifications in the Symphony agreement require a minimum of 2 and a desiderata of > 8 sensing sites. For the prototype chips, we started with the development of an integrated optical circuit with 4 sensing sites.

The European Commission regulation (EC No. 1881/2006) sets a maximum allowed level of *Aflatoxyn M_1* (AFM1) in milk equal to

50 ppt, or 25 ppt for infant formulae, as a vulnerable group of the population. To achieve such a demanding resolution, the Symphony consortium is developing a pre-concentration unit that should be able to concentrate the toxin molecules by a factor 1000. As such, the required limit of detection for the MRRs or aMZIs sensors is 152 nM, or 76 nM for the infants[1].

The LOD for surface sensing depends on the surface sensitivity of the sensor, but also on many other factors, among which aptamers surface concentration, incubation time, liquid sample flow rate, microfluidic geometry, etc. On the contrary, the bulk LOD, LOD_b, and the bulk sensitivity, S_b, only depend on the sensor itself and on the readout instrumentation. For this reason, the MRRs and aMZIs sensors are also evaluated in terms of bulk sensing characteristics. The specifications in the Symphony agreement require a maximum bulk LOD_b of 1×10^{-5} RIU for the prototyping test chips and a maximum bulk LOD_b of 1×10^{-6} RIU for the final sensor.

3.3 Waveguides

To set the waveguide dimensions we initially considered the SiON composition with lower refractive index ($n = 1.66$). From previous works conducted during the NAoMI project, we knew that with such composition it was possible to realize low-loss waveguides with thickness up to 300 nm. Thus, we fixed the thickness to be 300 nm and we run several FEM simulations to find the cut-off width at which the multimodal propagation is prevented for wavelengths longer than 780 nm. We decided to keep this wavelength, instead of the VCSEL's one, to be able to test the structures also with the laboratory-grade tunable laser unit (see §2.1.3.2).

In the simulations we used SiO_2 as the cladding material and SiON for the core. One picture representing the calculated mode profile of a waveguide with core refractive index 1.66, is shown in Figure 3.2. We found that to prevent multimodal propagation, the waveguide width should be smaller than 1.2 µm. To guarantee single-mode operation and to limit propagation losses, we decided to keep a safe width of $900-1000$ nm. In the design of the mask for the prototyping chips, we reserved several test structures to allow for the measurement of propagation and bending losses for both widths. More-

[1] AFM1 molecular weight is 328.27 g mol^{-1}.

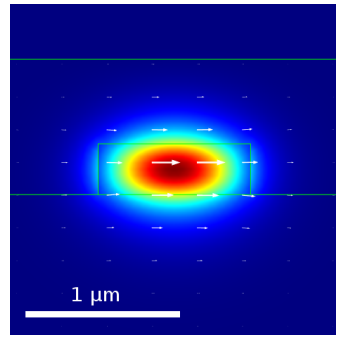

FIGURE 3.2: Electric field intensity (colormap) and direction (arrows) for the supported TE polarization. The cladding material is SiO_2 and the core material is SiON with refractive index 1.66.

over, from the simulations we found that a top cladding of thickness at least 500 nm is necessary to properly isolate the guided mode.

3.4 Splitters

The simultaneous driving and reading of more than one sensing site requires splitters to route equally the incoming light. The structures of usual choice to achieve this are:

- Y-junctions;
- multi-mode interference (MMI) splitters;
- directional couplers.

The first ones are really simple and compact, but usually suffer from high insertion losses, caused by the scattering at the tip of the junction. This is especially true if the photolithography resolution is not high enough. The second ones are bigger and less affected by the resolution, but need special cares in the design to achieve low insertion losses. The last ones are also quite simple and allow the control of the splitting ratio. However they suffer for size, wavelength bandwidth and polarization dependence. In our application, the size is not a severe constraint, the wavelength bandwidth is small (fixed by the emission of the VCSEL source) and the polarization dependence is

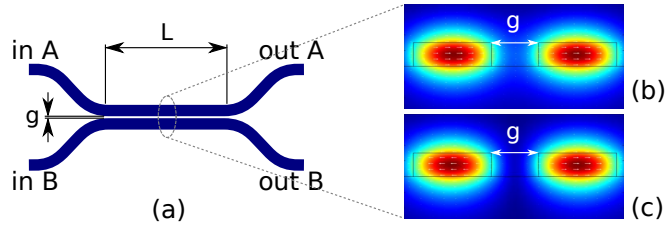

Figure 3.3: Schematic representation of a directional coupler. Two waveguides are brought close to each other. They are separated by a gap, g, and the length of the coupling region is L. (b),(c) 2D cross-section simulation of the electric field norm for the supported TE modes in the coupling region. The gap is $g = 600\,\text{nm}$. (b) TE even mode (symmetric). (c) TE odd mode (antisymmetric).

actually a favouring characteristic, as it can help distinguish TE and TM modes (since the waveguide can sustain both). For these considerations, we decided to opt for directional couplers.

Figure 3.3(a) shows the schematic representation of a directional coupler. In this device, two closely-separated and parallel waveguides are coupled through their evanescent fields. The coupling region is characterized by a gap g and a length L. The coupling breaks the degeneracy of the two modes supported by the two (separate) waveguides, and creates coupled hybrid *even* (symmetric) and *odd* (antisymmetric) modes (see Figure 3.3(b) and (c)). The length of the coupling region, which is needed to completely transfer the light power from the input A to the output B, is called *Coupling Length* L_{cp}. To calculate this value and to properly design our splitters we used the *Coupled Mode Theory* (CMT) [92]. From the laser wavelength λ and the effective refractive indexes of the even (n^e_{eff}) and odd (n^e_{eff}) coupled modes, we can calculated L_{cp} as

$$L_{cp} = \frac{\lambda}{2(n^e_{eff} - n^o_{eff})} \tag{3.1}$$

In the design of the splitter, we also considered possible fabrication defects due to a limited photolithography resolution. The FBK fabs declare a tolerance in lateral dimensions of 20 nm. Thus, we simulated the variations in the coupling lengths for directional couplers with gaps of 400, 500 and 600 nm, adding to the nominal value of the

waveguide width small variations in the range from ± 20 to 60 nm. The results of this analysis are reported in Figure 3.4(a).

As expected, the wider gap (600 nm) is more robust to waveguide dimensions variations. Another important consideration is that a lateral tolerance of 20 nm can cause variations in L_{cp} as high as 10 %. Since the transferred power along the propagation direction follows a squared-sine law

$$I(z) = I_0 \sin^2 \left(\frac{\pi}{2} \frac{z}{L_{cp}} \right) \tag{3.2}$$

a $50/50$ splitter is achieved when the coupling region has a length $L_{50} = L_{cp}/2$. By means of Equation (3.2), it is also possible to calculate the influence of the photolithography resolution on the splitting ratio. As plotted in Figure 3.4(b), we found that fabrication errors can modify the output power by about ± 10 %.

This analysis demonstrated the feasibility of the device, but also remarked its sensitivity to fabrication defects. A complex circuit with many cascaded splitters can not be reliably realized with such technology. Since in our sensors we only need two cascaded splitters (to build a 1×4 splitter), we decided to test the use of these directional couplers. If in the future the integrated sensor will be developed with 8 or more sensing sites, the use of MMI splitters should be taken in consideration.

Lastly, to validate the results obtained with the CMT, we performed a 2D top-view FEM simulation. For this simulation, the first step has been the tuning of the refractive indexes of core and cladding regions. In the top-view configuration, in fact, we lose the information of the waveguide thickness (it is assumed to be infinitely thick). To mimic an effective 3D structure in the 2D top-view analysis, we varied the refractive indexes of core and cladding region of a straight waveguide, until the propagation constant and confinement factor[2] matched the same values of a 2D cross-section simulation. Once found, we used these refractive indexes (reported in Table 3.1) to simulate the splitter, and we tuned the length of the coupling region to obtain a balanced output from the two waveguides. The result is depicted in Figure 3.5.

[2]here defined as the normalized line integral of $|E|^2$ across a horizontal line passing in the core region through the center of the guided mode.

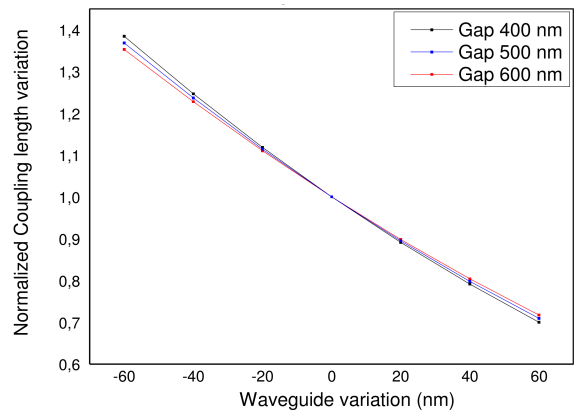

(a)

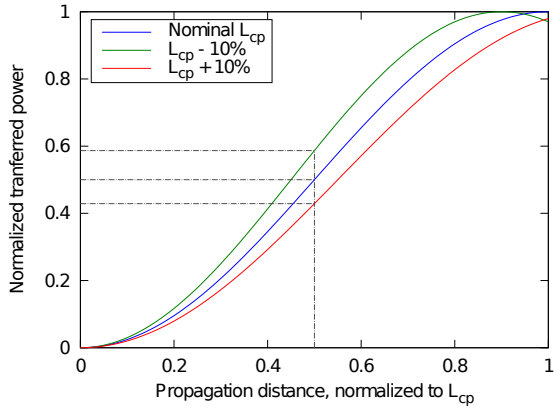

(b)

Figure 3.4: (a) Normalized coupling lengths L_{cp} as a function of variations in waveguide and gap size. The values are normalized to the nominal coupling length (nominal waveguide width 900 nm). (b) Variation in transmitted power along the direction of propagation for errors in L_{cp} equal to $\pm 10\,\%$.

Table 3.1: Effective parameters to match cross-section and top-view 2D FEM simulations.

Parameters	Cross-section	Top-view
Waveguide width	900 nm	900 nm
Waveguide thickness	300 nm	–
n_{SiO_2}	1.45	1.386
n_{SiON}	1.66	1.541
Effective index	1.503	1.503
Confinement factor	0.892	0.892

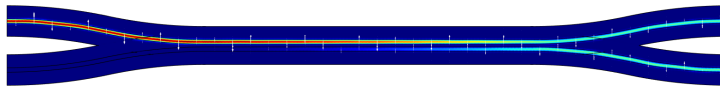

FIGURE 3.5: Top-view FEM simulation of the directional coupler 50/50 splitter, illuminated with TE light from the north-west port. The waveguide width is 900 nm, the length of the coupling region is 68 µm, and the gap between the waveguides is 600 nm.

The coupling lengths calculated with the two methods are significantly different. For a waveguide width of 900 nm and a gap of 600 nm, the CMT predicts a length $L_{50} = 55\,\mu m$, while with the FEM analysis we found $L_{50} = 68\,\mu m$. We think that the reason for such a difference should be searched in the top-view method that, even with the precautions explained above, is probably not well suited to substitute a full 3D simulation. Unfortunately, a full 3D simulation of such a big structure demands huge computational resources that were not available. Therefore, we accepted under reserve the CMT results, and decided to check on both methods experimentally. We designed test structures with different coupling lengths, ranging from 50 to 75 µm for waveguide width 900 nm, and from 65 to 90 µm for waveguide width 1000 nm.

3.5 Ring resonators

The part of the sensor that most critically affects its performances is the transducer, i.e., the MRR. A general rule for the design of a sensor with a good SNR is to use the microring in a slight undercoupling

regime, so to guarantee a large quality factor while still preserving a sizeable resonance dip in the transmission spectrum. Tuning the coupling is not a problem with off-chip tapered fibers, but it becomes challenging for resonators with integrated on-chip bus waveguides. The reason is that an efficient and optimized design depends on the MRR quality factor, which is impossible to calculate without *a priori* knowledge on the fabrication details (see §1.2.1). To address this problem, we based our design on both theoretical calculations and on the realization of several test chips.

The first analysis involved the calculation of the radiation losses. These are important for the design of the resonator but also for the design of all the bent waveguides that are used to route the light on the chip. The radiation towards the outward direction of a bent waveguide increases with decreasing radius and with decreasing refractive index contrast. To efficiently simulate these effects, we used a conformal transformation of the waveguide geometry and refractive index, as explained in [93, 94].

Shortly, we modeled the geometry of a curved waveguide with bending radius R by mapping its cylindrical coordinates (r, θ, z) to the conformal coordinates (u, v, z) as follows

$$u = R \ln \frac{r}{R} \tag{3.3}$$

$$v = R\,\theta \tag{3.4}$$

To satisfy Maxwell's equations, this transformation has to map also the real refractive index in the conformal index given by

$$n_t = n \exp \frac{u}{R} \tag{3.5}$$

The advantage of this conformal transformation is that it maps curved 3D waveguides in straight waveguides, with a refractive index that vary only in the (u, z) plane. This problem can be treated efficiently with 2D FEM simulations.

Since the radiation increases with reduced contrast, the parts of the circuit which mostly suffer from radiations are the routing bends (like the ones before and after any directional coupler), where the SiON core is surrounded by silica cladding. We thus simulated waveguides with width $w = 900\,\text{nm}$ and refractive index $n = 1.66$, embedded in silica (refractive index 1.45) and covered by air. Two of these simulations are reported in Figure 3.6. In (a) the bend radius

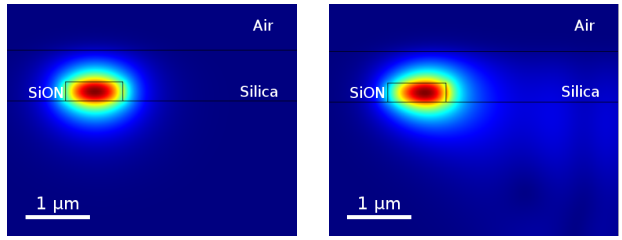

(a) (b)

FIGURE 3.6: Cylindrical-coordinates cross-section FEM simulation of a SiON resonator with bending radii (a) $R = 250\,\mu m$ and (b) $R = 25\,\mu m$. The displacement of the mode and the radiated power towards the outward direction (right side of the figure) are evident in the latter case.

is $R = 250\,\mu m$, while in (b) the bend radius is $R = 25\,\mu m$. We can notice that at short radii the mode is pushed to the exterior of the waveguide (increasing the surface scattering) and that the confinement of the mode is poor.

With the implementation of a PML at the boundaries of the simulation domain (see also §1.2.2), we could calculate the losses and the attenuation constant of this waveguide as a function of the bend radius R, as it is reported in Figure 3.7(a). For radii longer than $\sim 100\,\mu m$ the effect of radiation is negligible, and the losses are constant and equal to the material absorption losses (measured as ~ 0.1 dB/cm in a preliminary experiment on straight waveguides with similar dimensions and also reported in [95]). For shorter radii, the radiation starts to become dominant, growing exponentially and soon exceeding 1 dB/cm. For this reason, we decided to make all the bends in our circuit with $R = 100\,\mu m$ to limit to the minimum the losses in all the parts of the chip.

As a comparison, we also calculated the bending radiation losses for a waveguide with the same geometry but higher refractive index contrast. We simulated a Si_3N_4 waveguide, omitting the material absorption to better highlight the contribution of just the radiation losses. As we can see from Figure 3.7(b), the radiation losses start to be significant only for radii shorter than $R = 7\,\mu m$. This confirms our expectations, and it paves the way for the reduction of the res-

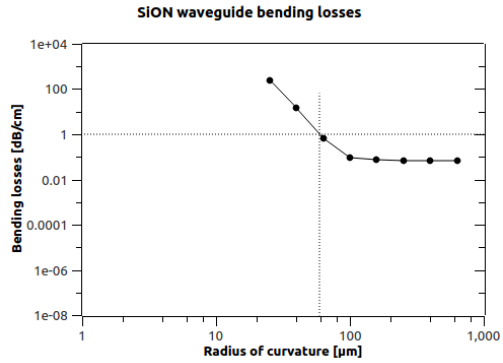

(a)

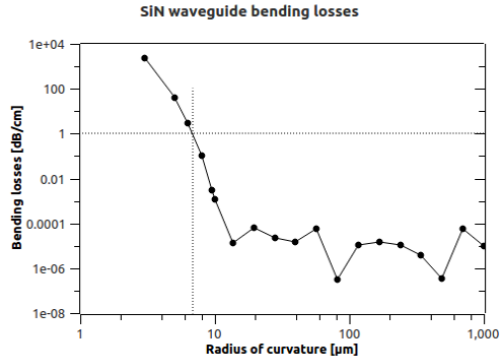

(b)

Figure 3.7: (a) Calculated bending losses and absorption losses for a SiON waveguide with refractive index $n = 1.66$. Radiation is negligible for $R \gtrsim 100\,\mu m$. (b) Calculated bending losses for a SiN waveguide with refractive index $n = 2.01$ (we omitted absorption losses here). Bending losses are significant only for $R \lesssim 7\,\mu m$. For longer radii the losses are induced by the numerical discretization.

onator size if dense multi-analyte sensing will become a necessity in the future.

To confirm these calculations and to measure also the scattering losses (that were not considered up to now), we designed on the photolithography mask several test structures with multiple bend radii of 100, 75, 50, 25, 10 and 5 µm, for both waveguide widths of 0.9 µm and 1.0 µm.

To conclude with the design of the MRR sensor, we had to calculate the coupling coefficient to achieve the critical coupling condition. As said before, it was not possible to calculate it without knowing the total losses in the cavity. However, by taking into consideration a range of possible values, we estimated the required coupling lengths. Based on this estimates, we designed several test structures to be able to measure experimentally the coupling coefficient. To calculate the range, we used the following procedure:

1. as lower limit for the attenuation constant in the ring, we used the loss coefficient that was measured for previous works in straight SiON waveguides. We have $\alpha = 0.1\,\text{dB/cm} = 0.023\,\text{cm}^{-1}$. Note that with this α the maximum quality factor could be calculated, using Equation (1.27), leading to $Q_0 \lesssim 5 \times 10^6$.

2. The maximum limit for the attenuation constant was estimated by knowing that FBK's fab was able to achieve loaded Q values in the order of 10^4 with smaller structures. Again, by using Equation (1.27) we found $\alpha \lesssim 10\,\text{cm}^{-1}$.

3. Then, we calculated the maximum and minimum round-trip loss for a resonator with $R = 100\,\mu\text{m}$ as $a = \exp(-\pi R\alpha)$. At critical coupling, the field transmission coefficient is $t = a$ (see Equation (1.23)) and, as always, we have $t^2 + k^2 = 1$, so that $k = \sqrt{1 - a^2}$.

4. To have a large freedom in the design, we used a *racetrack* geometry for our microresonators. This structure is similar to a ring resonator, but it couples to the bus waveguide through a straight section, in a similar way to a directional coupler. From the coupling lengths L_{cp} calculated in §3.4 and Equation (3.2), we derived the length for critical coupling as

$$L_{crit} = \frac{2L_{cp}}{\pi} \sin^{-1}(k) \tag{3.6}$$

Table 3.2: Critical coupling lengths L_{crit}, as calculated for different waveguide widths and loaded quality factors Q_l.

Waveguide width (nm)	$Q_l = \frac{Q_0}{2}$	Attenuation coefficient in the ring α (cm^{-1})	Critical coupling length L_{crit} (μm)
900	10^4	6	42
	10^5	6×10^{-1}	14
	10^6	6×10^{-2}	4.3
	10^7	6×10^{-3}	1.4
1000	10^4	6	54
	10^5	6×10^{-1}	17
	10^6	6×10^{-2}	5.5
	10^7	6×10^{-3}	1.7

In Table 3.2 we report the values calculated for the length of the coupling region, in order to achieve critical coupling with racetrack resonators of different quality factors (radius $R = 100\,\mu m$ and group index $n_g = 1.64$). Without a certain expectation of the Q value, we decided to add to the design of the test structures also several racetracks, with coupling lengths in the range from 0 to 64 μm.

As explained in §3.1, one of the appealing properties of the SiON is that its refractive index can be changed with its composition. Higher refractive indexes allow for higher confinement and, in turn, for shorter bend radii. Thus, we decided to analyze and to test also a high refractive index SiON composition, with $n = 1.8$. Even if the width of the waveguides and the gap in the couplers is fixed by the mask design, we could still deposit a different thickness of the SiON layer. Thus, we analyzed the influence of the layer thickness on the surface FOM as defined in Equation (1.37). With a FEM solver, we simulated rings with width $w = 1\,\mu m$ and radius $R = 100\,\mu m$, while sweeping the ring thickness. We simulated core refractive indexes of both 1.8 and 1.66, for comparison. The refractive index in the top cladding is 1.33, assuming a sensor immersed in water, while the refractive index of the substrate is 1.45, corresponding to the silica.

As motivated in §1.2.2, our FEM analysis neglect the coupling with the bus waveguide, so that the structure under investigation actually represents a ring resonator, rather than a racetrack. However, the mode field profiles in the bends are the same for both structures,

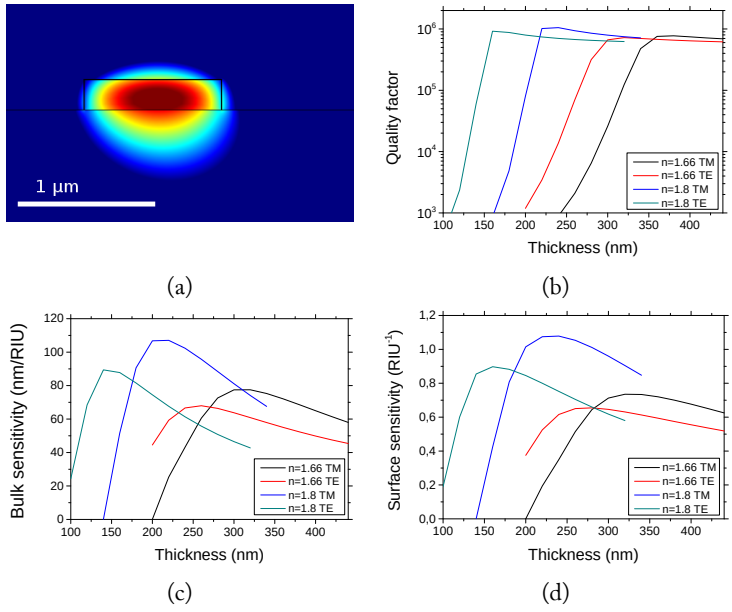

FIGURE 3.8: FEM analysis of the sensing performances of a MRR of width $w = 1\,\mu m$ and radius $R = 100\,\mu m$ as a function of its thickness and refractive index (see §1.2.2 for the method). (a) Electric field energy density in the cross section of a ring resonator. While reducing the thickness, the mode confinement is reduced and the sensitivity is enhanced. As represented in the figure, after a critical level, the mode starts to leak in the substrate reducing the sensitivity in the upper cladding. (b) The quality factor is limited by the index contrast and by the thickness, and it saturates due to material absorption. (c) Bulk sensitivity and (d) surface sensitivity of the MRR. Improved performances are obtained with higher refractive index.

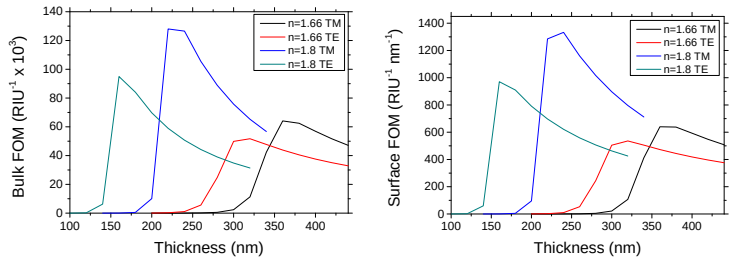

(a) (b)

Figure 3.9: (a) Bulk and (b) surface FOM of a MRR with width $w = 1\,\mu m$ and radius $R = 100\,\mu m$ as a function of its thickness and refractive index. The highest performances are obtained by using the TM mode of a ring in high-index SiON with thickness $t = 240\,nm$.

so that the approximation here introduced can be considered valid, as long as the coupling length is much shorter than the bend radius R. Thus, in the following, we will use the term "rings" to refer to the analysis of the racetracks, always assuming the aforementioned approximation. The results of this analysis are reported in Figure 3.8 and Figure 3.9.

From the simulation plots we can see that rings with high-index SiON ($n = 1.8$) and an optimized thickness ($t = 160 - 180\,nm$), can exhibit a superficial FOM in TE polarization about two times higher than rings with low-index SiON ($n = 1.66$). The improvement comes both from an enhancement of the sensitivity (+45 %) and of the quality factor. The latter has to be confirmed by experimental analysis, because the simulations omitted the contribution of surface scattering losses. It is interesting to notice that the curves in Figure 3.8(c),(d) show a maximum of sensitivity. The reduction of performances at thickness below a critical value is due to the leakage of the mode in the substrate, which has a refractive index higher than water.

For what concerns the low-index SiON composition, from Figure 3.9 we can also deduce that, while the choice of depositing a thickness $t = 300\,nm$ was optimal for the TE-mode sensing, a small increase (+24 %) of the FOM could be obtained by using the TM-mode of a ring with thickness $t = 370\,nm$. The enhancement of TM-modes versus TE-modes is even more pronounced in the case

of the high-index SiON (+35 %). The initial choice of using TE modes, which was mainly dictated by the expected higher quality factor and the shorter radii achievable in waveguide bends, has to be reconsidered in the final version of the optimized sensor. The final choice will need to take in consideration the sensing performances, the losses (mainly scattering losses, which are difficult to predict) and the chip area constraints.

3.6 Fiber coupling

To in- and out-couple the light from our test chip, we usually use lens tapered optical fibers in our experimental setups (see §2.1.1). The coupling procedure, however, can be completed only by technically skilled users and, in addition, it suffers from mechanical stability issues. In the vision of the Symphony project, the final chip has to be easy to be operated, i.e., all the critical parts have to be stably integrated. Presently, LioniX is working on the direct bonding of VCSEL laser sources and Si-photodiodes to create an heterogeneous integrated device. At the same time, FBK is developing a fabrication method to produce Si-photoconductive detectors monolithically integrated in the chip. While all these techniques will not be ready, the only reliable solution is still the use of optical fibers.

To fix firmly the fibers to the chip and allow an efficient light coupling, we also designed on the test chips bonding grooves and tapered mode converters. The first ones are needed to increase the area available for gluing the fiber to the chip and create a mechanically stable bonding. The fabrication procedure usually adopted in FBK's fabs involves the use of *Deep Reactive-Ion Etching* (DRIE) for chip singularization. We decided to use the same techniques to dig high aspect-ratio trenches in the sample. As opposite to V-grooves, typically exploited for fiber arrays, our grooves are basically just vertical, rectangular trenches at least 62.5 µm deep (which correspond to the radius of a typical optical fiber). A sketch of such a structure is depicted in Figure 3.10. We designed several test grooves with widths in the range from 120 to 130 µm and lengths of 250 µm or 500 µm.

The second issue to solve for the fiber coupling, is the mode matching. Light with wavelength 850 nm propagating through a *780-HP*[3]

[3]Specifications from `www.corning.com/WorkArea/downloadasset.aspx?id=30931` and `http://www.thorlabs.com/thorcat/6800/780HP-SpecSheet.pdf`.

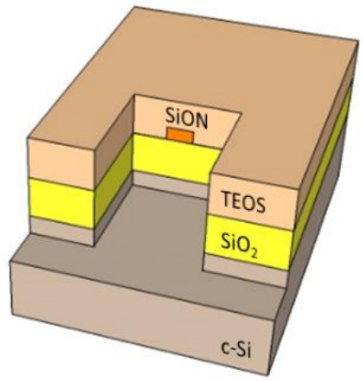

Figure 3.10: Sketch of the high aspect-ratio groove, designed for mechanical stability in fiber bonding.

optical fiber has a low effective refractive index, $n_{eff} = 1.46$, and a quite large MFD of 5.0 µm. Conversely, the light propagating in the waveguide has a high effective refractive index, $n_{eff} = 1.50$, and a small mode diameter, MFD=0.9 µm. To reduce the coupling losses, we designed an inverted taper waveguide, as suggested in [96, 97] and other works.

In an inverted taper waveguide, the MFD is enhanced by reducing the waveguide width. This counter-intuitive behaviour is due to the lower confinement factor that a small waveguide can handle. In Figure 3.11 we show the influence of the waveguide width on the MFD. In particular, Figure 3.11(a) shows how increasing the waveguide width the mode enlarges only in the horizontal direction and becomes very asymmetrical. This asymmetry produces poor overlaps with the mode of the input optical fiber, leading to high insertion losses. Conversely, in Figure 3.11(b),(c) and (d) we show that reducing the waveguide width the mode becomes more circular, and after a critical width the mode field area starts to increase, eventually matching that of the input optical fiber.

Figure 3.11(d) represents a waveguide of width 200 nm, which loosely guides a mode with effective MFD=3.3 µm. FBK's fabs are not equipped for very high resolution photolithography, and from the specifications the minimum feature size is 400 nm. However, smaller tips could be obtained with prolonged etching steps or overexposure

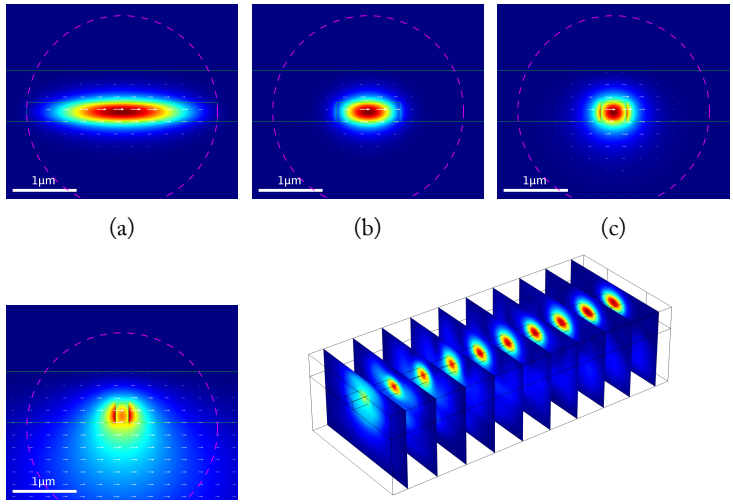

FIGURE 3.11: 2D and 3D simulations of the tapered mode converter. The dashed circle, depicted for reference, has a diameter of 3 µm. (a) By increasing the waveguide width, the mode enlarges only in the horizontal direction and becomes very asymmetrical. (b), (c) and (d) By reducing the waveguide width, the mode becomes more circular, and after a critical width the mode field area starts to increase, eventually matching that of the input optical fiber. (e) Slices of a 3D simulation showing the progressive mode conversion along the tapered waveguide. Only a small fraction is lost in propagation and absorption towards the bottom of the substrate.

during photolithography. For this reason, we decided to try to fabricate tapering with widths $w = 200$ nm and $w = 400$ nm and lengths ranging from 5 to 40 µm. With a full vectorial 3D simulation of a 10 µm long tapering, we estimated coupling losses as low as 1.3 dB for an input MFD=3 µm (typical lens tapered fiber) and 6 dB for an input MFD=5 µm. From Figure 3.11(e) it is possible to appreciate the progressive mode profile conversion along the tapered waveguide. Only a small fraction is lost in propagation and absorption towards the bottom of the substrate.

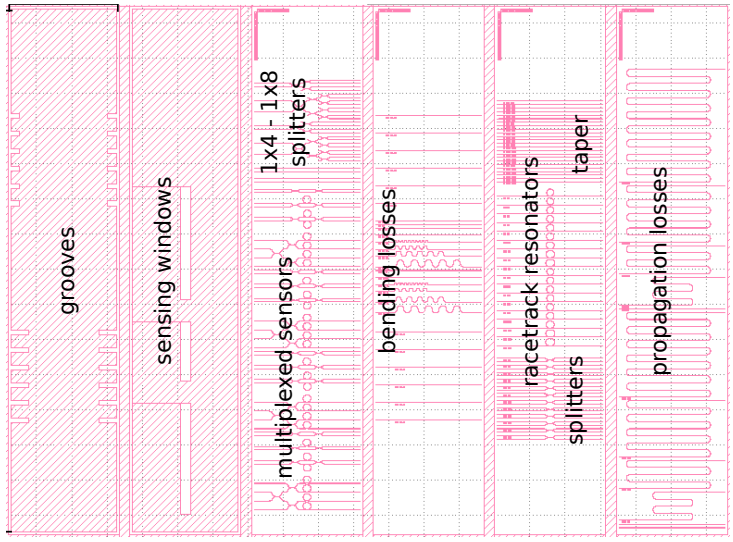

Figure 3.12: Reticle layout for the first batch of test structures (codename *Phobios*).

3.7 Symphony test structures reticle

In conclusion, all the structures presented above have been designed with CAD software on a GDS II file to produce the photolithography reticle. In Figure 3.12 we report the render of the layout of this first batch of test structures (codename *Phobios*).

Experimental results 4

4.1 Chip characterization

This section reports on the characterization of the test structures designed in §3 and of the aMZIs sensors developed by LioniX. Details on the fabrication process for both chips can be found in [91].

The MRR samples have been processed by the FBK's fab in three separate batches. The first runs (samples SM7 and SM8) have suffered from considerable deviation of the cross-section dimensions with respect to the target geometry. In the second fabrication process (samples L2 to L6) several fabrication issues have been partially solved. Moreover, a first attempt to include a detector directly on the chip was started. The last batch (samples BS1 to BS3) is currently being characterized. The summary of the nominal characteristics of the processed samples is reported in Table 4.1.

All the measurements reported in this section has been performed with the apparatus described in §2.1.3.3.

4.1.1 Propagation and bending losses

Propagation and bending losses have been measured on dedicated test structures (see Figure 3.12). For what concerns the first ones, waveguides with nominally equal cross-sections but different lengths

Table 4.1: Nominal characteristics of samples processed by FBK.

Sample name	SiON refractive index	Expected thickness (nm)
SM7	1.66	295
SM8	1.66	300
L2	1.66	349
L3	1.66	374
L4	1.66	298
L5	1.80	216
L6	1.80	256
BS1	1.66	300
BS2	1.66	330
BS3	1.66	375

(from 5 to 30 mm) have been measured. The intensity at the output of the waveguides has been plotted in semi-log scale, and we calculate the attenuation constant (in dB/cm) from the slope of the linear fit of the data.

In a similar fashion, to calculate the bending losses of the samples, we measured waveguides with multiple curves of different radii (from 5 to 100 µm), and compared the intensities at their output with the one of a single waveguide of same length without any curve.

First batch

In the first batch of test samples we measured very high propagations losses: 1.8(4) dB/cm and 2.3(3) dB/cm, respectively for the waveguides of width 1000 nm and 900 nm on sample SM8, and 5.2(7) dB/cm for waveguides of width 1000 nm on sample SM7.

Concerning the bending losses, we unexpectedly found high losses even for bend radius $R = 100$ µm. We measured 0.17(5) dB/90°bend and 0.30(5) dB/90°bend, respectively for waveguides of width 1000 nm and 900 nm on sample SM8. The losses were too high to be measured on sample SM7.

All these high losses led us to conclude that the fabrication process created erroneous waveguide dimensions. The error could have arise either for a wrong estimation of the thickness of the deposited SiON layer or for a wrong waveguide width definition, caused by a prolonged etching process. These conclusions has been later sup-

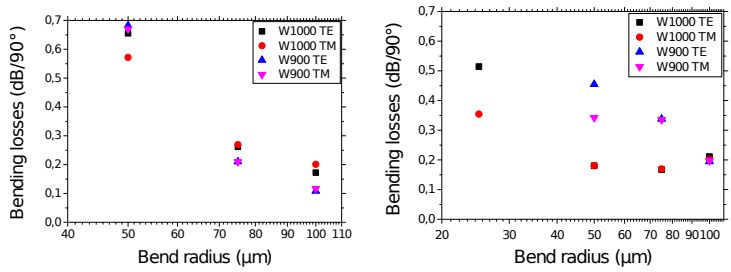

(a) (b)

FIGURE 4.1: Bending losses per 90° curve, measured in both polarizations on the 1000 nm and 900 nm width waveguides of samples (a) L2 and (b) L5.

ported by SEM inspection of the samples, as reported in §4.1.4.

Second batch

The second batch of test samples was fabricated with two SiON refractive indexes, with a fabrication process that reconsidered and partially solved the issues of the first batch.

For what concerns the low-index SiON samples, L2, the best results have been obtained on the 1000 nm width waveguides. We measured propagation losses of 0.9(1) dB/cm and 1.0(2) dB/cm, respectively for TE and TM polarizations. The 900 nm width waveguides experienced higher propagations losses, around 2.7 dB/cm, for both polarizations. Concerning the bending losses, for a bend radius $R = 100\,\mu m$ we measured 0.17 dB/90°bend and 0.1 dB/90°bend for waveguide widths of 1000 nm and 900 nm, respectively. The higher value measured for the wider waveguide is surprising, and we think it could have been biased by inhomogeneities in the coupling losses. For shorter radii the bending losses increased significantly. The data reported in Figure 4.1 indicate that the radius of the ring resonators should be larger than 100 µm.

Also in the case of high-index SiON samples, L5, the best results have been obtained on the 1000 nm width waveguides. Here, the propagations losses were measured as 0.6(2) dB/cm and 0.7(1) dB/cm, respectively for TE and TM polarizations. For the 900 nm width waveguides, the propagations losses rose up to 2 dB/cm in both po-

larizations. Concerning the bending losses, we consistently measured values below 0.2 dB/90°bend for radii varying from 100 to 50 μm for 1000 nm width waveguides. This is qualitatively consistent with our predictions in Figure 3.7, and indicates that the high-index SiON could allow smaller ring resonators with equivalent losses. Concerning the 900 nm width waveguide, losses start from 0.2 dB/90°bend for $R = 100\,\mu m$ and rapidly increase for shorter radii.

For the samples of this second batch, we registered propagation losses below 1 dB/cm, which is one of the targets of the Symphony project. However, the bending losses still remain quite high and, according to Equation (1.27), even the lowest observed value, which is $0.1\,\text{dB/90°bend} = 1.47\,\text{cm}^{-1}$, will limit the quality factor to a maximum value of $\approx 8 \times 10^4$. As it will be shown in §4.1.3, the highest unloaded quality factor for MRRs of this batch is actually 1×10^5, meaning that, even if slightly overestimated in this analysis, the bending losses are still the main limiting factor for the quality factor. Thus, the need for better performing curves is a major concern for the improvements of the sensor performances.

4.1.2 Splitters

The characterization of the $50/50$ splitters was aimed at finding the most suitable coupling length for the directional couplers on which are based.

The analysis that has been conducted on the test structures with varying coupling lengths permitted the validation of the Equation (3.2) and the calculation of the optimal coupling length. In this case the procedure was very simple: with reference to Figure 3.3(a), we injected the light on one arm (waveguide A) and measured the optical power at the output of the same waveguide (Input A/Output A) and of the second waveguide (Input A/ Output B).

In addition, we also performed an analysis on the 1×4 and 1×8 splitters. In this case, by measuring the power at the output of all the waveguides and solving the multivariate system which relates the measurements to the coupling coefficients, we could calculate the statistical variability (due to fabrication) of the coupling coefficients on many splitters with nominally identical features.

First batch

The measurements performed on sample SM8 of the first batch are

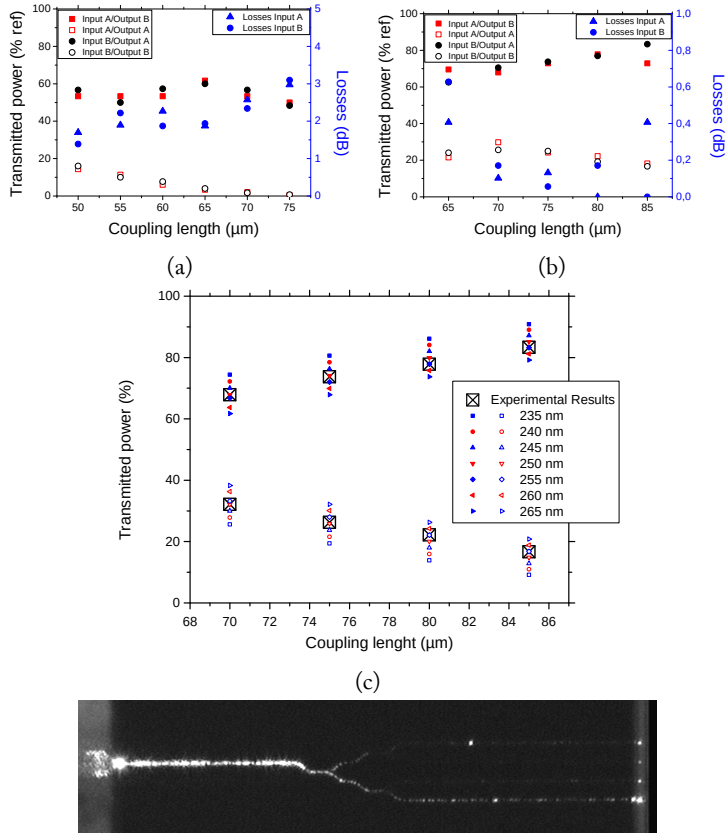

FIGURE 4.2: (a,b) Analysis of the coupling ratio of the splitters on sample SM8, for waveguide width (a) 900 nm and (b) 1000 nm. (c) Comparison of the experimental data for waveguide width 1000 nm with predicted values for waveguides of various thickness. A good matching is obtained for $t = 250 \sim 255$ nm. (d) Top-view microscope picture obtained on a 1×4 splitter with 900 nm width waveguides. The losses and the unbalanced output are visibly marked.

reported in Figure 4.2. We see that the directional couplers with width of 1000 nm are overcoupled at all the available coupling lengths. This unwanted behaviour gives additional insight in the problems already manifested in §4.1.1. In particular we interpreted the higher coupling coefficient as a clue of a waveguide thickness thinner than expected. To corroborate such hypothesis, we performed several simulations to calculate the expected coupling coefficient for directional couplers of thickness smaller than 300 nm. From the results reported in Figure 4.2(c), we found a very good matching between the experimental and simulated data for $250 \sim 255$ nm thick waveguides. The interesting point is that this thickness has been later confirmed by SEM analysis.

Concerning the 900 nm width directional couplers, we observed similar overcoupling regime with, in addition, elevated losses (between 1.5 dB and 3 dB), probably due to the bends used to route the light to and from the splitters. A qualitative picture which highlights these effects is reported in Figure 4.2(d).

Second batch

The improvements in the fabrication process of the second batch were manifested during the analysis of the splitters. In this case, since the mask design was optimized for the low-index SiON, we expected good results for that samples and an undercoupling regime (due to the higher confinement) for samples with higher index. The complete characterization for 1000 nm width directional couplers is summarized in Figure 4.3.

The results are both encouraging and surprising. We can make three observations:

1. the splitters of at least two low-index samples reach a balanced output for coupling lengths close to the length L_{50} calculated in §3.4;

2. the coupling ratio increases only partially when changing the polarization from TE to TM, while it should have a more pronounced effect;

3. the sample L5 is only slightly undercoupled in TE, while according to the simulations it should be much more confined and undercoupled.

Drawing accurate conclusions is not simple: the fact that the sample with the best expected thickness (L4) is actually overcoupled and that the two thicker samples (L2 and L3) are balanced, led us to conclude that either the thickness is overestimated or the gap is smaller than designed. Also the partial insensitivity to the polarization is an indication that the geometry may be different from the expected one. For better understanding the issues, FBK has performed a series of SEM analysis, which are briefly reported in §4.1.4.

Similar results have been obtained also with 900 nm width waveguides. Here we tested the 1×4 and the 1×8 splitters, with respectively 3 and 7 cascaded directional couplers. The pictures in Figure 4.3(c) and (d) are top-view microscope images of these structures, illuminated with TE-polarized light. The average value for the coupling ratio is 46(4) % for sample L2, which means an almost perfect 50/50 splitting, and 39(8) % for sample L5. Thus, the reproducibility of the fabrication process is higher for samples with low-index SiON.

4.1.3 Ring resonators

The ring resonator is, of course, the heart of the biosensor designed by the UniTN-FBK team. We spent a lot of time for their characterization, both from the point of view of the optical and sensing properties. The optical properties of interest are the quality factor Q and the extinction ratio ER of the WGM resonances. The sensing properties that we have measured are the bulk sensitivity S_b, the bulk figure of merit FOM_b and the bulk limit of detection LOD_b. The other sensing properties of interest, i.e., the surface sensitivity S_s, the surface figure of merit FOM_s and the surface limit of detection LOD_s, unfortunately, are not easy to be measured without surface functionalization. Thus, we will omit these properties from the characterization of the structures, but we will try to estimate such values from the biosensing measurements reported in §4.2.2.

First batch

As we saw in the previous sections, the first batch suffered from severe bending and propagation losses. This fact is reflected also in the poor quality observed in the resonators. We measured both resonators covered by *Tetraethyl orthosilicate* (TEOS) cladding and resonators exposed to ambient (where the top cladding has been etched away).

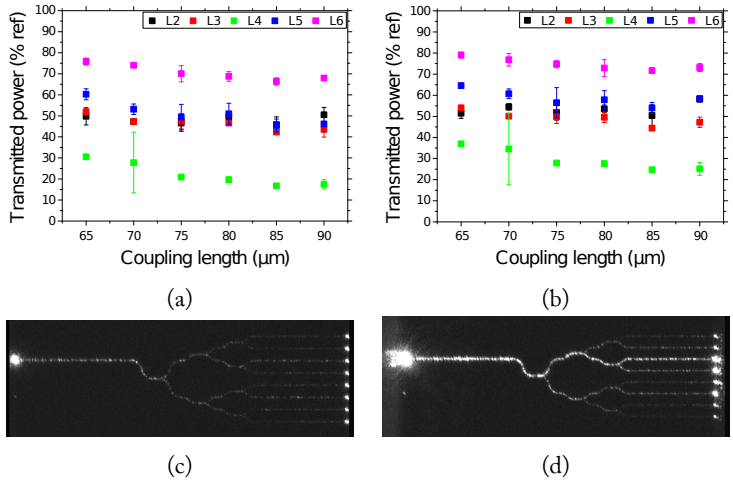

Figure 4.3: Output A/Input A ratio for 1000 nm width directional couplers of different lengths, in (a) TE and (b) TM polarizations. Samples L2, L3 and L5 are balanced for one coupling length in the given range. Top-view microscope pictures for the 1×8 splitters of samples (c) L2 and (d) L5 in TE polarization. The first shows balanced light intensities at the output, while the latter is evidently in undercoupling regime.

Concerning the covered structures with width 900 nm, the maximum quality factor reached $Q \sim 9 \times 10^3$ in near-critical coupling (ER ~ -7 dB) and TE polarization, but only half of this value for TM polarization. For what concerns the covered 1000 nm width rings, the quality factor rises to $Q \sim 18 \times 10^3$ for both TE and TM polarizations. However, in this case the visibility of the resonances is reduced, with an ER $\gtrsim -1$ dB, which greatly influences the precision of the resonance position measurements.

These results are even worst in the case of uncovered resonators. In all the samples that we tested, the light suffered from very high losses at the sensing window edges, where the waveguides cross the interface between etched silica and air or water. Figure 4.4 shows one typical example of these structures. We clearly notice that the signal, already low for the high bending losses, is completely lost when it reaches the sensing area. The effect is disruptive for measurements

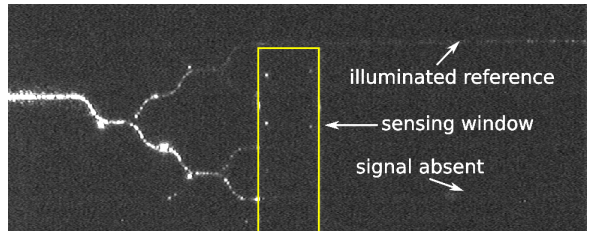

FIGURE 4.4: 1×4 exposed multiplexed sensor of sample SM8. The light experiences huge scattering losses at the silica/air or silica/water interface, preventing any sensing measurement.

both in water and in air, preventing any sensing measurement.

The reflectivity R given by the mismatch of effective index at the interface from the cladded region ($n_{eff,1} = 1.51$) to the sensing region ($n_{eff,2} = 1.49$, when filled with water) can be calculated using the Fresnel equation at normal incidence angle:

$$R = \left| \frac{n_{eff,1} - n_{eff,2}}{n_{eff,1} + n_{eff,2}} \right|^2 \tag{4.1}$$

We find $R = 4 \times 10^{-5}$, which is negligible and can not explain the observed losses. As we will show in §4.1.4, the losses at this interface are evidence of another fabrication issue related to the wet-etching process involved in the opening of the sensing windows. During the etching, in fact, the exposed waveguides have been tapered, reaching a final width of only $w \sim 530\,\text{nm}$. This issue has been faced and solved in the second fabrication batch.

Second batch

For the characterization of the MRRs of the second batch, we focused on the two samples that showed the best performances in terms of losses and coupling ratio, i.e., samples L2 and L5. The characterization of covered sensors for both samples is reported in Figure 4.5. Concerning L2, we notice that the length to achieve critical coupling is $\sim 15\,\mu\text{m}$ for both TE and TM polarizations and for both waveguide widths. On the contrary, in the case of sample L5 we measured a critical coupling length of $\lesssim 15\,\mu\text{m}$ for the TM polarization and sensibly longer ($\sim 40 - 50\,\mu\text{m}$) in the case of TE polarization. The lower polarization dependence of the sample L2 could be explained

by erroneous waveguide cross-section dimensions. The SEM analysis presented in §4.1.4 will confirm that both the thickness and width of these waveguides were actually wrong, yielding in an almost square cross-section and, thus, reducing the birefringence.

We noticed usually higher Q values for TE than for TM, which is in contrast with the simulations of Figure 3.8. We should remember that in all the analysis of §3.5 we neglected the contribution of surface losses (scattering and absorption). Thus, from the measured values it appears that surface losses are the main limiting factor for the quality factors of the resonators. This is especially evident in the case of TM polarization, because the WGM modes are less confined and are more affected by the surface characteristics of the resonator. The second observation is that the measured Q values are higher for the wider waveguide widths (1000 nm). This is reasonable, as the mode confinement is higher in the wider waveguides. However, to select the best sensors, we should first compare this values with the sensitivities of the resonators, as the compromise between mode confinement and quality factor will ultimately lead the choice.

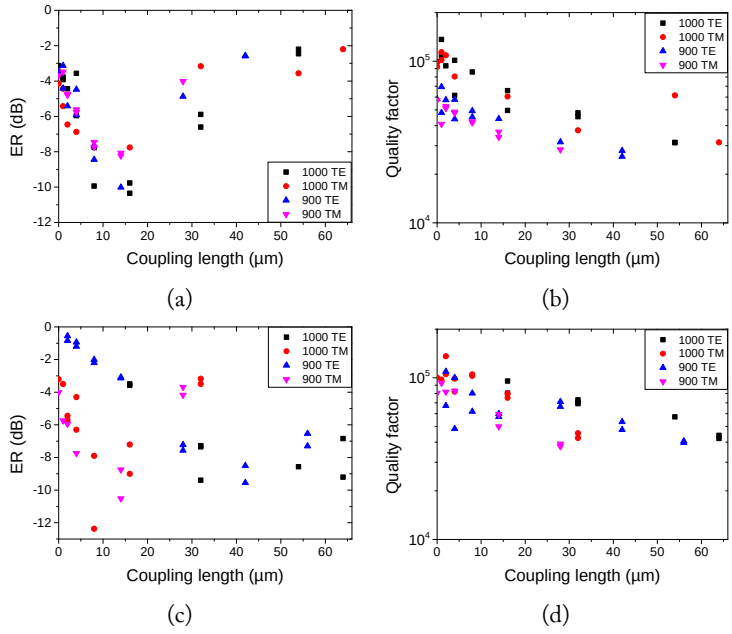

FIGURE 4.5: (a,c) Extinction ratio ER and (b,d) quality factor Q for ring resonators embedded in silica with varying coupling lengths. (a, b) Resonators from sample L2. (c, d) Resonators from sample L5.

In Figure 4.6 we report the characterization of sensors with etched silica cladding, exposed to de-ionized *MilliQ* water. Thus, in this case the refractive index of the cladding is 1.33, instead of the previous 1.45. The number of tested devices is reduced, because not all the resonators have been exposed (so that not all the coupling lengths were available). Therefore, it is not possible to accurately determine the intrinsic quality factor Q_0 and the critical coupling lengths L_{crit}, as done for the covered resonators. We noticed large extinction ratio (ER $= -18$ dB) in the case of sample L2 at long coupling lengths, but only limited loaded quality factor ($Q \lesssim 3 \times 10^4$). Conversely, on sample L5 we couldn't achieve critical coupling in the available range, with a minimum extinction ratio of only -6 dB. However, in this case the highest loaded quality factor has been $Q \sim 4 \times 10^4$. Strangely, for sample L5 the quality factor did not seem to be affected

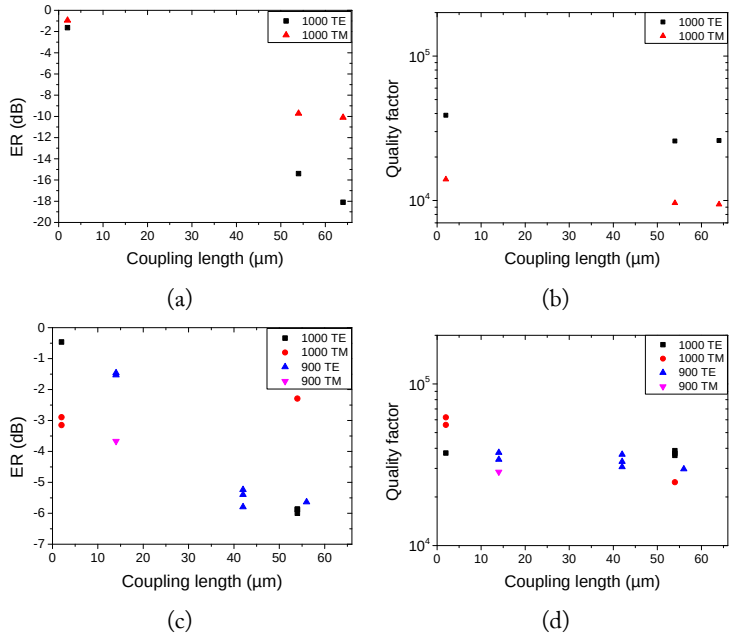

Figure 4.6: (a,c) Extinction ratio ER and (b,d) quality factor Q for ring resonators with varying coupling lengths. The upper cladding has been opened to expose the resonator to the analyte (*MilliQ* water, in this case). (a, b) Resonators from sample L2. (c, d) Resonators from sample L5.

by the coupling strength.

Both samples experienced a general enhancement of losses of $2 \sim 3$ times, when exposed to water. This fact can not be explained just by taking into account the absorption losses of water, that are $\alpha = 0.04\,\mathrm{cm}^{-1}$ [98] at the operating wavelength of 850 nm. It can not be explained even with the different refractive index contrast, that actually increases and should produce opposite behaviour. This means that the reduction in the quality factor happened during the etching process, which is necessary for the opening of the sensing window. The etching can either have introduced more superficial roughness, and hence have increased the superficial losses, or have altered the geometry of the waveguides, increasing the radiative losses.

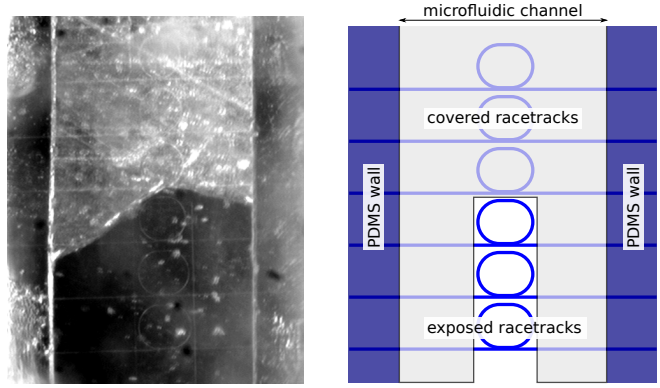

FIGURE 4.7: Optical microscope picture and schematic description, showing the transit of water (from bottom to top) in the PDMS microchannel, above few exposed MRRs sensors.

Even if the issues in the opening of the sensing window have been partially solved, in comparison with the results of the first batch, the process of this step has still to be improved.

As a conclusion to the characterization of the "statical" optical properties, i.e. Q and ER, Table 4.2 summarizes the important data obtained on the MRRs of this second production batch.

To measure the sensitivity of the sensors on samples L2 and L5, we used the same technique described at page 40. We prepared five solutions of glucose in water, with concentrations ranging from 0.0 % to 0.4 %w/w, equivalent to a maximum refractive index variation of 5.2×10^{-4} RIU. We used the microfluidic system described in §2.2.2 and §2.2.3.1 to inject at constant flow rate the solutions in a flux of pure (de-ionized) water. The transit of water above the MRRs is shown in Figure 4.7. During the injections, the transmission spectra of the resonators have been continuously measured by scanning the wavelength of the VCSEL source. The resonance positions were calculated by fitting a portion of the spectra with a Lorentzian function, and their time evolution was recorded with a sampling rate of at least 2 Hz. More details on the acquisition algorithm are reported in §B.

Table 4.2: Summary of the resonance's characteristics for samples L2 and L5. The resonators covered by the silica cladding are indicated as "cover", while the exposed sensor are called "open". The intrinsic quality factor is measured by extrapolating the measured (loaded) quality factors to a coupling length of 0 µm.

Sample name	Polarization	Waveguide width (nm)	Critical coupling length (µm)	Minimum ER (dB)	Intrinsic quality factor ($\times 10^4$)
L2 - cover	TE	900	15(5)	−10.0(5)	6(1)
	TE	1000	15(5)	−10.0(5)	12(2)
	TM	900	15(5)	−8.5(5)	5(1)
	TM	1000	15(5)	−8.0(5)	11(1)
L5 - cover	TE	900	42(5)	−9.0(5)	10.5(10)
	TE	1000	∼50(10)	−9(1)	13(1)
	TM	900	14(5)	−10(1)	9(1)
	TM	1000	12(4)	−10(1)	13(2)
L2 - open	TE	1000	60(5)	−18•	5•°
	TM	1000	60(5)	−10•	1.9•°
L5 - open	TE	900	∼50(10)	−5.8(5)	7(1)°
	TE	1000	∼50•	−6.0(5)	7(1)°
	TM	1000	-	-	6.0(5)

• too few datapoints to estimate an uncertainty value.
° calculated as twice the loaded quality factor at critical coupling.

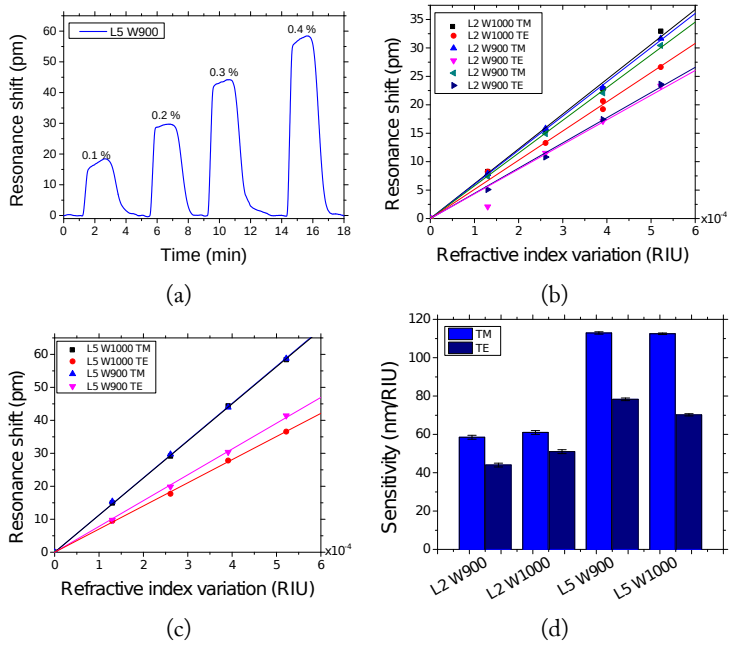

FIGURE 4.8: Bulk sensitivity measurements on samples L2 and L5. The variation in refractive index is obtained by injections of water-glucose solutions at different concentrations. (a) A typical example of the temporal evolution of the resonance wavelength upon subsequent injections of solutions at different concentrations. (b) Measured resonance wavelength shifts for varying polarizations and resonator widths on sample L2. We report the repeated measurements on two 900 nm width resonators to show the good reproducibility of the results. The error bars are smaller than the datapoints. (c) Same for sample L5. (d) Summary of the sensitivities of the two samples, as measured from the linear fits in plots (b) and (c). In all these measurements, the coupling length of the racetrack resonators of sample L2 was 64 µm, while it was 54 µm in the case of sample L5.

One example of a typical recorded signal is shown in Figure 4.8(a). The trace clearly shows red-shifts in the resonance wavelength upon injection of the solutions. The linear relation between the magnitude of these shifts and the variation in refractive index is reported in the plots of Figure 4.8(b),(c). Thus, the calculation of the bulk sensitivity

is simply obtained by the slope of the linear fit on the data. The plot summarizing all the measured bulk sensitivities S_b on samples L2 and L5 is reported in Figure 4.8(d). As expected, we can notice that the TM polarization always gives higher sensitivities with respect to TE polarization. In addition, the sensors on the sample with the highest refractive index contrast, L5, show overall better performances compared to the sensors on sample L2. On the contrary, the differences produced by the waveguides widths are less significant. The highest measured bulk sensitivity has been S_b =113(1) nm/RIU.

The comparison between the measured values and the simulated one, Figure 3.8(c), shows excellent agreement for the sample L5 (refractive index $n_{\mathrm{SiON}} = 1.8$ and thickness $t = 216$ nm). For what concerns the sample L2 (refractive index $n_{\mathrm{SiON}} = 1.66$ and expected thickness $t = 350$ nm), we see that the simulation overestimates the bulk sensitivity by about $10-15$ %. The reason has been found in the wrong estimation of the SiON thickness. During the fabrication process, in fact, the SiON layer is annealed at 1050 °C for 1.5 h. This annealing removes the hydrogen bonds present in the material and reduces the propagation losses. At the same time, however, the material should shrink by a factor up to 15 %, and for this reason the deposited layer has to be thicker to compensate the effect (i.e., 410 nm deposited to achieve a final thickness of 350 nm after the annealing). While, for the high-index SiON, we get a predictable shrinkage ratios of $8-10$ %, in accordance to previously measured values, the same did not apply for the low-index SiON. As we will see in §4.1.4, in fact, sample L3 (same low-index composition of L2) showed negligible shrinkage during the annealing. Therefore, it is reasonable to expect that also for L2 the final thickness equals the deposited one, i.e., $t = 410$ nm. If we compare the measured bulk sensitivity with the simulations of Figure 3.8(c) for this value of thickness, we find an agreement within 5 %. The FEM analysis proved to be a reliable technique for the prediction of the S_b values.

Finally, in order to characterize the bulk LOD of all the structures under test, we measured the uncertainty of repeated resonance wavelength estimations during continuous flow of blank solution (*MilliQ* water without glucose). Figure 4.9(a) shows few typical traces in a time scale of ten minutes: we can distinguish quite large fluctuations with a time scale $\tau \gtrsim 2$ min and smaller fluctuations with time scale $\tau \lesssim 2$ min. Since the resonance shift, during an injection, evolves with time scales shorter than 2 min (see Figure 4.8(a) for compari-

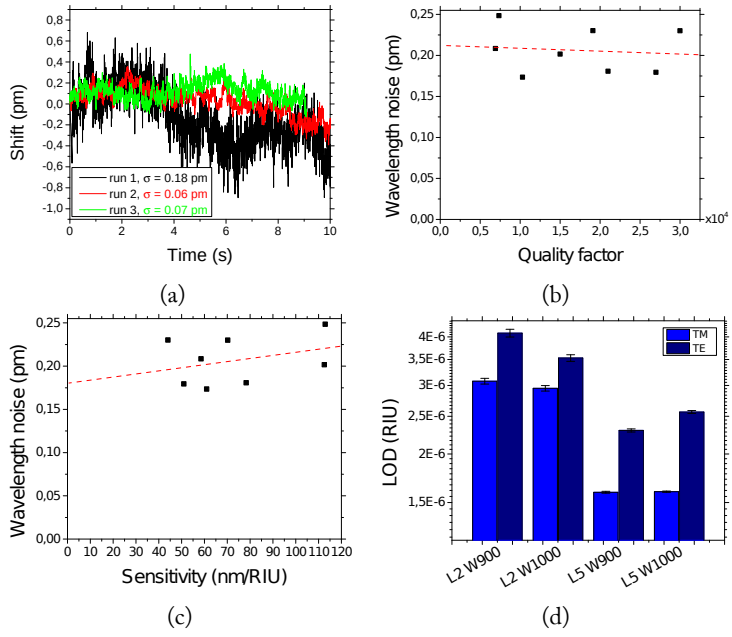

FIGURE 4.9: (b),(c) Demonstration of the weak dependence of the measured wavelength noise to the quality factor Q and bulk sensitivity S_b of several MRR sensors. (a) Comparison of the wavelength noise during continuous flow of blank solution with the old (black line) and new (green and red) wavelength estimation method. (d) Bulk LOD_b measured for the different sensors on samples L2 and L5. All the devices shows LOD_b in the range from 1.6×10^{-6} to 4×10^{-6} RIU.

son), we decided to use as wavelength uncertainty the standard deviation of the trace in a time-window $\overline{\tau} = 2$ min. The black line, in particular, has been recorded with the first version of the acquisition setup, which was not optimized. In this case, we found a wavelength uncertainty of $\sigma = 0.18(2)$ pm. With the same setup we also characterized all the devices under test (from samples L2 ad L5). In order to gain informations about the source of this noise, we compared the measured uncertainties as a function of the quality factor Q and bulk sensitivity S_b of the resonators. The result of these comparisons are

reported in Figure 4.9(b),(c). As expected, the uncertainty decreases with increasing quality factor and increases with increasing sensitivity. However, none of the two properties has strong influence on the wavelength noise, as it can be seen by the small slope of the linear fits in the plots.

From this analysis we can conclude that the limiting factor to the measurement uncertainties is nor the fitting procedure (which depends on Q) and neither the fluctuations in temperature or refractive index of the fluid, at least on this time scale $\overline{\tau}$. Thus, we deduced that the uncertainty in wavelength should have been originated from the VCSEL source (through the injection of electrical noise in the driving current) or from our method to estimate the wavelength (which was based on a direct reading of the current during the VCSEL tuning). By modifying the procedure to estimate the laser wavelength during the scan, we reduced the noise amount by about three times, as demonstrated in the green and red curves of Figure 4.9(a). The differences in tha acquisition algorithm are explained in §B. With this smaller uncertainty, $\sigma \approx 0.06(1)$ pm, and Equation (1.12) we calculated the bulk limit of detection, LOD_b, obtaining the plot of Figure 4.9(d). The best value is $\mathrm{LOD}_b = 1.6(3) \times 10^{-6}$ RIU, obtained with TM polarized light on the 1 μm wide rings of sample L5 (higher refractive index contrast device), while sample L2 shows a worse but still comparable $\mathrm{LOD}_b = 3.0(5) \times 10^{-6}$ RIU.

In conclusion, the efforts for the design and realization of a sensitive and multiplexed device reached good results during this second fabrication batch. We demonstrated reliable directional couplers, with which 1×4 and 1×8 light splitters have been realized. The MRRs sensors proved to be highly sensitive, with LOD values comparable to the state of the art of similar structures. In addition, as we will show in §4.2.2, these devices have been successfully used to detect aflatoxins in buffer solutions down to nanomolar concentrations. The room for improvements, mainly for what concerns the optimization of the deposited thickness and the etching of the sensing window, lead us to hope that even lower amount of analyte could be detected.

Third batch

The decision to start a third production batch was mainly driven by the need to converge all the technology developed so far in one final optimized prototype of the sensor. In the design of this device we

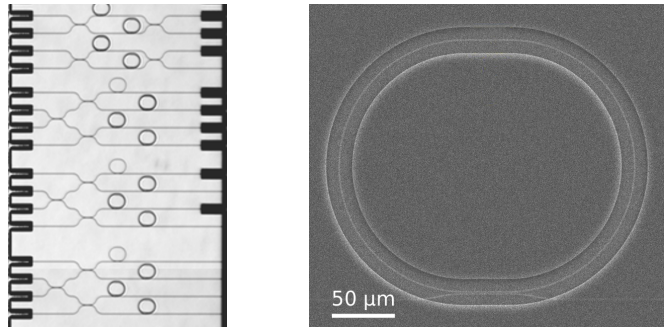

(a) (b)

FIGURE 4.10: (a) Top-view microscope image of the 1×4 multiplexed sensor prototype. Grooves are etched at the inputs and outputs to allow stable bonding of fibers. (b) SEM image of the opening window around the MRR

joined:

- fiber grooves with dimensions 135 µm $\times$ 300 µm, for stable bonding of fibers;
- 1×4 splitters, which proved equal splitting in sample L2;
- 1000 nm width racetrack resonators with coupling length 35 µm, with the intention to achieve a slight undercoupling regime in water ambient;
- smaller opening windows, localized just around the sensors, to reduce the amount of removed cladding and to better protect the ring during the functionalization procedure.

Moreover, since the FBK unit is developing an integrated photodetector, the design was planned to implement some of these receivers at the output of the sensors (unfortunately, at the time of writing, the development of this unit is not ready yet). In Figure 4.10 we report the top-view microscope picture and a close-up SEM picture of the newly fabricated devices.

Since the issues with the control of the deposition thickness were still not completely solved, FBK decided to fabricate in this batch

three wafers with different SiON nominal thickness (300, 330 and 375 nm) and refractive index $n_{\mathrm{SiON}} = 1.66$. A new batch with the higher-contrast refractive index is planned.

The results on these samples are still very preliminary. However, we can anticipate that the improved design led to the fabrication of critically coupled MRRs, with an excellent loaded quality factor $Q > 1.3 \times 10^5$ in liquid ambient. This result is more than four times better with respect to what measured on sample L2. At the same time, the bulk sensitivity is still high, with $S_b \sim 70$ nm/RIU in TE polarization and $S_b \sim 80$ nm/RIU in TM polarization. We think that, if these value will be confirmed, and if we will be able to reduce the uncertainty of the resonance wavelength estimation down to the limit posed by the resonance linewidth, we will reach LOD values down to $\approx 6 \times 10^{-7}$ RIU.

4.1.4 SEM analysis

The characterization of the first two fabrication batches evidenced anomalies between the expected and the measured performances of the devices. The analysis conducted on several samples revealed some information about the causes of these differences, but to gain deeper insight in the process we needed SEM inspection of the samples. All the SEM pictures here reported have been acquired by Alina Samusenko and Mher Ghulinyan at the FBK facilities. With this analysis, we could highlight two main fabrication issues: the proper definition of the waveguide cross-section and the careful opening of the sensing window.

Waveguide definition issues

Usually, in an experienced silicon fab, the definition of waveguides with accurate dimensions is not a problem. However, the FBK's fab recently upgraded most of its machines to the production of 6″ wafers, making most of the old fabrication recipes unreliable.

The first issue came from the shrinkage of the SiON material after the annealing process. The first production batch, during which we were not aware of the problem, produced samples with SiON layers thinner than designed, with $t \sim 250$ nm (SEM image not available). During the two subsequent batches the process has been adjusted, approaching to an almost correct thickness, as shown in Figure 4.11(a) and (b).

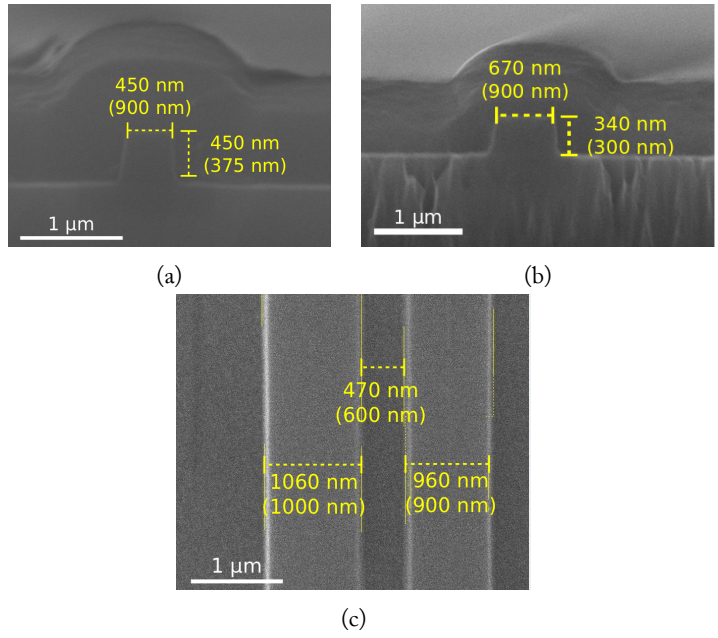

FIGURE 4.11: Cross-section pictures of samples (a) L3 (second batch) and (b) BS1 (third batch) showing the issues in the correct waveguide definition (expected values are reported in parentheses). The waveguides are covered by TEOS cladding. (c) Top-view picture of waveguides of the third batch before the cladding deposition. The width errors are reduced to 6 %.

The second issue, which concerns the width of the waveguides, was due to a wrong calibration of the exposure of the photolithography stepper. Also in this case, we can see that the issue has been faced and finally solved almost completely. In Figure 4.11(c), the waveguides of the last batch are inspected before the deposition of the TEOS cladding, and appear just 60 nm larger than expected.

Sensing window opening issues

The need to open a window in the silica cladding over the sensors require an etching step. In particular, during this process the waveguide should not be affected. During the fabrication of the first batch we

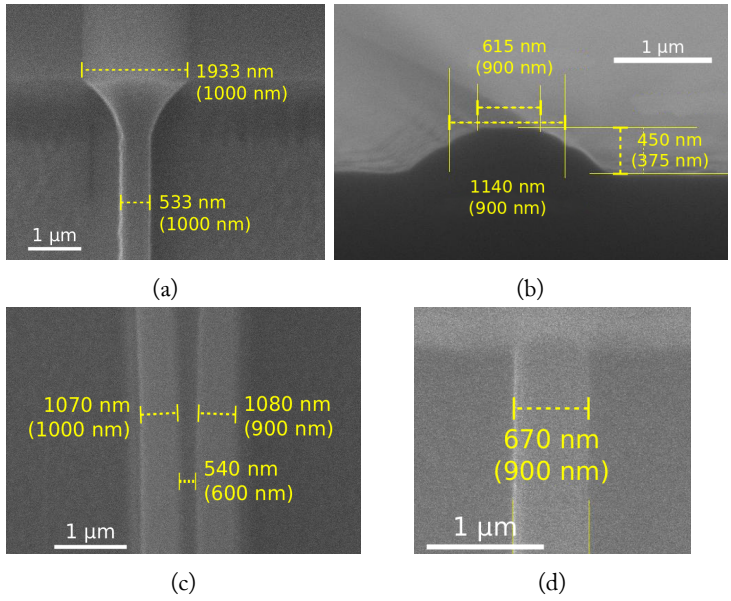

Figure 4.12: (a) Narrowing of the waveguide width on sample SM8 due to the wet BHF process of the first batch. (b),(c) Silica shoulders remained on the edges of the waveguides on sample L3 during the second production batch. (d) A longer BHF treatment completely removed the silica shoulders on sample BS1 of the third batch.

opted for a wet etching, which heavily thinned the exposed waveguides, as shown in Figure 4.12(a). In the next two fabrication batches, we chose an initial RIE etching, followed by a final wet BHF step. In Figure 4.12(b),(c), we notice that an incorrect etching, performed during the second production batch, leaved silica shoulders at the edges of the waveguide. In the third production batch, a longer wet etch completely removed these shoulders, even if at the cost of a narrowing in the waveguide width (Figure 4.12(d)).

Finally, we conclude by showing in Figure 4.13 the SEM picture of a groove etched during the first DRIE test. In this case, the etching has been exaggerated on purpose to show the high aspect-ratio that can be achieved with this technique. We clearly see that the width of the opening is preserved throughout the profile. The final grooves,

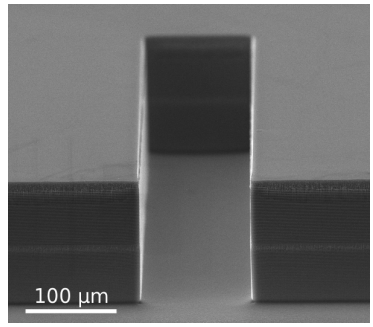

FIGURE 4.13: DRIE etched test groove. The high aspect ratio of the trench is exaggerated in this test. The final grooves will be 63 µm deep.

however, will be only 63 µm deep.

4.1.5 Asymmetric Mach-Zehnder

We conclude this section about the optical characterization of the Symphony's photonic sensor chips with the samples designed and fabricated by our partner team LioniX. They developed three different aMZIs, with sensing arm length $L_s \simeq 3$, 5 and 9 cm. The reference arm, which is covered by a silica cladding, has a length calculated to produce a FSR of 0.1 nm in the transmission spectra (see Equation (1.43)). The calculated nominal parameters are reported in Table 4.3. Figure 4.14 shows the layout of the shortest and longest sensors. The light coupling is achieved through a fiber array unit with six single-mode fibers, enabling the simultaneous interrogation of both sensing devices available on every chip.

On these chips we could not characterize the propagation and bending losses of the waveguides, as in the layout there were no dedicated structures. However, from the total insertion losses on the longest interferometer ($\sim$ 9 cm), we can definitely conclude that propagation losses are below 1 dB/cm (LioniX measured 0.2 dB/cm in preliminary tests). The bending losses are negligible, as the light is detected after passing through more than 120 90° curves. Similarly, we did not observed detectable losses in the Y-splitter structures.

A typical transmission spectrum of an aMZI is shown in Fig-

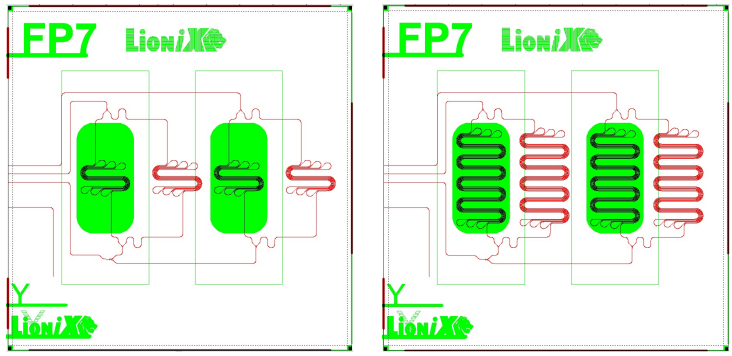

(a) (b)

Figure 4.14: Overlaid mask layout of the aMZIs chips, showing the shortest and longest interferometers. The green areas are opening in the cladding to expose the sensor arm to the ambient. The light coupling is achieved on the left side of the chip by using a fiber array.

ure 4.15(a). After normalization, the data can be fitted using a sinusoidal function, as shown from the theoretical analysis in §1.3.1, Equation (1.43). The frequency of the fitted sine corresponds to the FSR of the interferometric fringes, while the phase ϕ gives informations about the relative optical path length in the two sensing arms. During the sensing experiments, the phase ϕ changes in response to the variations of refractive index according to Equation (1.44), and a bulk sensitivity S_b can be defined as for the MRRs sensors with Equation (1.45).

Similarly to what done for the characterization of the MRRs, to measure the bulk sensitivity, S_b, of the aMZIs we exposed them to

Table 4.3: Computed nominal characteristics of aMZI samples designed by LioniX.

Sensing arm length (µm)	Covered arm length (µm)	FSR (nm)	Sensitivity (nm/RIU)
28 941	32 797	0.1	768
49 740	53 422	0.1	1320
91 339	94 675	0.1	2425

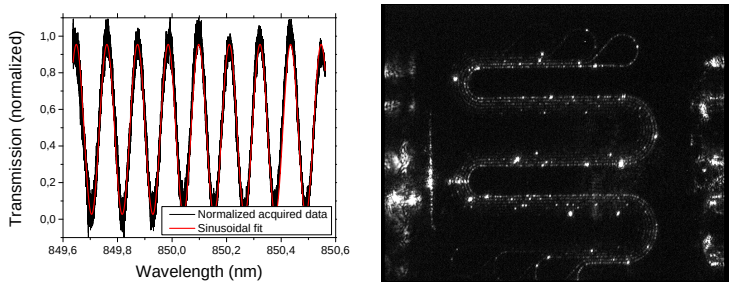

(a) (b)

FIGURE 4.15: (a) Typical transmission spectrum (normalized data) of an aMZI sensor, and corresponding sinusoidal fit. (b) Top-view microscope picture of light scattered from an aMZI sensor.

several water-glucose solutions. In this case, we used the microfluidic of Epigem (see §2.2.3.2), specifically designed by LioniX to fit their samples. The drawback of this microfluidic is that the sensing chamber is big, with a volume of 10 µl and a cross section of 1.6 mm^2. Thus, the flow rate used for these measurement is necessarily high (15 $\mu l\,min^{-1}$), in order to reach a stable signal in a reasonably short time during the injections. We observed significant drifts in the baseline during the measurements. These have been removed by interpolating the offset recorded during the flow of the reference (blank) solution. The measured phase shift curves and the comparison of the bulk sensitivities are reported in Figure 4.16.

From the analysis of these data, we calculated a bulk sensitivity S_b =44.2(5) $\times$ 10^3 rad/RIU and S_b =77.5(5) $\times$ 10^3 rad/RIU, respectively for the short and medium length aMZIs. We can convert these phase sensitivities in wavelength sensitivities by using the following relation

$$S(\text{nm/RIU}) = \frac{\text{FSR(nm)}}{2\pi} S(\text{rad/RIU}) \tag{4.2}$$

With a measured FSR$\simeq$0.11 nm, we obtained S_b =780(10) nm/RIU and S_b =1360(10) nm/RIU, respectively for the short and medium length aMZIs. The experimental sensitivities agree with the simulated values within 3 %.

We conclude the characterization of the aMZIs sensors by evaluating their bulk LOD. Following the guidelines of the MRRs anal-

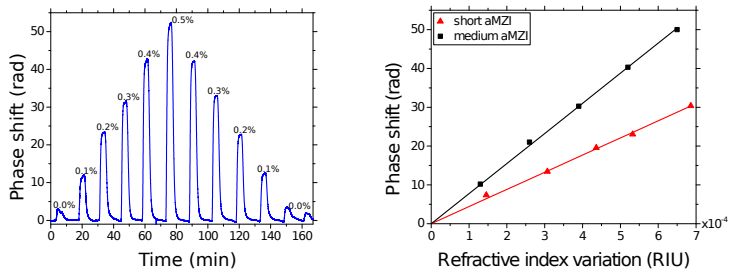

(a) (b)

Figure 4.16: (a) Phase shift curves obtained with a medium length aMZI during the injection of the water-glucose solutions (glucose concentration in %w/w labelled on the plot). The baseline drift has been removed from the data. (b) Evaluation and comparison of the bulk sensitivity S_b on the medium and short length aMZIs.

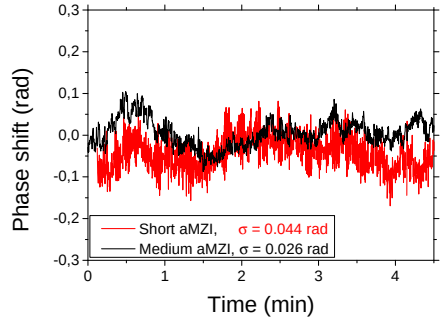

Figure 4.17: Typical temporal evolution of the measured phase shift during continuous flow of reference solution, for two aMZIs of different length.

ysis, we chose as typical time scale the value $\overline{\tau} = 2\,\text{min}$. In this time window, we calculated the standard deviation of the phase shift curves for the short and medium lengths sensors, respectively $\sigma = 0.044\,\text{rad}$ and $\sigma = 0.026\,\text{rad}$, as can be seen from Figure 4.17. From these values, we obtained $\text{LOD}_b = 3 \times 10^{-6}\,\text{RIU}$ and $\text{LOD}_b = 1 \times 10^{-6}\,\text{RIU}$, for the short and medium length aMZIs.

A final comment on the limit of detection analysis: for both

MRRs and aMZIs, and especially for the latter, the value of the LOD is heavily influenced by the choice of the time interval $\overline{\tau}$ and, to some extent, also from the position of this temporal window along a "flat" signal. The value of the LOD, thus, makes sense only if referenced to a specific $\overline{\tau}$, which, in our case, was chosen to be $\overline{\tau} = 2$ min. The choice was dictated by the duration of the transient phases during injections. With different flow rates or different microfluidics, the value for $\overline{\tau}$ has to be reconsidered, and the LOD accordingly.

In conclusion, both the MRRs and the aMZIs proved to be ultrasensitive sensors in compliance with the technical specification imposed by the project Symphony, at least for what concerns the bulk sensing. The higher flexibility and design control offered by the aMZI is counterbalanced by the need for a larger sensing area, while the appeal of the MRR's compactness is obfuscated by the lower fabrication tolerance. At this stage of the project it is very difficult to decide for a preferred platform. Thus, the most important and critical parameter to demonstrate and measure is the specific bio-recognition of the target molecules and its achievable LOD. The next sections will cover the preliminary measurements on this regard.

4.1.6 State of the art

To asses the quality of our devices, in this section we compare the measured characteristics of our sensor to the ones of similar devices. For what concerns the bulk sensitivity of the MRRs sensors, we observed values between 60 nm/RIU and 110 nm/RIU, depending on the material of the core and on the polarization. In particular, the highest sensitivity has been obtained with the higher refractive index SiON composition ($n = 1.8$).

This dependence to the core material can also be noticed in similar reported WGM resonators. For a ring of a relatively low index polymer ($n \approx 1.6$) and small radius ($R = 45$ µm), the measured bulk sensitivity is $S_b = 65$ nm/RIU [8], whereas a small ring in silicon-on-insulator (SOI), with $n = 3.43$, can offer bulk sensitivities up to $S_b = 163$ nm/RIU [99]. However, the sensitivity also depends on geometrical factors, and in particular on the confinement factor, as explained thoroughly in §1.2.2. By adopting ultra-thin SOI microrings (thickness of 90 nm instead of the usual 220 nm), in [100], the authors could enhance the sensitivity by more than three times, from

38 to 133 nm/RIU, even if at the expenses of a lower quality factor, $Q = 24 \times 10^3$.

Thus, from the point of view of the sensitivity, our devices are perfectly in line with the status of the art on microrings. However, other WGM structures can be investigated. By developing disk resonators with horizontal air slots, and exploiting the well known field enhancement in the slot region, in [101] the authors demonstrated a sensitivity enhancement up to $S_b = 300\,\text{nm/RIU}$. Presently, we are analyzing the feasibility of obtaining a similar structure, by also integrating a vertically coupled bus waveguide. Among other WGM structures we have silica microsphere, which usually shows low sensitivities, due to the low refractive index, and ultra-high quality factors [102]. Conversely, resonators based on ultrathin capillaries can reach values as high as $S_b = 1100\,\text{nm/RIU}$, obtained by exciting higher radial order modes that shows high confinment factors in the fluid [103].

From the point of view of the quality factor, our devices show room for improvements. The propagation losses in straight SiO_xN_y waveguides has been reported to be as low as $0.1\,\text{dB cm}^{-1}$, from which an expected quality factor can be calculated as $Q = 5 \times 10^6$ at wavelengths of 850 nm [104]. The propagation losses that we measured were almost one order of magnitude higher, ranging from 0.6 to $1.0\,\text{dB cm}^{-1}$, from which we would expect a maximum quality factor in the range from 5×10^5 to 9×10^5. The maximum intrinsic measured quality factors, observed in the last production batch, was $Q = 2.3 \times 10^5$. This value is satisfactory, but still not optimal. As a comparison, the highest observed quality factor for a silica wedge microresonator has been $Q = 8.75 \times 10^8$ [67], and the highest quality factor for a microring in Si_3N_4, with radius $R = 100\,\mu\text{m}$, has been $Q = 3.4 \times 10^6$ [105]. SiO_xN_y is an alloy of these two materials, and it is reasonable to expect comparable results, even if implying a linear combination would be too over-simplified. Thus, efforts have to be put in the improvement of the fabrication method, in order to reduce the propagation losses, both of straight waveguide and bent ones.

Another important metric for comparing different structures and technology is the FOM, as anticipated in §1.1.4. The highest FOM_b that we observed has been

$$\text{FOM}_b = \frac{70\,\text{nm/RIU} \times 1.3 \times 10^5}{850\,\text{nm}} \approx 11 \times 10^3\,\text{/RIU} \qquad (4.3)$$

which outperform the small SOI disks of [55] ($FOM_b = 2 \times 10^3$ /RIU and the photonic crystal cavity of [57] ($FOM_b = 8 \times 10^3$ /RIU). Our FOM is even higher than the one of the commercial apparatus *Maverick*, from *Genalyte*, that is based on the structures of [99], with a $FOM_b = 4.5 \times 10^3$ /RIU. As an example of the impact of different metrics, we report the case of the plasmonic gold mushrooms arrays. These structures are based on localized surface plasmon resonances (LSPR), and exhibit extremely high sensitivities, up to $Sb = 1000$ nm/RIU. However, the quality factor of their resonances is very low, $Q \approx 100$, and the final FOM is reported as $FOM_b = 108$ /RIU, which is also the theoretical upper limit for SPR-based sensors [56]. Thus, from this example we immediately see that it is very important to adopt the right metric, in order to not be misled in the comparison.

Unfortunately, still nowadays many groups omit to report either the quality factor or the sensitivity in their manuscripts, so that it is not always possible to calculate the FOM. In such cases the comparison is based on the LOD, which is biased by the noise in the readout system and, for this reason, not completely fair. The LOD of our sensors (1.6×10^{-6} RIU for the MRR and 1×10^{-6} RIU for the aMZI) compares reasonably well with many devices reported in literature. SOI microrings usually perform in the range between 10^{-5} RIU [106] and 7×10^{-7} RIU [99]. Mach-Zehnder interferometers also performs in the order of 10^{-6}-10^{-7} RIU [39, 107], and similar is the case of SPR devices [26]. Even combining SPR with magneto-optical materials, the LOD still remains in the order of 5×10^{-6} RIU [108]. Outliers from this list are the silica microspheres, that thanks to the high quality factors can achieve outstanding $FOM_b = 150 \times 10^3$ /RIU and $LOD_b = 3 \times 10^{-7}$ RIU [102], the liquid-core capillary-based WGMs, that by excitation of higher order modes can reach LOD_b as low as 2.8×10^{-7} RIU (and $FOM_b = 70 \times 10^3$ /RIU) [109], and the resonance-splitting-sensing in silica microtoroids, that is able to distinguish (in air) single particle with diameters down to 30 nm [36]. Unfortunately, none of these methods are easily integrable in a sensor-chip.

To summarize, Table 4.4 lists the values reported in this comparison. Overall, we can conclude that the sensors that we developed can be ranked among the state-of-the-art of the competing technologies. They are densely integrated in optical chips (on the contrary of microspheres- or microcapillary-based sensors) and show high perfor-

Table 4.4: Comparison of the sensing performances of state-of-the-art refractometric sensors.

Technique	Bulk sensitivity (nm/RIU)	Quality factor	FOM_b (/RIU)	LOD_b (RIU)	Reference
Polymer ring	65	2×10^4	8.4×10^2	5×10^{-5}	[8]
SOI ring	163	4.3×10^4	4.5×10^3	7×10^{-7}	[99]
SOI disk	21	1.3×10^5	2×10^3	-	[55]
Silica microsphere	30	5×10^6	1.5×10^5	3×10^{-7}	[102]
Microcapillary	570	1.2×10^5	7×10^4	3×10^{-7}	[109]
Slot microdisk	300	3.4×10^4	6.6×10^3	-	[101]
PhC cavity	330	3.3×10^4	8×10^3	10^{-5}	[57]
Plasmonic gold mushroom	1000	1×10^2	1×10^2	10^{-5}	[56]
MZI				10^{-6}-10^{-7}	[39, 107]
SPR				10^{-6}-10^{-7}	[26]
MRR L5	110	3×10^4	4×10^3	1.6×10^{-6}	present work
MRR BS3	70	1.3×10^5	1.1×10^4	-	present work
aMZI	1360	1.55×10^4 •	2.5×10^4	1×10^{-6}	present work

• Calculated using FSR/2 as the FWHM.

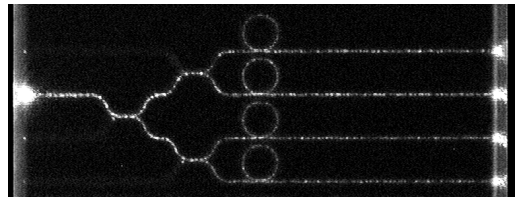

FIGURE 4.18: Microscope picture of a 1×4 multiplexed sensor of sample L2. The light is equally split and it couples simultaneously to all the four resonators. Reading more than one sensor at the same time can improve the reliability of the measurements. Moreover, the aspecific contributions given by thermal fluctuations or by bulk refractive index variations can be suppressed with the use of one reference ring, yielding in a lower limit of detection.

mances, both in terms of FOM and LOD. Still, further improvements can be applied, both from the point of view of fabrication and of the readout system. In particular, one of the next activities will be the investigation of the multiplexed sensing capabilities of our devices, as for the sensor shown in Figure 4.18. With the simultaneous reading of more than one resonator, in fact, we expect to improve the reliability of the measurements. Moreover, the aspecific contributions given by thermal fluctuations or by bulk refractive index variations (during label-free sensing) can be suppressed with the use of one reference ring, yielding in a lower limit of detection.

4.2 Biosensing with Aflatoxin-M1

This section summarizes the most important results achieved in the field of biosensing experiments during the project Symphony.

The objectives in this regard were multiple:

- develop a reliable sensing protocol;
- select a suitable functionalization procedure;
- evaluate and compare the sensing properties of MRRs and aMZIs;
- test the sensitivity of the sensors to several noise contributions (temperature fluctuations, flow rate, fat/particles content);

- evaluate the limits of the biosensing, in terms of selectivity, limit of detection, detection range, re-usability of the chips.

For the moment we mainly focused on the first three objectives, but also some aspects of the other ones have been faced.

For the experiments of this section we collaborate with our colleagues of the LaBSSAH group of FBK. They provided the consumable materials and performed the functionalization on the sensor' surface (more details in §A). The optical setup was the same as described in §2.1.3.3, while the sample delivery system is described in §2.2.2. The target analyte was the aflatoxin AFM1.

4.2.1 Biosensing with the aMZI

The specific biorecognition of the DNA-aptamers is a delicate biological process that requires a careful control of the physico-chemical properties of the ambient in which this process takes place. In particular, some of the factors that influence the recognition are:

- temperature;
- pH;
- ionic strength.

Except for the temperature, the other parameters can be controlled with a proper buffer solution. However, the choice of this buffer should consider not only the interactions with the aptamers, but also the interactions with the analyte and ultimately with the sensor itself.

The first experiments in this regard were aimed to highlight the effects of few carrier solutions on our aMZIs. Initially, we naively decided to test the use of regenerated skimmed milk powder. If this test had given good results, many of the constraints of the Symphony's team in charge of the filtering of the milk sample would have been relaxed. Needless to say, this test was a complete failure, with huge aspecific drifts and complete coverage of the sensor' surface due to milk content (probably proteins). Under the microscope the formed layer appeared compact and whitish. Thus, we moved to the testing of four different buffer compositions:

- *Phosphate Buffered Solution* (PBS), which is a widely used buffer. In [110], this buffer composition was used for an immunoassay of Aflatoxin-M1, with an antibody-based functionalization;

- *Tris(hydroxymethyl)aminomethane* (Tris)-HCl, which is the buffer suggested from the company selling the aptamers (NeoVentures[1]). We tested the composition with and without $MgCl_2$, with the aim of lowering the content of salts and bulk shift;
- *2-(N-morpholino)ethanesulfonic acid* (MES), for its closer pH value in comparison to that of milk.

Details on the buffers composition are reported in §A.2. This experiment was particularly designed to check if these buffers could contribute to give aspecific signals.

We prepared the experiment by exposing a medium-length aMZI to a continuous flow of *MilliQ* water, with a flow rate of 5 µl min^{-1}. We started the acquisition of the spectra and waited for the stabilization of the phase signal. From this reference we injected the four buffers, one at a time, and recorded the evolution of the phase ϕ. The obtained curves are plotted in Figure 4.19(a). We can notice that the four buffers produce different bulk shifts, as expected from the different concentrations and contents. More important, however, is that the two Tris-HCl buffers did not reach a steady (flat) condition within 8 minutes from the injection. We measured the slope of the curves in the range between minute 3 and 6, obtaining -0.33, 1.35, 1.02 and 0.30 rad/min, respectively for PBS, Tris-HCl, Tris-HCl-$MgCl_2$ and MES.

As explained in §1.1.2, and in particular in Equation (1.5), one possible way to estimate the concentration of the analyte solution is to measure and compare the initial slope of the sensorgram. For this reason, it is important to reduce to the minimum the background drift produced by the carrier solution (buffer). Based on this consideration, we selected the MES buffer as the first choice for the biosensing experiment.

Inspecting the curves of Figure 4.19(a), we notice that the time to reach a stable signal after an injection takes at least 3 min, which is comparable to the expected timescale of the biosensing binding. This is mainly due to the big volume of the sensing chamber, which in the case of the aMZIs developed by LioniX is fixed to 10 µl per sensing site. To alleviate the problem and reduce the uncertainty in the initial-slope measurement, we repeated the injection of PBS plugs while varying the flow rate. As shown in Figure 4.19(b), we found

[1] Company website `http://neoventures.ca/`.

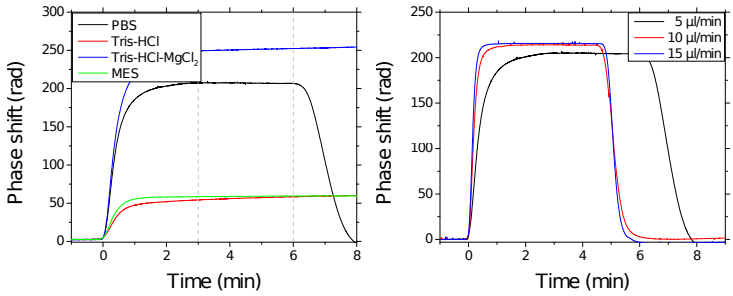

(a) (b)

Figure 4.19: (a) Comparison of the signals obtained by injecting different buffer solutions on a medium-length aMZI. The initial (reference) liquid is *MilliQ* water, at flow rate 5 µl min^{-1}. The slope is evaluated between minutes 3 and 6. (b) Comparison of the stabilization time after the injections of PBS buffers at different flow rates.

that at 15 µl min^{-1} the signal could be considered stable after only 1 min, which is a reasonable compromise for our purposes. Faster rates could shorten this time even more, but will consume more analyte during the sensing experiments. Thus, we decided to use a flow rate of 15 µl min^{-1} in the following experiments with this microfluidic.

The next experiments were aimed at assessing the sensing properties of the aMZI with regard to the specific recognition of AFM1. To this regard, the sensor has been functionalized with amminoterminated anti-Aflatoxin M1 DNA-aptamers, through the wet silanization procedure described in §A. In this experiments, the carrier solution was MES buffer (at the chosen flow rate of 15 µl min^{-1}), in which we injected plugs of AFM1 solutions in *Dimethyl Sulfoxide* (DMSO) and MES. The reason for the use of DMSO is that the toxin is insoluble in water (and thus in the buffer). Therefore, AFM1 is diluted, upon purchase, in DMSO and saved in stock solutions of 12 µM concentration. From the stock, the toxin is then diluted in MES to reach the desired concentration. The content of DMSO in the final solution is thus proportional to the content of AFM1, and complicates the interpretation of the sensorgrams by adding an aspecific bulk-refractive-index signal during the injection/incubation of the analyte.

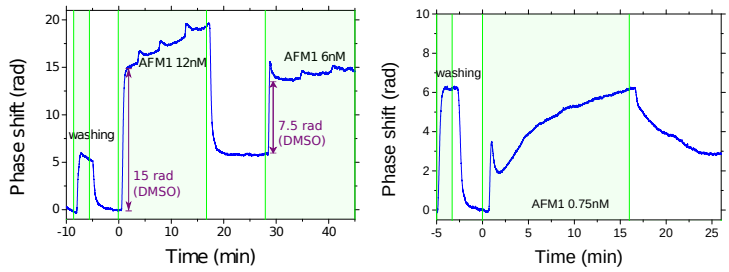

(a) (b)

FIGURE 4.20: Sensorgrams obtained by exposing a functionalized medium-length aMZI to AFM1 solutions of concentrations (a) 12 nM and 6 nM and (b) 0.75 nM. The injection valve is actuated within the shadowed regions. Before the injection of the toxin samples, we rinsed the injection tubes with clean buffer. In (a) the microfluidic pump produced overpressure spikes, probably because of clogging at the sample inlet.

In Figure 4.20 we report the sensorgrams obtained by exposing a functionalized medium-length aMZI to several toxin samples at different concentrations. Here we can distinguish some artefacts, important to understand the following measurements:

1. the injection valve is actuated within the shadowed regions, but the signal is delayed because of the finite volume between the valve and the sensor;
2. samples with higher concentrations produce higher step-like jumps, which are related to the bulk refractive index change produced by the DMSO content;
3. the flow of buffer or the injection of washing buffer produces no or little drifts in time, meaning that the aspecific signal is low;
4. the injection of target toxin produces signals with significant drifts in time and a residual shift which remains even after the injection.

In addition, in Figure 4.20(a) we notice few spikes during the two analyte injections. Since normally these spikes are not present, we

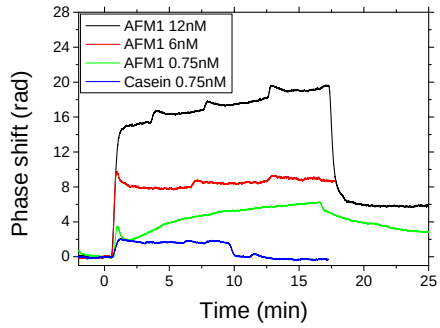

Figure 4.21: Direct comparison of the sensorgrams obtained with the injections of AFM1 solutions, respectively at 12, 6 and 0.75 nM concentration, and with the injection of casein at 0.75 nM.

believe that they were produced by the microfluidic pump exercising overpressure to compensate for clogging at the sample inlet.

To better appreciate the discussed effects, we report in Figure 4.21 four overlaid sensorgrams obtained on a medium-length aMZI. In this case, we also show the curve obtained during the injection of casein at 0.75 nM concentration. As expected, while in the case of AFM1 we observe drifts of signal in time, these drifts are not present during the injection of the casein proteins. However, we can also notice that the slope of the sensorgrams are not proportional to the concentration of toxin. This is due to a limited reproducibility of the measurements that will be discussed later.

Surprised by the significant drift observed during the injection of AFM1 at 0.75 nM concentration, we investigated the specific limit of detection, LOD_{AFM1}, by reducing the amount of toxin content. This time, we prepared a functionalized short-length aMZI and injected solutions at 0.75, 0.37 and 0.19 nM concentration. As shown in Figure 4.22, even at these low concentrations the signal still increases visibly during the incubation of the analyte. We measured slopes of 0.51, 0.21 and 0.17 rad/min, respectively for the three concentrations. Also in this case, the issues in the reproducibility of the surface preparation (regeneration protocol or repeated functionalization processes on the same sample) leads to the impossibility of the concentration estimation. However, an important point that we wanted to highlight with this plot is the exceptionally low concentration that is

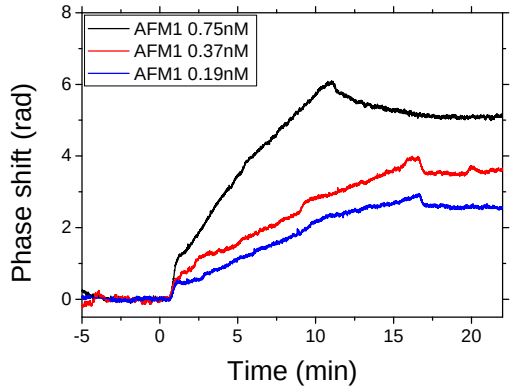

FIGURE 4.22: Sensorgrams acquired with low-concentrated AFM1 on a short-length aMZI.

qualitatively detectable with our setup: 0.19 nM of AFM1 is equivalent to a concentration of 62 ppt, which is very close to limit imposed by the EU regulation. If this result could be confirmed and reproduced reliably, the constraints on the pre-concentration unit will be solved almost completely.

After these first experiments, we could not observe clear signals at such low concentrations any more. We deduced that the repeated cleaning and re-functionalization processes, forced by the low number of available chips, could have affected the composition of the sensor' surface, hence preventing a good and reliable coverage with aptamers. To contain this reduction of sensitivity, we need to limit the number of re-functionalization processes. This is possible if an effective regeneration procedure is found. To optimize the sensing protocol, we started the investigation of the regeneration of the surface. We repeated the injection of AFM1 solutions at 20 nM concentration, trying to regenerate the sensor with either MES buffer or with the injection of a solution of sodium acetate (composition summarized in §A.3). What we observed in Figure 4.23 is a good reproducibility in the bulk shift, but a poor reproducibility of the slope during the toxin incubation. We could not notice any improvement after regeneration of the surface with Na-acetate, in comparison to the effect of the buffer alone.

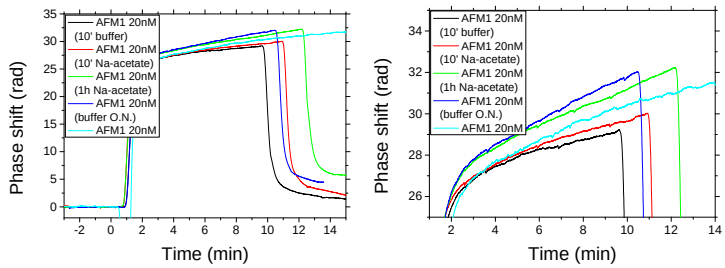

Figure 4.23: (a) Full-range and (b) zoomed sensorgrams of repeated AFM1 injections, interposed with injections of buffer or sodium acetate as regenerating solutions.

From these results, we can also quantify the reproducibility of the sensorgrams, and hence the uncertainty in the estimation of the concentration, by looking at the distribution of the observed slopes during AFM1 incubation. The average slope is 0.37 rad/min, with a standard deviation of 0.12 rad/min. With this values, estimating the concentration from a single measurement will result in relative errors of more than 30 %.

We conclude this overview on the reproducibility of AFM1 biorecognition on aMZIs sensor by showing the results of a tentative calibration experiment. We injected toxins at concentration from 10 to 80 nM. The obtained curves, reported in Figure 4.24, clearly show the negative result of such approach. While the bulk shift reproduces the DMSO content reliably, the slopes of the sensorgrams during the incubations are not proportional to the concentrations of AFM1. The issues on the reproducibility of the specific label-free sensing have been faced, and mostly solved, during the investigation on the MRRs sensors.

4.2.2 Biosensing with the MRRs

After the demonstrated "proof-of-principle" detection of aflatoxin with the aMZIs, we started to investigate if the same could be replicated also with our developed MRRs sensors. Similarly to what done in the first case, the chips have been functionalized with anti-aflatoxin DNA-aptamers, and the assay has been performed in a con-

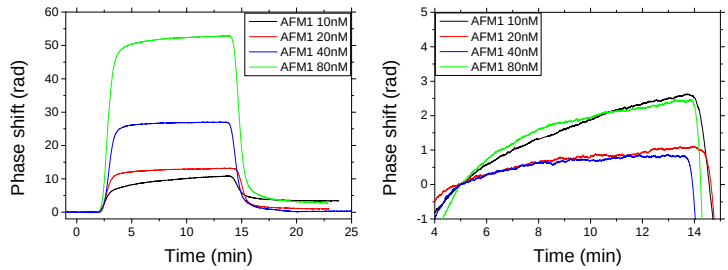

FIGURE 4.24: Sensorgrams obtained with a medium-length aMZI exposed to increasing toxin concentrations. (a) Full-range sensorgrams. (b) Zoomed view on the incubation part of the sensorgrams. The shifts due to the bulk content of DMSO has been subtracted for better comparison.

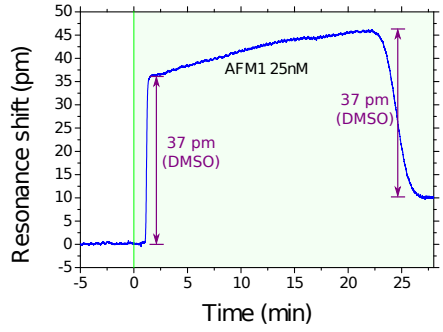

FIGURE 4.25: Sensorgram obtained on a MRR sensor of sample L2. The injected AFM1 concentration was 25 nM.

tinuous flow of 50 mM MES buffer at pH 6.6. In this case, however, we could use the microfluidic flow-cell of §2.2.3.1, that we specifically developed to reduce to the minimum the volume of the incubation chamber. As a result, we could keep a reduced flow rate of 3 $\mu l\,min^{-1}$ to obtain the same rise time upon injection of analyte samples.

In Figure 4.25 we report the first observation of AFM1 specific detection using a MRR sensor from sample L2 (core refractive in-

dex $n_{\mathrm{SiON}} = 1.66$) of the second production batch. The sensorgram signal was flat during the initial rinsing with buffer. After the injection of target solution at 25 nM concentration, the sensor firstly exhibited a step-like jump due to the DMSO content, and then it showed a linear grow due to the specific binding. We can notice that the residual signal after the injection ($\Delta\lambda = 10\,\mathrm{pm}$) equals the total increment, attributed to the binding of the toxin, registered between minutes 2 and 22. This effect is an evidence of a stable binding on the surface, which is not rinsed with the subsequent flow of buffer solution. This characteristic is especially desired for sensors which are to be operated in a complex sensing liquid, like milk or blood serum or plasma. During the sensing, in fact, the fluid under examination could contain various amount of non specific biomolecules, and the tiny specific signal can be easily masked. In these cases, after the analyte incubation for a fixed amount of time, it is possible to rinse the excess of complex media and perform the measurement of residuals in a controlled buffer.

Another conclusion that can be drawn comparing the recorded curve to the ones calculated in Figure 1.2, is that the sensor was operated far from its saturation. Despite this, repeating the experiment with other AFM1 injections at the same concentration produced lower and lower slopes, corresponding to a reduction of the specific sensitivity. Even trying to regenerate the surface with glycine solution did not restore the original signal level. However, from this experiment we could not distinguish if the reduced specific sensitivity was attributed to an harsh effect of the glycine solution or simply to a poor aptamer functionalization binding strength.

To clarify the issue, we studied the effect of repeated injections of glycine solution by performing similar specific biosensing experiments on sample L5 (higher refractive index, $n_{\mathrm{SiON}} = 1.8$, and bulk sensitivity, S_b =112 nm/RIU). The composition of the regeneration solution is reported in §A.3. In Figure 4.26, in particular, we report the results of a test on the regeneration efficiency. Here, we alternated the injections of toxins with injections of glycine solutions. Our aim was to measure the total number of regenerations that could be achieved without major effects on the capture efficiency.

If we analyse the sensorgram curves obtained during the incubation, reported in Figure 4.26(b), we can notice that the accumulated wavelength shift $\Delta\lambda$ was proportional to the concentration, as expected if the sensor was operated far from saturation, with $\Delta\lambda = 3$

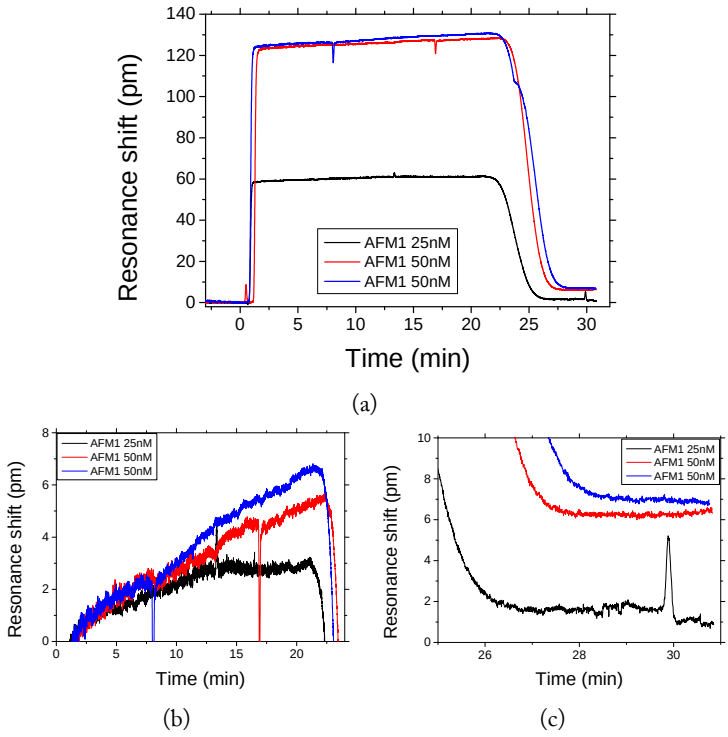

FIGURE 4.26: (a) Sensorgrams obtained on sample L5, with the injection of two different AFM1 concentrations alternated by injections of glycine as regeneration solution. The spikes in the signal are due to pressure irregularities in the microfluidic flow. (b) Sensorgram curves obtained by subtracting the bulk effect due to the presence of DMSO. (c) Close-up of the sensorgrams on the residual shifts after the rinsing of the sensor with buffer.

and $\sim$ 6 pm respectively for concentrations of 25 and 50 nM. In contrast, we can also notice from Figure 4.26(c) that the residual shift after the sensor rinsing with buffer did not reflect the same proportionality: the injection at the lowest concentration did not form a stable binding with the aptamers, with a final residual $\Delta\lambda < 2$ pm. In this sense, the regeneration glycine solution, which followed the first injection of 25 nM AFM1, seems to have improved the binding strength. The two subsequent injections of 50 nM AFM1, in fact, produced a residual shift $\Delta\lambda \sim 6.5$ pm which coincides with the value observed during the incubation. In that case, the sensorgrams seemed to be reasonably reproducible.

To better compare the effects of the regeneration, in another experiment on sample L2 we decided to start the injection sequence with the glycine solution, so as to set a common initial condition for all the successive AFM1 injections. In addition, we decided to repeat the measurement on all the concentrations at least two times and to randomize the injections sequence, in order to avoid systematic errors induced by the progressive damaging of the sensor.

Figure 4.27(a) and (b) show the sensorgrams obtained on sample L2, respectively for TE and TM polarizations. As expected, the bulk shifts were higher in the case of TM polarization, but also the residual shifts and the slopes during the incubations were higher in the case of TM polarized light. This was the first evidence of a confirmation of the FEM simulation results shown in Figure 3.8(d). In previous experiments (not described here) similar comparisons gave controversial results. The main reason was that the small difference in surface sensitivity was masked by larger variations in surface preparation/conditions. The better reproducibility provided by the continuous regeneration with glycine actually increased the resolution of the binding-kinetic measurements, such that the difference in the surface sensitivities can now be appreciated.

Figure 4.27(c) reports the binding curves of Figure 4.27(b) from minute 3 to 21 and after the subtraction of the bulk contribution. Figure 4.27(d) shows a zoomed-view of the residual shifts of the sensorgrams after the rinsing with buffer. In both plots we can appreciate the clear dependence of these signals on the toxin concentration. In addition, the strength of the specific binding formed between analyte and aptamers is such that, even after sensor rinsing, the final level of wavelength shift $\Delta\lambda$ matches the signal increment obtained during the incubation, giving more reliability to the analysis.

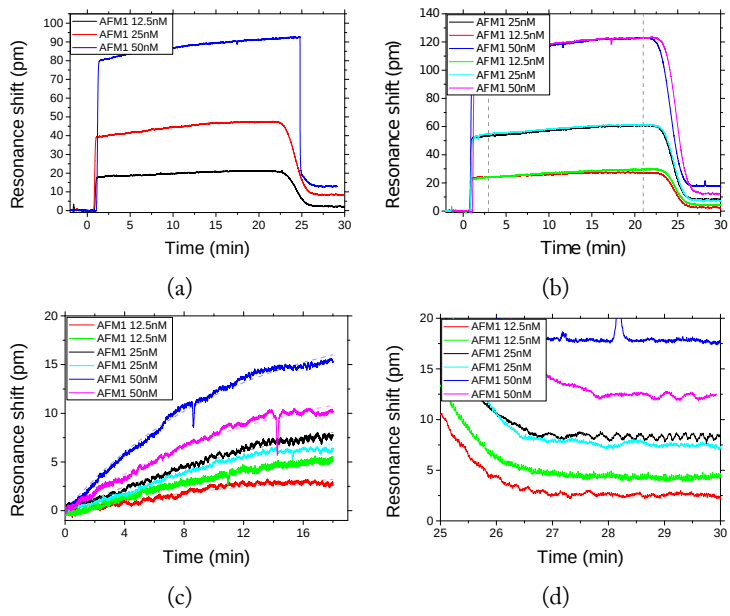

FIGURE 4.27: Sensorgrams recorded on sample L2 with (a) TE and (b) TM polarized light. The dashed lines in (b) mark the time interval for the surface binding analysis exposed in (c). (c) Specific binding sensorgrams after the subtraction of the bulk shift induced by the DMSO content. The dashed curves are exponential fittings for the evaluation of the rate constants and initial slopes. (d) Zoomed view on the residual shifts after the sensor rinsing with buffer.

Another important observation on these measurements is that, even if at high concentration (50 nM) the sensorgrams started to clearly show the effects of the surface saturation, we could use the sensor repeatedly for many injections (9 AFM1 injections and 9 glycine injections). This means that the use of glycine regenerates the surface effectively. One of the objectives of the next measurements will be the assessment of the total number of regenerations cycles that can be performed on the same sensor.

We conclude this section with the estimation of the rate constants of our binding process (1.2), and with the analysis of the specific surface sensitivity S_{AFM1} of samples L2 and L5. The analysis started

with the exponential fitting of the binding curves recorded between minutes 3 and 21 from the beginning of the toxin injections. The fitting function is

$$\Delta\lambda(t) = A\left[1 - \exp\left(-\frac{t}{\tau}\right)\right] \tag{4.4}$$

where t is the time passed since the beginning of the analysed frame, and the parameters that are extracted from the fitting are the saturation level A and the time constant τ. The latter is related to the kinetic rate constants of Equation (1.4), and can be read as

$$\frac{1}{\tau} = k_a \cdot C + k_d \tag{4.5}$$

with C the analyte concentration, and where k_a and k_d are the association and dissociation rate constants, respectively.

To determine the rate constants we plotted the obtained values of τ^{-1} as a function of the injected AFM1 concentration, as reported in Figure 4.28. From the slope and intercept of the linear fit we calculated k_a and k_d. Table 4.5 reports their values, together with the equilibrium dissociation constant, $K_D = k_d/k_a$. The company selling the aptamer (*NeoVentures*) report the value of the dissociation constant as $K_D = 10\,\text{nM}$. The agreement, within the error bars, between the measured and the specified K_D validates this analysis. Unfortunately, the company does not specify the rate constants, so that a direct assessment of their value is not possible. Both the measured association and dissociation rate constants, k_a and k_d, fall into the typical ranges of, respectively, 10^3-$10^7\,\text{M}^{-1}\,\text{s}^{-1}$ and 10^{-1}-$10^{-6}\,\text{s}^{-1}$ [111]. A comparison can be made with a DNA-aptamer developed to detect molecules (anthracyclines) with a molecular weight similar to the one of aflatoxin. [112] measured rate constants of $k_a = 3.3 \times 10^4\,\text{M}^{-1}\,\text{s}^{-1}$ and $k_d = 6.5 \times 10^{-4}\,\text{s}^{-1}$, proving a reasonable agreement with our measurements.

The rate constants are useful to compare and optimize the time needed to complete a bio-assay. However, they are independent from the sensor characteristics, and for this reason they can not be used to compare between different sensors. In addition, when the biosensor is used far from its saturation, i.e., with low analyte concentrations, the fitting of the time constant τ is affected by huge uncertainties. Therefore, calculating the analyte concentration from Equation (4.5)

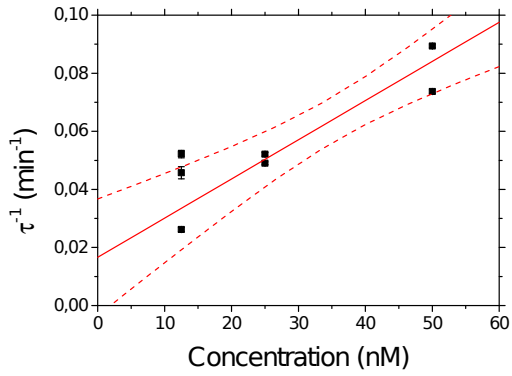

FIGURE 4.28: Dependence of the time constants τ (obtained from the fitted curves of Figure 4.27(c)) to the AFM1 concentration. The slope and intercept of the linear fit are, respectively, the rate constants k_a and k_d. The error bars of every datapoint are shown, but are comparable to the size of the marker. The dashed lines represent the confidence bands of the fitting.

is unreliable, and the preferred choice is the use of the initial slope method [99]. From the fit model Equation (4.4), the initial slope can be calculated as

$$R_0 = \frac{A}{\tau} \tag{4.6}$$

Even if the two parameters A and τ, individually, are fitted with huge uncertainties, they are statistically correlated, and the fit algorithm can calculate the ratio R_0 with much higher accuracy, providing a reliable measurement even at low analyte concentrations. From the comparison of Equation (1.4) and Equation (4.4) we can derive

$$R_0 = \alpha \sigma_0 k_a C \tag{4.7}$$

Table 4.5: Binding kinetic constants, as calculated from the fitted sensorgrams of Figure 4.27(c).

Association rate constant	k_a	$(2.3 \pm 0.3) \times 10^4\,\mathrm{M^{-1}\,s^{-1}}$
Dissociation rate constant	k_d	$(2.8 \pm 1.3) \times 10^{-4}\,\mathrm{s^{-1}}$
Eq. dissociation constant	K_D	$(12 \pm 8)\,\mathrm{nM}$

Here σ_0 is the aptamer surface concentration and α is an effective parameter for the sensor transfer function, summarizing the optical properties of the sensing transduction, including the size and refractive index of the analyte (which are constants) but also the surface sensitivity of the MRR or aMZI sensor. A comparison between different sensors can be obtained by comparing the initial slopes R_0 and keeping constant k_a and σ_0, i.e., using the same functionalization technique. Similarly, different functionalization processes can be compared by analysing the initial slopes R_0 on the same sensor, i.e., with α constant.

In Figure 4.29(a), (b) and (c), we plotted the measured initial slopes as a function of the AFM1 concentration, for the two samples L2 and L5 in TE and TM polarizations. The data are scarce and affected by significant uncertainties, but clearly show increasing trends. The slope of these plots is the specific surface sensitivity S_{AFM1}, which equals the product $S_{\text{AFM1}} = \alpha\sigma_0 k_a$. In Table 4.6 we summarize the values of S_{AFM1} for the measured MRRs sensors, while in Figure 4.29(d), we compare the same to the surface sensitivities calculated with FEM analysis in Figure 3.8(d). The experimental data match nicely with the predicted values. As expected, we see that the highest sensitivity is achieved by using the highest contrast SiON composition and the TM polarization of the light.

To compare these values with similar results reported in literature, we can not use S_{AFM1}, because of its dependence from the specific functionalization. The parameter that is typically accepted is the sensitivity to the superficial density of the bound analyte layer. We can calculate it as

$$S_{s,m} = \frac{S_{\text{AFM1}}}{\sigma_0 k_a \text{MM}} \approx 0.13(6)\,\text{pm}\,\text{mm}^2\,\text{pg}^{-1} \tag{4.8}$$

where $\sigma_0 = 3.5(5) \times 10^{11}\,\text{mm}^{-2}$ [113] is the molecular surface concentration of the aptamer layer, and $\text{MM} = 5.45 \times 10^{-22}\,\text{g}$ is the

Table 4.6: Specific surface sensitivities, S_{AFM1}, as calculated from the linear fits of Figure 4.29.

S_{AFM1}, L2 TE	$0.021(3)\,\text{pm}\,\text{min}^{-1}\,\text{nM}^{-1}$
S_{AFM1}, L2 TM	$0.028(3)\,\text{pm}\,\text{min}^{-1}\,\text{nM}^{-1}$
S_{AFM1}, L5 TE	$0.034(7)\,\text{pm}\,\text{min}^{-1}\,\text{nM}^{-1}$

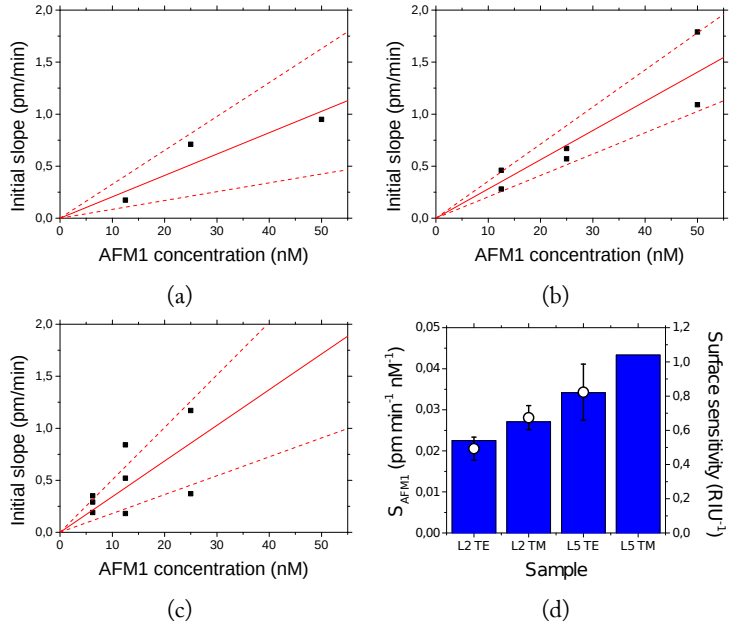

FIGURE 4.29: Sensorgram initial slopes, R_0, as a function of the AFM1 concentration for sample L2 in (a) TE and (b) TM polarizations, and for sample L5 in (c) TE polarization. The error-bars on R_0, given by the fitting uncertainties, are smaller than the datapoint markers. Converesly, the statistical error representing the reproducibility of the trials is much bigger, and it is reported by the the confidence bands (dashed lines). The slope of the linear fit of the datapoints is the specific surface sensitivity S_{AFM1}. (d) Comparison of the fitted specific surface sensitivities S_{AFM1} (points) with the surface sensitivities calculated with the FEM analysis in Figure 3.8(d) (bars).

molecular mass of AFM1. This superficial mass sensitivity, combined with the measured wavelength uncertainty of 0.07 pm, yields in a superficial $\mathrm{LOD}_{s,m} = 2(1)\,\mathrm{pg\,mm^{-2}}$. This value is quite satisfactory, as state-of-the-art biosensors usually exhibit $\mathrm{LOD}_{s,m}$ in the range from 0.3 to 3 $\mathrm{pg\,mm^{-2}}$ [4, 63]. We should remember here that this parameter is not completely fair, as the superficial mass sensitivity could be biased by differences in the susceptibility of the analyte. A better choice would be the use of the superficial sensitivity, S_s, defined in Equation (1.35). However, because of the difficulty in finding tabulated values of the optical properties of the analytes, the use of $\mathrm{LOD}_{s,m}$ is typically preferred.

In conclusion, this section §4.2 covered the detailed characterization of two label-free biosensors, the MRR and the aMZI, from the point of view of the specific recognition of aflatoxin in buffer solution. In particular, we optimized the experimental conditions and protocol to achieve a satisfactory reproducibility in the measurements. These improvements not only could lower the LOD, that we demonstrated to be at least as low as 0.2 nM using an aMZI sensor, but also enabled the multiple re-use of the sensor for a total of nine times.

Despite the additional complication due to the insolubility of AFM1 in water and the added DMSO, the correct interpretation of the sensorgrams yields to the estimation of the rate constant k_a and k_d and of the surface sensitivity of the sensors. This analysis allows a direct comparison of the biosensing characteristics of different devices, as we showed in the case of the MRRs of samples L2 and L5, and it can also be used to compare between different functionalization strategies. To the best of our knowledge, this is the first time that a direct comparison of the surface sensitivity is made between different structures and with the simulated values. A more complete characterization has been reported in [114], even if performed only on a single structure and with some discrepancy between experiment and simulation.

Due to the very low molecular weight of the AFM1, the specific LOD, 0.2 nM, expressed in terms of mass concentration is as low as 66 $\mathrm{pg\,ml^{-1}}$, or 66 ppt. This is a good result for a label-free biosensor. In comparison, SPR devices typically reach limit of detection in the order of 1 $\mathrm{ng\,ml^{-1}}$ [26, 25], whereas silica microspheres can reach 10 $\mathrm{pg\,ml^{-1}}$ [32]. Similarly, nanoplasmonic SPR biosensors exhibit LOD in the range from 10 $\mathrm{ng\,ml^{-1}}$ to 10 $\mathrm{pg\,ml^{-1}}$ [115], with a best record of 1 $\mathrm{pg\,ml^{-1}}$ [116]. Our result competes also with labeled de-

tection: in a recently published work on chemiluminescence sensing the authors reported a LOD value of $60\,\mathrm{pg\,ml^{-1}}$ [19]. Therefore, our devices fairly compares with state-of-the-art technologies, even if some improvements in the optical sensor, in the functionalization and in the sensing protocol (buffer, flow rate and temperature) can still yield in an enhanced limit of detection. One of the future works will be the assessment of an optimized functionalization protocol, which can maximize the specific surface sensitivity S_{AFM1} and minimize the time needed to complete a bio-assay. Another prospected activity is the investigation of a multiplexed sensor, like the one reported in Figure 4.18. The simultaneous reading of more than one MRR should significantly improve the reliability of the sensorgram measurements and minimize the aspecific fluctuations in the signals.

Overall, the performances demonstrated up to here are satisfactory, and perfectly within the specifications of the agreement of the Symphony project.

Conclusions 5

The development of a highly integrated optical biosensor is expected to significantly impact on the performances and on the throughput of biochemical assays, with applications in the field of pharmaceutical research, point-of-care diagnostic, food-borne pathogens screening and safety. In this context, several technologies have appeared and evolved in the last decades, the most famous being the SPR. This is the principle on which several commercial apparatus are based, but despite its maturity level other, more recently proposed, technologies are taking-over. A quite common opinion is that the most promising alternatives are the exploitation of highly-folded Mach-Zenhders or of the resonant features of high-quality-factor optical cavities based on whispering-gallery-modes.

Driven by this firm belief, in this dissertation, I described the design, development and characterization of an integrated photonic label-free biosensor, based on the WGMs of ring resonators or on the new concept of spectrally-resolved aMZIs.

The theoretical chapter provided a general overview, covering the mathematical basis of the two main building blocks of these devices, i.e., the biorecognition reaction and the photonic sensor. For what concerns the former, I modeled the process as a one-to-one binding, and I studied the pseudo-first-order reaction kinetics, in order to be able to reproduce the experimental curves (sensorgrams) and quan-

tify the rate constants. Regarding the latter, I focused on WGMs resonators and on MZIs. The theory provided for the MRRs is quite general, and can be applied also to other topologies (disks, toroids, spheres, etc.). In particular, I derived a relation to calculate the spectral sensitivity, the quality factor and the FOM of a WGM, and I provided the tools for their efficient calculation through numerical analysis. As a significant example, I applied these methods to assess the influence of the cross-section of a wedge microresonator to its properties for biosensing applications. This study revealed that, in order to achieve the highest FOM, the control of the resonator thickness is a primary concern and that, although the wet etching process is necessary to obtain high quality factors, cares have to be taken to prevent a drastic reduction of the inclination angle. A peer-reviewed journal paper has been published on this topic [76]. This dissertation also dealt with MZIs and, in particular, with spectrally-interrogated aMZIs. With respect to MRRs, these devices give more flexibility in the design of the sensors, providing a way to directly control both their sensitivity and resolution. However, the price to pay for obtaining high performances is a large sensing area. I concluded the section by proposing an innovative device that combines the phase-sensitivity of a MZI with the compactness of a MRR. The main difference of this kind of sensor, with respect to the other two, is that its interrogation can be obtained with white (broadband) light, and that a self-stabilizing feedback control can be closed by thermally actuating the reference ring.

In the following chapter I described my achievements in the development of the experimental apparatus. I thoroughly detailed and characterized every part, explaining the pros and cons of the proposed alternatives. I realized a programmable active thermal controller, with high accuracy and temperature stabilization resolution down to 5 mK. The controller is fundamental to suppress aspecific resonance shifts due to temperature fluctuations. I also built and reported on the setup for the fluid handling, which is composed by a commercial continuous flow pump, an injection valve and a custom PDMS flowcell. This apparatus permits handling of bubble-free samples down to the µl range, with a programmable control of the flow rate. The flowcell has been specifically designed to allow an easy alignment to the photonic structures, even on optical chips as small as few millimeters per side. For what concerns the optics, I realized three setups, each

suitable for a fast realtime acquisition and analysis of the transmission spectra of MRRs or aMZIs in a certain wavelength range. I analyzed our photonic resonators either at wavelength of 1550 nm, or in the VIS-NIR range (780 nm and 850 nm), with the aim of investigating alternative approaches for the development of a fully integrated optical chip. Although few issues were highlighted, the scheme that I proposed could measure the resonance wavelengths of modes with moderate-to-high quality factors with a resolution below 0.1 pm, i.e., less than 1/200th of the resonance linewidth. This was accomplished by acquiring oversampled transmission spectra with high SNR, and by fitting in realtime a lorentzian function to track the peak position.

In chapter §4 I reported on the design and characterization of our label-free biosensors. In particular, the design was realised by myself and Dr. Romain Guider. We aimed to the realization of a set of 1×4 multiplexed MRRs sensors. Taking in consideration the limits imposed by the fabrication process, we planned solutions for improved light coupling between

- optical fibers and waveguides,
- arms of the balanced splitters,
- bus waveguides and ring resonators.

During the design of the MRRs, I maximized the FOM, finding the optimized ring thickness, as a function of the light polarization and refractive index of the resonator core.

With the additional planning of several test structures, we (me, Dr. Guider and the bachelor student Alexis Rougemond) thoroughly characterized the propagation and bend losses of the waveguides, the splitting ratio and the length of the directional couplers, the bulk sensitivity and quality factors of the resonators, and the bulk sensitivity of the aMZIs interferometers. In particular, for what concerns the two kind of sensors, we obtained good results, both in terms of sensitivity and limit of detection, which are comparable to state-of-the-art sensors. It is interesting to note that the accurate design, through the theory developed in §1 and FEM simulations, yielded optical circuits and sensors with satisfactory performances right from the first mask layout. In the second mask design, which has been planned to realize a prototype with integrated detectors, we introduced only small variations to compensate for fabrication issues.

Finally, we demonstrated the effective use of our sensors for the biodetection of Aflatoxin-M1 in controlled buffer solutions. With the colleagues of FBK, we functionalized the surface of the MRRs and aMZIs with anti-aflatoxin DNA-aptamers. Aim of the experiments were the testing of the functionalization process and of the solutions for regeneration of the surface, as well as the assessment of the specific sensitivity and LOD of our photonic devices. With the refinement of the measurement protocol, we managed to obtain results with a sufficient reproducibility, so that I could evaluate the kinetic rate constants and the specific sensitivity S_{AFM1}. Our results are still affected by large uncertainties, but seem to be compatible with the ones of similar bioreceptors. Moreover, I evaluated the LOD, both in terms of surface-deposited mass concentration and of analyte bulk concentration. The former is in the order of $1\,\mathrm{pg\,mm^{-2}}$, while the latter was observed down to 0.2 nM, which for AFM1 is equivalent to $66\,\mathrm{pg\,ml^{-1}}$. Both values are at the level of, or even better than, state-of-the-art competing technologies.

The work here presented poses the basis for the successful achievement of the ambitious objectives of the Symphony project. Obviously, the photonic sensor and the surface functionalization are just small (but fundamental) gears, that have to fit perfectly in a more complete, and complex, device. Both aMZIs and MRRs have shown good sensing performances, with slightly better values measured in the former case. In my opinion, an aMZI should be preferred for applications where a low LOD is more important than space consumption and multiplexing. Conversely, the MRRs have greater potentials for dense and highly multiplexed sensors, thanks to the lower insertion losses and the smaller footprints. In addition, it should be possible to realize MRRs with higher quality factors and, hence, lower LOD values, as it appears from my calculations and from the observation of similar devices. However, major problems are presently limiting the performances of our rings: firstly, the poor lithography resolution and the problems encountered during the etching of the structures (see §4.1.4), and, secondly, the uncertainty in the readout apparatus. For what concerns the fabrication, the problems can be solved with the use of a higher resolution and more reproducible lithography technique. In alternative, the roughness on the sidewalls can be reduced by adopting a wedge resonator structure, since the technology for the realization of vertical couplings to the bus-

waveguides is now available again. For what concerns the readout, I think that the temperature stabilization during the sample injections and the accurate estimation of the wavelength of the laser source are the main issues of the current apparatus.

As an outlook on the future improvements on the experimental apparatus, I think that the simultaneous measurement of two or more multiplexed sensors will lead to the effective reduction of the wavelength uncertainty due to bulk refractive index and temperature variations. We are already working in this direction, and we hope to get encouraging results soon. To further improve the accuracy of the wavelength measurement, I am thinking of implementing an off-chip spectrum reference with a fiber-based asymmetric Mach-Zehnder. The interference patter will serve as a low-finesse ethalon to resolve small wavelength variations, and to suppress the uncertainty arising from the fluctuations in the light source. These improvements will be advantageous for both the MRRs and the aMZIs, but the higher FOM of the latter will result in more evident benefits.

To conclude, I want to comment on the system integration and scalability, in comparison to different biosensing approaches. The strategy adopted by the Symphony consortium is focused on a small number (4 to 8) of multiplexed sensor. Wondering about its scalability to larger number of sensing sites, I think that different readout strategies should be investigated. Even if we could manage to integrate reliably both the laser source and the photodetectors, the number of electrical contacts will grow linearly with the number of sensing sites, soon limiting the feasibility of a simple plug-and-play disposable cartridge. From this perspective, I think that there are only two foreseeable strategies:

1. The on-chip implementation of logic functions, to digitally convert the measurements of the photodetectors and serialize the communication. In this case every sensor will act as a pixel in a linear array.

2. The direct access to the chip via optical links, similarly to the strategy of prism-coupled SPR sensors or to the elegant proposal of [99].

The first solution is quite involved and, to the best of my knowledge, nobody has explored it yet. The second one is being explored

by researchers at universities and companies, but it is still limited to about a hundred of sensing sites. In comparison, labeled detection of sandwich-type ELISA microarrays can offer more than a thousand of sensing sites. Thus, I think that CMOS-compatible photonics has great potentials, but it requires a seamless integration with microelectronics before becoming a real breakthrough. Until the technology will not be more mature, the strength of MZI or WGM biosensors will not be the high throughput but the high FOM and the low LOD. The objectives of the Symphony consortium are consistent with this strategy, i.e., the development of a system for a fast and simple (from the operator's point-of-view) on-line detection of traces of small molecules (aflatoxin-M1, in this case) on a small number (4 to 8) of multiplexed sensor.

Surface bio-functionalization A

A.1 Preparation

The functionalization of the sensor chips was performed by means of a wet silanization of the entire chip. Figure A.1 schematically represents the steps of the functionalization protocol, which are described as follows:

1. Surface activation, achieved through an argon plasma cleaning at 40 W of radiofrequency power. This step removes the possible contaminants from the surface and exposes the hydroxyl groups necessary to bind the organosilanes.

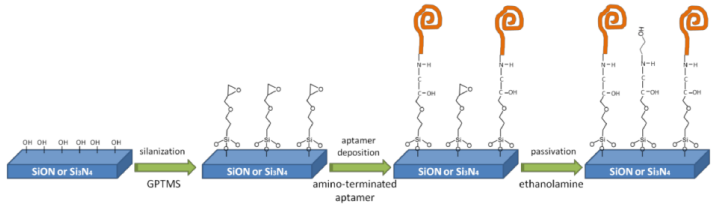

Figure A.1: Schematic representation of the functionalization process.

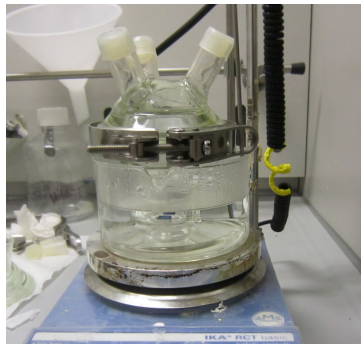

(a)

(b)

Figure A.2: Pictures of two steps of the functionalization procedure. (a) Silanization with GPTMS in anhydrous toluene. (b) Rinsing before immobilization of the DNA-aptamers. Pictures from [83].

2. Wet silanization, accomplished in a 3-Glycidyloxypropyltrimethoxysilane (GPTMS, $\geq$98 % from *Sigma-Aldrich*) at 0.01 % v/v in anhydrous toluene (99.8 %, from *Sigma-Aldrich*), at 60 °C for 10 min (see Figure A.2).

3. Deposition and immobilization of 100 µM amino-modified anti-aflatoxin DNA aptamer, performed in 50 mM phosphate buffer (ionic strength 300 mM) for 2 h. The NH_2 of the aptamer undergoes an addition reaction with the epoxide group of the glycidol, forming a hydroxyl group and a secondary amine, which gives an aptamer-silane bonding.

4. Passivation with 1 mM ethanolamine, in the same buffer, for 30 min.

A.2 Sensing buffers

MES

- Composition:

  - *MilliQ* water,
  - 50 mM 2-(N-morpholino)ethanesulfonic acid.
- pH: 6.6
- Notes: same pH as milk. Very stable buffer, low bulk shift.

Tris-HCl

- Composition:
  - *MilliQ* water,
  - 10 mM Tris(hydroxymethyl)aminomethane,
  - 120 mM NaCl,
  - 5 mM KCl,
  - 5 mM $MgCl_2$,
  - HCl as needed to adjust the pH value.
- pH: 7.5
- Notes: buffer composition suggested by NeoVentures (the company selling the aptamers). During our experiments we reported significant aspecific drifts with this buffer.

PBS

- Composition:
  - *MilliQ* water,
  - 50 mM PBS mixture.
- pH: 7
- Notes: although this buffer provided satisfactory stable signals, the refractive index is high. For this reason PBS gave higher bulk aspecific signals. The pH value is close to that of milk. This buffer has been used successfully for immunoassay with antibodies [110].

A.3 Regeneration solutions

Glycine

- Composition:
  - 100 mM glycine,
  - HCl as needed to adjust the pH value.
- pH: 2
- Notes: up to 9 regeneration cycles have been succesfully repeated on a single sensor, as demonstrated in Figure 4.27.

Sodium acetate

- Composition:
  - 1 mM $NaC_2H_3O_2$ (sodium acetate),
  - $C_2H_4O_2$ (acetic acid) as needed to adjust the pH value.
- pH: 3.7
- Notes: no sizeable regeneration effect has been observed.

Realtime data extraction B

In this section we describe the data acquisition and analysis, in realtime, concerning the apparatus of Figure 2.11, which has been employed both with the *Sacher Lasertechnik LiON* external cavity tunable laser at 780 nm and with the *Philips U-L-M* VCSEL at 850 nm.

B.1 Data acquisition

To reconstruct the transmission spectra, we simultaneously acquire the outputs of two photodiodes (signal and normalization reference) with a four-channels oscilloscope. The wavelength is inferred from the signal on the third channel. During the development of our setup, we tested two alternatives strategies for the measurement of the wavelength.

In the first, the wavelength is calculated as a function of the direct reading of the modulation signal

$$\lambda = f(V)$$

To be more precise, the modulation signal V is acquired and then fitted linearly, to reduce the noise. The fitted signal $\tilde{V}$ is then fed into the function, so that $\lambda = f(\tilde{V})$. In the case of the piezoelectric actuator, $f(*)$ is a linear function with slope $4\,\mathrm{pm\,V^{-1}}$. In the case

of the VCSEL, the function $f(*)$ is a third-degree polynomial, as shown in Figure 2.16(b).

In the second strategy, we just read the synchronization signal of the sawtooth function generator, and we infer the instantaneous modulation voltage from the time passed from the trigger (knowing the settings of the function generator).

The advantage of first method is that we do not rely on the "expected" modulation voltage, but we directly read the value. However, as a side effect, the noise (electrical or quantization) affecting the measurement of V is transferred, through the fitting, to λ. Conversely, the second case is less "robust" as it relies on the nominal voltage applied by the function generator, but it is immune to the electrical noise. The noise in the time estimation (jitter) is negligible in an oscilloscope. A comparison of both methods shows that the second configuration (trigger-based) reduces the uncertainty in the wavelength estimation by about three times, as visible in the green and red curves of Figure 4.9(a), with respect to the balck one.

B.2 Data analysis algorithm

For every acquired spectrum, a *Matlab* script, embedded in the *LabView* code of the acquisition program, analyzes the data and extract the signal used for the sensing. The algorithms are different, depending on the kind of photonic sensor.

B.2.1 MRRs

In the case of MRRs, the script is quite simple. These are the commented steps:

1. The wavelength and the transmission ratio (the ratio of the signals of the two photodetectors is calculated within the *LabView* code) are imported as column vectors and sorted for increasing λ. The sorting is not fundamental, but produces better-looking plots (for debugging purposes).

2. The transmission is normalized to the maximum value, but a copy of the original is saved for later use.

3. The two arrays are decimated (low-pass filtered) to reduce the noise level. `dn` and `do` are the decimation number and order,

respectively, and are parameters that can be changed from the *LabView* user interface. Typical values are 100 and 3.

4. A portion of the spectrum is selected, for wavelengths delimited by two external parameters, `fit_start` and `fit_stop`.

5. Within this range, the resonance wavelength is coarsely estimated by finding the minimum value.

6. A sub-portion of the spectrum is determined, by expanding the selection to both sides of the minimum, for a number of datapoints determined by the external parameter `n_broadening` (typically equal to 20, so that every resonance is fitted with 51 points). This sub-portion of the spectrum is denoted by the lowercase `x` and `y`.

7. The initial fitting parameters are coarsely estimated, and then fed to the procedure `lsqcurvefit` to calculate the least-square fit to the datapoints. The function `lorentz` is a custom function (reported here below) that calculates a lorentzian peak and its jacobian (for a faster convergence of the minimization algorithm).

8. The quality factor `Q` and the resonance position `xc` are calculated from the parameters `p` of the fitted lorentzian. The value `top` is an auxiliary information that is used during the measurements to track the alignment of the fibers.

The *Matlab* code is here reported:

```
X = wavelength';
[X, I] = sort(X);
Y = ratio'; % Ratio of the two photodetectors
Y = Y(I);
Yorig=Y;
Y = Y./max(Y); % Normalization to the maximum

X = decimate(X,dn,do);
Y = decimate(Y,dn,do);
Yorig = decimate(Yorig,dn,do);
len = length(Y);
```

```
sel = (X>fit_start) & (X<fit_stop)
X = X(sel);
Y = Y(sel);

[ymin, i] = min(Y);
top = 0;
Q = 0;
xc = 0;
if(ymin<1)
is = i-n_broadening;
ie = i+n_broadening;

if(is>0 && ie<len)
    fit_opts = optimoptions('lsqcurvefit','Jacobian','on');

        x = X(is:ie);
        y = Y(is:ie);
     p0 = [ max(y); min(y)-max(y); x(floor(end/2)); (x(end)-x(1))/2 ];
     p = lsqcurvefit(@lorentz, p0, x, y,[0;-inf;x(1);eps],[1;0;x(end);inf],fit_opts);

        Q = p(3)./(2*p(4));
        xc = p(3);
        top = mean(Yorig([1:is,ie:len]));
  end
end

function [y, J] = lorentz(p, x)
    y0=p(1); A=p(2); xc=p(3); g=p(4);

    den = 1./((x-xc).^2+g^2);
    y = y0 + (A*g^2).*den;

    if nargout > 1   % two output arguments
        den2 = den.^2;
        if isrow(x)
            J = zeros(4,length(x));
            J(1,:) = ones(size(J(1,:)));                % dL/dy0
            J(2,:) = (g^2).*den;                         % dL/dA
            J(3,:) = (2*A*g^2).*den2.*(x-xc);           % dL/dxc
            J(4,:) = (2*A*g).*den - (2*A*g^3).*den2;    % dL/dg
```

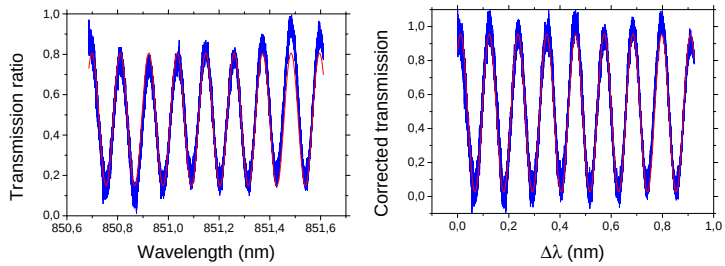

(a) (b)

FIGURE B.1: Comparison of the transmission spectra (a) as acquired and (b) after the polynomial baseline correction. The fitted curves, in red, show the difference in the fitting quality.

```
    else
        J = zeros(length(x),4);
        J(:,1) = ones(size(J(:,1)));                % dL/dy0
        J(:,2) = (g^2).*den;                         % dL/dA
        J(:,3) = (2*A*g^2).*den2.*(x-xc);           % dL/dxc
        J(:,4) = (2*A*g).*den - (2*A*g^3).*den2;     % dL/dg
    end
end
```

B.2.2 aMZIs

For what concerns the analysis of the aMZI spectra, the algorithm is slightly more complicated by the fact that the transmission spectra are distorted by nonlinear baselines, as shown in Figure B.1(a). A sinusoidal fitting on the data could be achieved in any case, yielding in large residuals. The algorithm here developed corrects the baseline before calculating the fitting parameters, so that the residuals are smaller, as depicted in Figure B.1(b).

Here we explain the details of the algorithm:

1. The wavelength and the transmission ratio are imported as column vectors and sorted for increasing λ. The value of the wavelength is translated by 850 nm for convenience.

2. Both arrays are decimated (low-pass filtered) by a number of points fixed by the external parameter `Ndecimate`.

3. The baseline-correction algorithm takes place, with the following instructions:

   a) The datapoints are divided in two sets, depending on their `Y` value: above or below the midpoint 0.5. Here we assume that the variable attenuator on the reference photodetector is regulated to give normalized transmission spectra balanced around that value.

   b) The upper and the bottom parts are fitted with a polynomial function of order `poly_order`, which is an external parameter that can be changed through the user interface. Since the peaks and the valleys are more dense of datapoints, with respect to the rising or decreasing parts of the transmission, the fitted polynomials roughly interpolate the top and bottom envelope of the spectrum.

   c) The datapoints `Y` and the envelopes `Yfit_up` and `Yfit_dn` are first scaled and then translated to yield the transmission spectrum of Figure B.1(b).

   The whole procedure is repeated two times.

4. Notice that, if the frequency (which actually is the free-spectral-range) of the sinusoid to be fitted is known (`d`, in the script), the problem of finding the amplitude, the phase and the offset of the sinusoid is actually a linear inversion problem, that can be achieved efficiently by *Matlab* with the operator `\`. For this reason two functions are defined: `cfun` and `sumerr2`. The former calculates the offset and the two amplitudes of the sine and cosine with frequency `d` that fit the data `Y`. The latter calculates the sum of the squared errors.

5. If the frequency is not fixed as an external parameters, a minimization process is performed on `sumerr2` to find the best-fitting frequency. If the frequency is fixed, this step is skipped.

6. The offset and the two amplitudes are calculated with `cfun`, and from these the amplitude and the phase of the sinusoidal function are calculated.

Here is the script:

```
X = wavelength';
Y = ratio'; % Ratio of the two photodetectors
[X, I] = sort(X);
Y = Y(I);
X = X-850;

if(Ndecimate~=1)
   Xorig = X;
   Yorig = Y;
   Y = decimate(Y,Ndecimate);
   X = decimate(X,Ndecimate);
end

for k=1:2 % Two cycles of baseline correction
sel_l = Y < 0.5;
sel_r = Y > 0.5;

p_up = polyfit(X(sel_r),Y((sel_r)),poly_order);
p_dn = polyfit(X(sel_l),Y((sel_l)),poly_order);
Yfit_up = polyval(p_up,X);
Yfit_dn = polyval(p_dn,X);

fs = 0.6./(Yfit_up - Yfit_dn);
Y = Y.*fs;
Yfit_up = Yfit_up.*fs;
Yfit_dn = Yfit_dn.*fs;
fo = (Yfit_up + Yfit_dn)./2-0.5;
Y = Y-fo;
Yfit_up = Yfit_up-fo;
Yfit_dn = Yfit_dn-fo;
end

y = Y';
x = X';

cfun = @(d) [ones(size(x)),sin(2*pi*d*x),cos(2*pi*d*x)]\y;
sumerr2 = @(d) sum((y-[ones(size(x)),sin(2*pi*d*x),cos(2*pi*d*x)]*cfun(d)).^2);

if (fix_freq == 0)
    freq_opt = fminbnd(sumerr2,freq_lb,freq_ub);
```

```
else
    freq_opt = fix_freq;
end

coeff = cfun(freq_opt);

y0 = coeff(1);
A = norm( coeff(2:3) );
phi = atan2( coeff(3),coeff(2) );
```

Dissemination activities

Peer-review journal papers

1. D. Gandolfi, F. Ramiro-Manzano, F. J. Rebollo Aparico, M. Ghulinyan, G. Pucker, and L. Pavesi. Role of Edge Inclination in an Optical Microdisk Resonator for Label-Free Sensing. *Sensors*, 15(3):4796–4809, 2015.

2. F. J. Aparicio, E. Froner, E. Rigo, D. Gandolfi, M. Scarpa, B. Han, M. Ghulinyan, G. Pucker, and L. Pavesi. Silicon oxynitride waveguides as evanescent-field-based fluorescent biosensors. *Journal of Physics D: Applied Physics*, 47(40):405401, 2014.

3. P. Ingenhoven, A. Anopchenko, A. Tengattini, D. Gandolfi, F. Sgrignuoli, G. Pucker, Y. Jestin, L. Pavesi, and R. Balboni. Quantum effects in silicon for photovoltaic applications. *Physica Status Solidi: A*, 210(6):1071–1075, 2013.

4. A. Tengattini, D. Gandolfi, N. Prtljaga, A. Anopchenko, J. M. Ramirez, F. Ferrarese Lupi, Y. Berencen, D. Navarro-Urrios, P. Rivallin, K. Surana, B. Garrido, J.-M. Fedeli, and L. Pavesi. Toward a 1.54 μm Electrically Driven Erbium-Doped Silicon Slot Waveguide and Optical Amplifier. *Journal of Lightwave Technology*, 31(3):391–397, 2013.

5. D. Gandolfi, M. Niedermayr, M. Kumph, M. Brownnutt, and R. Blatt. Compact radio-frequency resonator for cryogenic ion traps. *Review of Scientific Instruments*, 83(8):084705, 2012.

Books

1. M. Franchi, D. Gandolfi, and L. M. Martini. *Proceedings of the event IPSP2014: Industrial Problem Solving with Physics*. Università degli Studi di Trento, Trento, ISBN: 978-88-8443-580-4, 2015.

2. M. Borghi, D. Gandolfi, M. Ghulinyan, R. Guider, M. Mancinelli, G. Pucker, F. Ramiro-Manzano, F. Turri, and L. Pavesi. *Silicon microresonators: how to give a new twist to silicon photonics*. book chapter in *Plenary Lectures on Nanoscience and Engineering*, in press, 2015.

Non peer-review journal papers

1. D. Gandolfi, R. Guider, T. Chalyan, L. Pasquardini, A. Samusenko, C. Pederzolli, G. Pucker, and L. Pavesi. Sensitivity and Limit of detection of biosensors based on ring resonators. *Proceedings of XVIII AISEM Annual Conference*, in press.

2. A. Samusenko, V. J. Hamedan, R. Guider, D. Gandolfi, L. Pavesi, G. Pucker, M. Ghulinyan, and F. Ficorella. Integrated silicon photodetector for lab-on-chip sensor platform. *Proceedings of XVIII AISEM Annual Conference*, in press.

3. D. Gandolfi, F. Ramiro-Manzano, F. Aparicio Rebollo, M. Ghulinyan, G. Pucker, L. Pavesi, Role of edge inclination in optical microdisk resonator for label-free sensing. *arXiv*:1408.3954 [physics.optics], 2014.

4. A. Tengattini, D. Gandolfi, A. Marconi, A. Anopchenko, N. Prtljaga, J. M. Ramirez, F. Ferrarese Lupi, Y. Berencen, D. Navarro Urrios, B. Garrido, J.-M. Fedeli, P. Rivallin, K. Surana, and L. Pavesi. Opto-Electrical Characterization of Erbium Doped Slot Waveguides. *Proceedings of SPIE, the International Society for Optical Engineering*, 8431:843118–843118, 2012.

5. D. Gandolfi, M. Niedermayr, M. Kumph, M. Brownnutt, and R. Blatt. Compact RF resonator for cryogenic ion traps. *arXiv*1204.5004 [physics.atom-ph], 2012.

6. A. Anopchenko, F. J. Aparicio Rebollo, P. Bettotti, F. Bianco, P. Bellutti, M. Cazzanelli, K. Fedus, E. Froner, D. Gandolfi, M. Ghulinyan, N. Kumar, Y. Jestin, P. Ingenhoven, S. Larcheri, L. Lunelli, M. Mancinelli, A. Marconi, E. Moser, L. Pasquardini, C. Pederzolli, C. Potrich, N. Prtljaga, G. Pucker, F. Ramiro-Manzano, E. Rigo, M. Scarpa, F. Sgrignuoli, A. Tengattini, and L. Pavesi. La Nanofotonica in Silicio e la Fotonica con il Nanosilicio - Una piattaforma per ampliare il successo della fotonica in silicio. *Il Nuovo Saggiatore*, 28:5–15, 2012.

International conferences

1. D. Gandolfi, R. Guider, T. Chalyan, L. Pasquardini, A. Samusenko, C. Pederzolli, G. Pucker, and L. Pavesi. Sensitivity and Limit of Detection of biosensors based on ring resonators. *AISEM 2015 Annual Conference*, 3-5 February 2015, Trento, Italy.

2. L. Pasquardini, L. Pancheri, C. Potrich, C. Piemonte, L. Lunelli, M. Ghulynian, G. Pucker, S. Berneschi, S. Soria, D. Gandolfi, L. Pavesi, L. Lorenzelli, D. Stoppa, and C. Pederzolli. Design of optical sensors for blood protein recognition. *SIFB annual congress*, 11-13 June 2014, Trento, Italy.

3. D. Gandolfi, M. Guarisco, F. Ramiro Manzano, L. Pasquardini, C. Pederzolli, M. Ghulinyan, G. Pucker, and L. Pavesi. Enhanced integrated optical resonators for label-free biosensing. *SPIE Photonics Europe 2014*, 14-17 April 2014, Brussels, Belgium.

4. D. Gandolfi, G. Pucker, M. Guarisco, L. Pasquardini, M. Ghulinyan, and L. Pavesi. Enhanced sensitivity in label free sensing using integrated wedge resonators. *EUROPT(R)ODE XII*, 13-16 April 2014, Athens, Greece.

5. D. Gandolfi, F. J. Aparicio, M. Signoretto, F. Ramiro-Manzano, L. Pasquardini, M. Ghulinyan, C. Pederzolli, and L. Pavesi. Comparison of novel structures for label-free biosensing. *5th EOS Topical Meeting on Optical Microsystems*, 12-14 September 2013, Capri, Italy (EOS-Springer Best Student presentation award)

6. D. Gandolfi, F. J. Aparicio, M. Signoretto, F. Ramiro-Manzano, L. Pasquardini, M. Ghulinyan, C. Pederzolli, and L. Pavesi. Integrated and Mass-Producible Label-Free Biosensor. *Fotonica 2013*, 21-23 May 2013, Milano, Italy.

7. A. Tengattini, A. Anopchenko, N. Prtljaga, D. Gandolfi, M. Cazzanelli, J. M. Ramìrez, F. Ferrarese Lupi, Y. Berencén, D. Navarro-Urrios, O. Jambois, B. Garrido, J. M. Fedeli, and L. Pavesi. Er3+/silicon nanocrystals co-doped devices: from a light emitting diode to an injected slot waveguide. *EOS Annual Meeting 2012*, 25-28 September 2012, Aberdeen, Scotland.

8. A. Tengattini, D. Gandolfi, A. Anopchenko, N. Prtljaga, J. M. Ramírez, Y. Berencén, F. Ferrarese Lupi, B. Garrido, and L. Pavesi. Electrically excited erbium in slot waveguides. *Fotonica 2012*, 15-17 May 2012, Firenze, Italy.

9. D. Gandolfi, A. Tengattini, A. Anopchenko, N. Prtljaga, J. M. Fedeli, P. Rivallin, K. Surana, and L. Pavesi. Optical characterization of electrically pumped Erbium-doped slot-waveguides (poster). *AIP-ICTP Industrial Physics Forum 2012*, 16-20 April 2012, Miramare, Trieste, Italy.

Bibliography

[1] K B Mullis, H A Erlich, N Arnheim, G T Horn, R K Saiki, and S J Scharf. US patent US4683195 A, 1987.

[2] R. Edwin Oosterbroek and Albert van den Berg. *Lab-on-a-Chip*. Elsevier B.V., Amsterdam, 2003.

[3] Lorenzo Pavesi and Philippe M. Fauchet, editors. *Biophotonics*. Springer-Verlag, Berlin, 2008.

[4] W. Bogaerts, P. De Heyn, T. Van Vaerenbergh, K. De Vos, S. Kumar Selvaraja, T. Claes, P. Dumon, P. Bienstman, D. Van Thourhout, and R. Baets. Silicon microring resonators. *Laser Photonics Reviews*, 6(1):47–73, 2012.

[5] S. Feng, T. Lei, H. Chen, H. Cai, X. Luo, and A.W. Poon. Silicon photonics: from a microresonator perspective. *Laser & Photonics Reviews*, 6(2):145–177, April 2012.

[6] David Lockwood and Lorenzo Pavesi. *Silicon photonics II. Components and integration*. Springer, Berlin, 2nd edition, 2011.

[7] Andrea L. Martin, Deniz K. Armani, Lan Yang, and Kerry J. Vahala. Replica-molded high-Q polymer microresonators. *Optics Letters*, 29(6):533, March 2004.

[8] C.Y. Chao, W. Fung, and L.J. Guo. Polymer microring resonators for biochemical sensing applications. *IEEE Journal of Selected Topics in Quantum Electronics*, 12(1):134–142, January 2006.

[9] Adam L Washburn, Matthew S Luchansky, Adrienne L Bowman, and Ryan C Bailey. Quantitative, label-free detection of five protein biomarkers using multiplexed arrays of silicon photonic microring resonators. *Analytical chemistry*, 82(1):69–72, January 2010.

[10] Neelam Verma and Minni Singh. Biosensors for heavy metals. *BioMetals*, 18(2):121–129, April 2005.

[11] L A Pinnaduwage, A Gehl, D L Hedden, G Muralidharan, T Thundat, R T Lareau, T Sulchek, L Manning, B Rogers, M Jones, and J D Adams. Explosives: a microsensor for trinitrotoluene vapour. *Nature*, 425(6957):474, 2003.

[12] Wei Pang, Hongyuan Zhao, Eun Sok Kim, Hao Zhang, Hongyu Yu, and Xiaotang Hu. Piezoelectric microelectromechanical resonant sensors for chemical and biological detection. *Lab on a Chip*, 12:29, 2012.

[13] L. G. Carrascosa, M. Moreno, M. Álvarez, and L. M. Lechuga. Nanomechanical biosensors: A new sensing tool. *Trends in Analytical Chemistry*, 25:196–206, 2006.

[14] Matthew A. Cooper and Victoria T. Singleton. A survey of the 2001 to 2005 quartz crystal microbalance biosensor literature: Applications of acoustic physics to the analysis of biomolecular interactions. *Journal of Molecular Recognition*, 20:154–184, 2007.

[15] Frances S. Ligler and Chris Rowe Taitt. *Optical Biosensors: Present & Future*. Elsevier Science, 2002.

[16] Eva Engvall and Peter Perlmann. Enzyme-linked immunosorbent assay (ELISA) quantitative assay of immunoglobulin G. *Immunochemistry*, 8(9):871–874, September 1971.

[17] Hye Jin Lee, Alastair W Wark, and Robert M Corn. Microarray methods for protein biomarker detection. *The Analyst*, 133:975–983, 2008.

[18] Geertruida a. Posthuma-Trumpie, Jakob Korf, and Aart Van Amerongen. Lateral flow (immuno)assay: Its strengths,

weaknesses, opportunities and threats. A literature survey. *Analytical and Bioanalytical Chemistry*, 393:569–582, 2009.

[19] Laura Pasquardini, Lucio Pancheri, Cristina Potrich, Alessandro Ferri, Claudio Piemonte, Lorenzo Lunelli, Lucia Napione, Valentina Comunanza, Maria Alvaro, Lia Vanzetti, Federico Bussolino, and Cecilia Pederzolli. SPAD aptasensor for the detection of circulating protein biomarkers. *Biosensors and Bioelectronics*, 68:500–507, 2015.

[20] David S. Smith and Sergei a. Eremin. Fluorescence polarization immunoassays and related methods for simple, high-throughput screening of small molecules. *Analytical and Bioanalytical Chemistry*, 391:1499–1507, 2008.

[21] David M Rissin, Cheuk W Kan, Todd G Campbell, Stuart C Howes, David R Fournier, Linan Song, Tomasz Piech, Purvish P Patel, Lei Chang, Andrew J Rivnak, Evan P Ferrell, Jeffrey D Randall, Gail K Provuncher, David R Walt, and David C Duffy. Single-molecule enzyme-linked immunosorbent assay detects serum proteins at subfemtomolar concentrations. *Nature biotechnology*, 28(6):595–599, 2010.

[22] S D Jayasena. Aptamers: an emerging class of molecules that rival antibodies in diagnostics. *Clinical chemistry*, 45(9):1628–50, October 1999.

[23] Michael J. Whitcombe, Nicole Kirsch, and Ian A. Nicholls. Molecular imprinting science and technology: A survey of the literature for the years 2004-2011. *Journal of Molecular Recognition*, 27:297–401, 2014.

[24] Cameron Alexander, Håkan S. Andersson, Lars I. Andersson, Richard J. Ansell, Nicole Kirsch, Ian A. Nicholls, John O'Mahony, and Michael J. Whitcombe. Molecular imprinting science and technology: A survey of the literature for the years up to and including 2003. *Journal of Molecular Recognition*, 19:106–180, 2006.

[25] Xudo Fan, Ng, Ian M White, Siyka I Shopova, Hongying Zhu, Jonathan D Suter, and Yuze Sun. Sensitive optical biosensors for unlabeled targets: a review. *Analytica chimica acta*, 620(1-2):8–26, July 2008.

[26] Jiří Homola. Surface plasmon resonance sensors for detection of chemical and biological species. *Chemical Reviews*, 108:462–493, 2008.

[27] B. O. Liedberg, C. Nylander, and I. Lundstrom. Surface plasmon resonance for gas detection and biosensing. *Sensors and Actuators*, 4:299–304, 1983.

[28] P. I. Nikitin, A. N. Grigorenko, A. A. Beloglazov, M. V. Valeiko, A. I. Savchuk, O. A. Savchuk, G. Steiner, C. Kuhne, A. Huebner, and R. Salzer. Surface plasmon resonance interferometry for micro-array biosensing. *Sensors and Actuators, A: Physical*, 85:189–193, 2000.

[29] Christina Boozer, Gibum Kim, Shuxin Cong, HannWen Guan, and Timothy Londergan. Looking towards label-free biomolecular interaction analysis in a high-throughput format: a review of new surface plasmon resonance technologies. *Current Opinion in Biotechnology*, 17:400–405, 2006.

[30] C. G B Garrett, W. Kaiser, and W. L. Bond. Stimulated emission into optical whispering modes of spheres. *Physical Review*, 124:1807–1809, 1961.

[31] F. Vollmer, D. Braun, A. Libchaber, M. Khoshsima, I. Teraoka, and S. Arnold. Protein detection by optical shift of a resonant microcavity. *Applied Physics Letters*, 80(21):4057, 2002.

[32] Frank Vollmer and Lan Yang. Review Label-free detection with high-Q microcavities: a review of biosensing mechanisms for integrated devices. *Nanophotonics*, 1(3-4):267–291, December 2012.

[33] Mher Ghulinyan, Romain Guider, Georg Pucker, and Lorenzo Pavesi. Monolithic Whispering-Gallery Mode Resonators With Vertically Coupled Integrated Bus Waveguides. *IEEE Photonics Technology Letters*, 23(16):1166–1168, August 2011.

[34] Fernando Ramiro-Manzano, Nikola Prtljaga, Lorenzo Pavesi, Georg Pucker, and Mher Ghulinyan. A fully integrated high-Q Whispering-Gallery Wedge Resonator. *Optics Express*, 20(20):22934, September 2012.

[35] Frank Vollmer and Stephen Arnold. Whispering-gallery-mode biosensing: label-free detection down to single molecules. *Nature methods*, 5(7):591–6, July 2008.

[36] Jiangang Zhu, Sahin Kaya Ozdemir, Yun-Feng Xiao, Lin Li, Lina He, Da-Ren Chen, and Lan Yang. On-chip single nanoparticle detection and sizing by mode splitting in an ultrahigh-Q microresonator. *Nature Photonics*, 4(1):46–49, December 2009.

[37] Martin D Baaske, Matthew R Foreman, and Frank Vollmer. Single-molecule nucleic acid interactions monitored on a label-free microcavity biosensor platform. *Nature nanotechnology*, 9:933–939, 2014.

[38] Stephen Arnold, Stephen Holler, and Xudong Fan. Taking microcavity label-free single molecule detection deep into the protein realm: Cancer marker detection at the ultimate sensitivity. In Baldassare Di Bartolo, John Collins, and Luciano Silvestri, editors, *Nano-Structures for Optics and Photonics*, NATO Science for Peace and Security Series B: Physics and Biophysics, pages 309–322. Springer Netherlands, 2015.

[39] F Prieto, B Sepúlveda, A Calle, A Llobera, C Domínguez, A Abad, A Montoya, and L M Lechuga. An integrated optical interferometric nanodevice based on silicon technology for biosensor applications. *Nanotechnology*, 14:907–912, 2003.

[40] Stefania Dante, Daphné Duval, Borja Sepúlveda, Ana Belen González-Guerrero, José Ramón Sendra, and Laura M. Lechuga. All-optical phase modulation for integrated interferometric biosensors. *Optics Express*, 20:7195, 2012.

[41] E. Coscelli, M. Sozzi, F. Poli, D. Passaro, A. Cucinotta, S. Selleri, R. Corradini, and R. Marchelli. Toward A Highly Specific DNA Biosensor: PNA-Modified Suspended-Core Photonic Crystal Fibers. *IEEE Journal of Selected Topics in Quantum Electronics*, 16, 2010.

[42] Davide Passaro, Matteo Foroni, Federica Poli, Annamaria Cucinotta, Stefano Seileri, Jesper Læ gsgaard, and Anders Overgaard Bjarklev. All-silica hollow-core microstruc-

tured Bragg fibers for biosensor application. *IEEE Sensors Journal*, 8:1280–1286, 2008.

[43] E. Rigo, F. J. Aparicio, M. R. Vanacharla, S. Larcheri, R. Guider, B. Han, G. Pucker, and L. Pavesi. Evanescent-field excitation and collection approach for waveguide based photonic luminescent biosensors. *Applied Physics B*, 114(4):537–544, July 2013.

[44] F J Aparicio, E Froner, E Rigo, D Gandolfi, M Scarpa, B Han, M Ghulinyan, G Pucker, and L Pavesi. Silicon oxynitride waveguides as evanescent-field-based fluorescent biosensors. *Journal of Physics D: Applied Physics*, 47(40):405401, October 2014.

[45] Symphony consortium. Symphony - Annex I - "Description of Work". Technical report, 2013.

[46] Jörgen Vessman, Raluca I. Stefan, Jacobus F. van Staden, Klaus Danzer, Wolfgang Lindner, Duncan Thorburn Burns, Ales Fajgelj, and Helmut Müller. Selectivity in analytical chemistry (IUPAC Recommendations 2001). *Pure and Applied Chemistry*, 73:1381-1386, 2001.

[47] Camille L A Hamula, Jeffrey W. Guthrie, Hongquan Zhang, Xing Fang Li, and X. Chris Le. Selection and analytical applications of aptamers. *TrAC - Trends in Analytical Chemistry*, 25:681–691, 2006.

[48] Laura Pasquardini, Simone Berneschi, Andrea Barucci, Franco Cosi, Ramona Dallapiccola, Massimiliano Insinna, Lorenzo Lunelli, Gualtiero Nunzi Conti, Cecilia Pederzolli, Simone Salvadori, and Silvia Soria. Whispering gallery mode aptasensors for detection of blood proteins. *Journal of biophotonics*, 6(2):178–87, February 2013.

[49] Marina Cretich, Giovanna Pirri, Francesco Damin, Isabella Solinas, and Marcella Chiari. A new polymeric coating for protein microarrays. *Analytical biochemistry*, 332(13):67–74, September 2004.

[50] Jurjen Ter Maat, Remco Regeling, Menglong Yang, Marja N. Mullings, Stacey F. Bent, and Han Zuilhof. Photochemical covalent attachment of alkene-derived monolayers onto hydroxyl-terminated silica. *Langmuir*, 25:11592–11597, 2009.

[51] Subramanian Balamurugan, Anne Obubuafo, Steven A Soper, and David A Spivak. Surface immobilization methods for aptamer diagnostic applications. *Analytical and bioanalytical chemistry*, 390(4):1009–21, March 2008.

[52] Ji-Yeon Byeon and Ryan C Bailey. Multiplexed evaluation of capture agent binding kinetics using arrays of silicon photonic microring resonators. *The Analyst*, 136(17):3430–3, September 2011.

[53] Gary L. Long and J. D. Winefordner. Limit of Detection A Closer Look at the IUPAC Definition. *Analytical Chemistry*, 55(7):712A–724A, June 1983.

[54] Ian M. White and Xudong Fan. On the performance quantification of resonant refractive index sensors. *Optics Express*, 16(2):1020, January 2008.

[55] Samantha M Grist, Shon a Schmidt, Jonas Flueckiger, Valentina Donzella, Wei Shi, Sahba Talebi Fard, James T Kirk, Daniel M Ratner, Karen C Cheung, and Lukas Chrostowski. Silicon photonic micro-disk resonators for label-free biosensing. *Optics express*, 21:7994–8006, 2013.

[56] Yang Shen, Jianhua Zhou, Tianran Liu, Yuting Tao, Ruibin Jiang, Mingxuan Liu, Guohui Xiao, Jinhao Zhu, Zhang-Kai Zhou, Xuehua Wang, Chongjun Jin, and Jianfang Wang. Plasmonic gold mushroom arrays with refractive index sensing figures of merit approaching the theoretical limit. *Nature communications*, 4:2381, January 2013.

[57] Lijun Huang, Huiping Tian, Daquan Yang, Jian Zhou, Qi Liu, Pan Zhang, and Yuefeng Ji. Optimization of figure of merit in label-free biochemical sensors by designing a ring defect coupled resonator. *Optics Communications*, July 2014.

[58] Yuze Sun and Xudong Fan. Optical ring resonators for biochemical and chemical sensing. *Analytical and bioanalytical chemistry*, 399(1):205–11, January 2011.

[59] Kerry J Vahala. Optical microcavities. *Nature*, 424(6950):839–46, August 2003.

[60] John E. Heebner, Vincent Wong, Aaron Schweinsberg, Robert W. Boyd, and Deborah J. Jackson. Optical transmission characteristics of fiber ring resonators. *IEEE Journal of Quantum Electronics*, 40:726–730, 2004.

[61] Vanessa Zamora, Antonio Díez, Miguel V. Andrés, and Benito Gimeno. Refractometric sensor based on whispering-gallery modes of thin capillarie. *Optics Express*, 15(19):12011, September 2007.

[62] C. Ciminelli, F. Dell'Olio, D. Conteduca, C.M. Campanella, and M.N. Armenise. High performance SOI microring resonator for biochemical sensing. *Optics & Laser Technology*, 59:60–67, 2014.

[63] K. De Vos, J. Girones, T. Claes, Y. De Koninck, S. Popelka, E. Schacht, R. Baets, and P. Bienstman. Multiplexed Antibody Detection With an Array of Silicon-on-Insulator Microring Resonators. *IEEE Photonics Journal*, 1(4):225–235, October 2009.

[64] Florian Sedlmeir, Richard Zeltner, Gerd Leuchs, and Harald G.L. Schwefel. High-Q MgF_2 whispering gallery mode resonators for refractometric sensing in aqueous environment. *Optics Express*, 22:30934, 2014.

[65] D K Armani, T J Kippenberg, S M Spillane, and K J Vahala. Ultra-high-Q toroid microcavity on a chip. *Nature*, 421(6926):925–8, February 2003.

[66] T. Kippenberg, J. Kalkman, A. Polman, and K. Vahala. Demonstration of an erbium-doped microdisk laser on a silicon chip. *Physical Review A*, 74(5):051802, November 2006.

[67] Hansuek Lee, Tong Chen, Jiang Li, Ki Youl Yang, Seokmin Jeon, Oskar Painter, and Kerry J. Vahala. Chemically etched

ultrahigh-Q wedge-resonator on a silicon chip. *Nature Photonics*, 6(6):369–373, May 2012.

[68] A. Yariv. Universal relations for coupling of optical power between microresonators and dielectric waveguides. *Electronics Letters*, 36(4):321, February 2000.

[69] Michael L. Gorodetsky and Aleksey E. Fomin. Geometrical theory of whispering-gallery modes. *IEEE Journal on Selected Topics in Quantum Electronics*, 12:33–39, 2006.

[70] Mark Oxborrow. Traceable 2-D finite-element simulation of the whispering-gallery modes of axisymmetric electromagnetic resonators. In *IEEE Transactions on Microwave Theory and Techniques*, volume 55, pages 1209–1218, 2007.

[71] Matthew Borselli, Thomas Johnson, and Oskar Painter. Beyond the Rayleigh scattering limit in high-Q silicon microdisks: theory and experiment. *Optics express*, 13:1515–1530, 2005.

[72] Romain Guider, Nicola Daldosso, Alessandro Pitanti, Emmanuel Jordana, Jean-Marc Fedeli, and Lorenzo Pavesi. NanoSi low loss horizontal slot waveguides coupled to high Q ring resonators. *Optics express*, 17:20762–20770, 2009.

[73] Comsol. Wave Optics Module User's Guide. Technical report, Comsol AB, 2013.

[74] Ladislav Prkna, Jiří Čtyroký, and Milan Hubálek. Ring microresonator as a photonic structure with complex eigenfrequency. *Optical and Quantum Electronics*, 36(1-3):259–269, January 2004.

[75] M Imran Cheema and Andrew G Kirk. Accurate determination of the quality factor and tunneling distance of axisymmetric resonators for biosensing applications. *Optics express*, 21(7):8724–35, April 2013.

[76] Davide Gandolfi, Fernando Ramiro-Manzano, Francisco Javier Rebollo Aparico, Mher Ghulinyan, Georg Pucker, and Lorenzo Pavesi. Role of Edge Inclination in an Optical Microdisk Resonator for Label-Free Sensing. *Sensors*, 15(3):4796–4809, 2015.

[77] Steven Johnson, M. Ibanescu, M. Skorobogatiy, O. Weisberg, J. Joannopoulos, and Y. Fink. Perturbation theory for Maxwell's equations with shifting material boundaries. *Physical Review E*, 65(6):066611, June 2002.

[78] Iwao Teraoka, Stephen Arnold, and Frank Vollmer. Perturbation approach to resonance shifts of whispering-gallery modes in a dielectric microsphere as a probe of a surrounding medium. *Journal of the Optical Society of America B*, 20(9):1937, 2003.

[79] Ping Lu, Liqiu Men, Kevin Sooley, and Qiying Chen. Tapered fiber Mach-Zehnder interferometer for simultaneous measurement of refractive index and temperature. *Applied Physics Letters*, 94, 2009.

[80] A. Marconi, A. Anopchenko, M. Wang, G. Pucker, P. Bellutti, and L. Pavesi. High power efficiency in Si-nc/SiO2 multilayer light emitting devices by bipolar direct tunneling. *Applied Physics Letters*, 94, 2009.

[81] A. Tengattini, D. Gandolfi, N. Prtljaga, A. Anopchenko, J. M. Ramirez, F. Ferrarese Lupi, Y. Berencen, D. Navarro-Urrios, P. Rivallin, K. Surana, B. Garrido, J.-M. Fedeli, and L. Pavesi. Toward a 1.54 μm Electrically Driven Erbium-Doped Silicon Slot Waveguide and Optical Amplifier. *Journal of Lightwave Technology*, 31(3):391–397, February 2013.

[82] Winnie Ning Ye. *Stress engineering for polarization control in Silicon-On-Insulator waveguides and its applications in novel passive polarization splitters/filters*. PhD thesis, Carleton University, Ottawa, Canada, 2006.

[83] Marta Guarisco. *Development of a new functionlaization process for label-free biosensors*. Master thesis, University of Trento, 2014.

[84] W M Yunus and A B Rahman. Refractive index of solutions at high concentrations. *Applied optics*, 27:3341–3343, 1988.

[85] L. Ferraioli, M. Wang, G. Pucker, D. Navarro-Urrios, N. Daldosso, C. Kompocholis, and L. Pavesi. Photoluminescence of silicon nanocrystals in silicon oxide. *Journal of Nanomaterials*, 2007, 2007.

[86] A. Anopchenko, A. Marconi, E. Moser, S. Prezioso, M. Wang, L. Pavesi, G. Pucker, and P. Bellutti. Low-voltage onset of electroluminescence in nanocrystalline- Si/ SiO 2 multilayers. *Journal of Applied Physics*, 106, 2009.

[87] L Pavesi. Will silicon be the photonic material of the third millenium?. *Journal of Physics: Condensed Matter*, 15:R1169–R1196, 2003.

[88] K Liu and M G Littman. Novel geometry for single-mode scanning of tunable lasers. *Optics letters*, 6:117–118, 1981.

[89] Akshay Bhat. Application note 5129: Stabilize Your Transimpedance Amplifier. Technical report, Maxim Integrated, 2011.

[90] Todd Squires and Stephen Quake. Microfluidics: Fluid physics at the nanoliter scale. *Reviews of Modern Physics*, 77(3):977–1026, October 2005.

[91] Romain Guider, Davide Gandolfi, Lorenzo Pavesi, Georg Pucker, Alina Samusenko, Floris Falke, and Erik Schreuder. Symphony - D2.1 - "Design of photonic sensor". Technical report, FP7 EU project Symphony, 2014.

[92] Qian Wang, Gerald Farrell, and Thomas Freir. Effective index method for planar lightwave circuits containing directional couplers. *Optics Communications*, 259(1):133–136, March 2006.

[93] M. Heiblum and J. Harris. Analysis of curved optical waveguides by conformal transformation. *IEEE Journal of Quantum Electronics*, 11(2):75–83, February 1975.

[94] P. Bienstman, E. Six, A. Roelens, M. Vanwolleghem, and R. Baets. Calculation of bending losses in dielectric waveguides using eigenmode expansion and perfectly matched layers. *IEEE Photonics Technology Letters*, 14(2):164–166, February 2002.

[95] Kerstin Wörhoff, Edwin Klein, Gamar Hussein, and Alfred Driessen. Silicon oxynitride based photonics. *Proceedings of 2008 10th Anniversary International Conference on Transparent Optical Networks, ICTON*, 3:266–269, 2008.

[96] Vilson R. Almeida, Roberto R. Panepucci, and Michal Lipson. Nanotaper for compact mode conversion. *Optics Letters*, 28(15):1302, August 2003.

[97] Minhao Pu, Liu Liu, Haiyan Ou, Kresten Yvind, and Jørn M. Hvam. Ultra-low-loss inverted taper coupler for silicon-on-insulator ridge waveguide. *Optics Communications*, 283(19):3678–3682, October 2010.

[98] Linhong Kou, Daniel Labrie, and Petr Chylek. Refractive indices of water and ice in the 0.65- to 2.5-μm spectral range. *Appl. Opt.*, 32(19):3531–3540, 1993.

[99] Muzammil Iqbal, Martin A Gleeson, Bradley Spaugh, Frank Tybor, William G Gunn, Michael Hochberg, Tom Baehr-Jones, Ryan C Bailey, and L Cary Gunn. Label-Free Biosensor Arrays Based on Silicon Ring Resonators and High-Speed Optical Scanning Instrumentation. *IEEE Journal of Selected Topics in Quantum Electronics*, 16(3):654–661, 2010.

[100] Sahba Talebi Fard, Valentina Donzella, Shon A Schmidt, Jonas Flueckiger, Samantha M Grist, Pouria Talebifard, Yichen Wu, Rick J Bojko, Ezra Kwok, Nicolas A F Jaeger, Daniel M Ratner, and Lukas Chrostowski. Performance of ultra-thin SOI-based resonators for sensing applications. *Optics Express*, 22(12):9499–9506, 2014.

[101] Shinyoung Lee, Seok Chan Eom, Jee Soo Chang, Chul Huh, Gun Yong Sung, and Jung H Shin. A silicon nitride microdisk resonator with a 40-nm-thin horizontal air slot. *Optics express*, 18(11):11209–15, May 2010.

[102] Niranjan M. Hanumegowda, Caleb J. Stica, Bijal C. Patel, Ian White, and Xudong Fan. Refractometric sensors based on microsphere resonators. *Applied Physics Letters*, 87:1–3, 2005.

[103] Tao Ling and L. Jay Guo. Sensitivity enhancement in optical micro-tube resonator sensors via mode coupling. *Applied Physics Letters*, 103, 2013.

[104] Kerstin Wörhoff, Edwin Klein, Gamar Hussein, and Alfred Driessen. Silicon oxynitride based photonics. *Proceedings of*

2008 10th Anniversary International Conference on Transparent Optical Networks, ICTON, 3:266–269, 2008.

[105] Ehsan Shah Hosseini, Siva Yegnanarayanan, Amir H. Atabaki, Mohammad Soltani, and Ali Adibi. High quality planar silicon nitride microdisk resonators for integrated photonics in the visible wavelength range. *Optics Express*, 17(17):14543, August 2009.

[106] Katrien De Vos, Irene Bartolozzi, Etienne Schacht, Peter Bienstman, and Roel Baets. Silicon-on-Insulator microring resonator for sensitive and label-free biosensing. *Optics express*, 15(12):7610–5, June 2007.

[107] P. V. Lambeck. Remote opto-chemical sensing with extreme sensitivity: Design, fabrication and performance of a pigtailed integrated optical phase-modulated Mach-Zehnder interferometer system. *Sensors and Actuators, B: Chemical*, 61:100–127, 1999.

[108] B Sepúlveda, A Calle, L M Lechuga, and G Armelles. Highly sensitive detection of biomolecules with the magneto-optic surface-plasmon-resonance sensor. *Optics letters*, 31(8):1085–1087, 2006.

[109] Hao Li and Xudong Fan. Characterization of sensing capability of optofluidic ring resonator biosensors. *Applied Physics Letters*, 97, 2010.

[110] Charlie O Parker, Yvonne H Lanyon, Mary Manning, Damien W M Arrigan, and Ibtisam E Tothill. Electrochemical immunochip sensor for aflatoxin M1 detection. *Analytical chemistry*, 81(13):5291–8, July 2009.

[111] Arnoud Marquart. Sprpages. `http://sprpages.nl/kinetics/association.html`.

[112] Aniela Wochner, Marcus Menger, Dagmar Orgel, Birgit Cech, Martina Rimmele, Volker a. Erdmann, and Jörn Glökler. A DNA aptamer with high affinity and specificity for therapeutic anthracyclines. *Analytical Biochemistry*, 373:34–42, 2008.

[113] Laura Pasquardini, Romain Guider, Davide Gandolfi, Lorenzo Lunelli, Cecilia Pederzolli, and Cristina Potrich. Symphony - D3.2 - "Sensor functionalization and regeneration procedure". Technical report, 2014.

[114] MS Luchansky, AL Washburn, and TA Martin. Characterization of the evanescent field profile and bound mass sensitivity of a label-free silicon photonic microring resonator biosensing platform. *Biosens Bioelectron.*, 26(4):1283–1291, 2010.

[115] M. Carmen Estevez, Marinus A. Otte, Borja Sepulveda, and Laura M. Lechuga. Trends and challenges of refractometric nanoplasmonic biosensors: A review. *Analytica Chimica Acta*, 806:55–73, 2014.

[116] Tae Jung Park, Seok Jae Lee, Do Kyun Kim, Nam Su Heo, Jung Youn Park, and Sang Yup Lee. Development of label-free optical diagnosis for sensitive detection of influenza virus with genetically engineered fusion protein. *Talanta*, 89:246–252, 2012.